

A Bio-Inspired Computational Model of Cardiac Mechanics: Pathology and Development.

Thesis by
Anna Grosberg

In Partial Fulfillment of the Requirements
for the Degree of
Doctor of Philosophy



California Institute of Technology
Pasadena, California

2008
(Defended April 11, 2008)

Acknowledgements

I would like to thank my adviser Mory Gharib for his guidance and support throughout my time at Caltech. He has taught me by word and example in both the joy of new results and the disappointments of the difficulties. His admirable breadth of scientific horizons and depth of his insights, his soft style and infinite patience were among the most important factors of my growth as a researcher.

I would like to thank my committee members Kaushik Bhattacharya, Scott Fraser, and Rob Phillips for their time and attention and for their valuable advice; and Guruswami (Ravi) Ravichandran for introducing me to ABAQUS.

I would like to thank my friends and Gharib group-mates for their support and help throughout my years in graduate school. My time at Caltech would have been bleak without the atmosphere of friendliness in the group.

I would like to thank Dr. Paul Finn of UCLA Medical School and Dr. David Sahn of OSHU for their suggestions and interest in my work, and for the medical insights they opened up for me.

I would like to thank my high school chemistry teacher Ms. Rene Gibb of Brookline High School, MA, who played an integral role in setting me on the path that brought me to this thesis.

I would like to thank my family for the unconditional support that spans time zones and continents.

Abstract

In this work we study the function and development of the myocardium by creating models that have been stripped down to essentials. The model for the adult myocardium is based on the double helical band formation of the heart muscle fibers, observed in both histological studies and advanced DTMRI images. The muscle fibers in the embryonic myocardium are modeled as a helical band wound around a tubular chamber. We model the myocardium as an elastic body, utilizing the finite element method for the computations. We show that when the spiral band architecture is combined with spatial wave excitations the structure is twisted, thus driving the development of the embryonic heart into an adult heart. The double helical band model of the adult heart allows us to gain insight into the long standing paradox between the modest, by only 15%, ability of muscle fibers to contract, and the large left ventricular volume ejection fraction of 60%. We show that the double helical band structure is the essential factor behind such efficiency. Additionally, when the double helical band model is excited following the path of the Purkinje nerve network, physiological twist behavior is reproduced. As an additional validation, we show that when the stripped down double helical band is placed inside a sack of soft collagen-like tissue it is capable of producing physiologically high pressures.

We further develop the model to understand the different factors behind the loss of efficiency in heart with a common pathology such as dilated cardiomyopathy. Using the stripped down model we are able to show that the change to fiber angle is the much more important factor to heart function than the change in gross geometry. This finding has the potential to greatly impact the strategy used in certain surgical procedures.

Contents

Acknowledgements	iii
Abstract	iv
List of Figures	x
List of Tables	xiii
1 Introduction	1
1.1 Background	1
1.1.1 Physiology of the human heart	1
1.1.1.1 Heart development	2
1.1.1.2 Adult heart anatomy	3
1.1.1.3 Myocardium architecture	3
1.1.1.4 Functional properties of the left ventricle	4
1.1.1.5 Pathologies	5
1.1.2 Modeling the Heart	6
1.2 Overview of the Present Work	8
1.2.1 Modeling of helical muscle bands	8
1.2.2 Spiral elastic bands and development	9
1.2.3 Adult Heart Model: Ejection Fraction and Twist	9
1.2.4 Modeling pathologies in the heart	10
2 Computational models of heart pumping efficiencies based on contraction waves in spiral elastic bands	11
2.1 Introduction	11
2.2 Methods	13
2.2.1 Geometries of muscle bands	13
2.2.1.1 A simple tube	14
2.2.1.2 A two chamber structure	15

2.2.2	Choosing the Geometrical Parameters	18
2.2.2.1	Embryonic tube heart	18
2.2.2.2	Adult heart	19
2.2.3	Material properties	20
2.2.4	Boundary conditions	20
2.2.4.1	Embryonic tube heart	21
2.2.4.2	Adult heart	21
2.2.5	Different Excitation schemes	21
2.2.6	Computational methods	24
2.2.7	Data Analysis	24
2.3	Results	26
2.3.1	Step excitation	26
2.3.2	Temporal excitation	27
2.3.3	Spatial wave excitation	29
2.3.3.1	Simple spatial waves: Adult Heart	30
2.3.3.2	Timing of maximal contraction: Adult Heart	30
2.3.3.3	Initial increase in volume: Adult Heart	31
2.3.3.4	Simple spatial waves: Tube	31
2.3.3.5	Pumping with suction: Tube	31
2.4	Conclusions	32
3	Physiology in phylogeny: Modeling of mechanical driving forces in cardiac development	34
3.1	Introduction	34
3.1.1	Some Hints from Embryonic Heart Development	35
3.1.1.1	The development of the heart	35
3.1.1.2	A basic observation	36
3.1.2	Modeling	37
3.2	Methods	38
3.2.1	Geometry of the ribbon models	38
3.2.1.1	Embryonic tube heart	38
3.2.1.2	Adult heart	38
3.2.2	Choosing the Geometrical Parameters	39
3.2.2.1	Embryonic tube heart	39
3.2.2.2	Adult heart	40
3.2.3	Material properties	41

3.2.4	Boundary conditions	41
3.2.4.1	Embryonic tube heart	41
3.2.4.2	Adult heart	41
3.2.5	Excitation schemes	42
3.2.6	Computational methods	42
3.2.7	Data Analysis	43
3.3	Results	44
3.3.1	No twist in a uniformly contracted spiral band	44
3.3.2	Back to the future: Adult heart model	44
3.3.2.1	Simulations of the Adult heart	46
3.3.2.2	How uniform vs. spatial-wave contractions affect pumping ability: Adult heart model	46
3.3.2.3	Different dynamics caused by spatial-waves	46
3.3.3	Forward to the Past: Embryonic heart model	48
3.3.3.1	How uniform vs. spatial-wave contractions affect pumping ability: Embryonic heart model	48
3.3.4	Evidence of twisting in a spiral undergoing a spatial-wave contraction	49
3.4	Conclusions	50
4	Modeling the macrostructure of the heart as a dynamic double helical band	52
4.1	Introduction	52
4.2	Methods	54
4.3	Results and Discussion	59
4.3.1	Large volume changes – small local deformations	59
4.3.2	Twist in the left ventricle	59
4.3.3	Timing relationship between twist and ejection fraction	61
4.3.4	Varying the point of the initiation of spatial excitation waves	62
4.4	Conclusion	63
5	Modeling the macrostructure of the heart: healthy and diseased	64
5.1	Introduction	64
5.2	Methods	67
5.2.1	Geometries of the bands	67
5.2.2	Material Properties	70
5.2.3	Boundary Conditions and Excitation	71
5.2.4	Computational Methods	71
5.2.5	Data Analysis	72

5.2.5.1	Volume and Ejection fraction	72
5.2.5.2	Rate of Filling	72
5.2.5.3	Twist and Torsion	73
5.3	Results	73
5.3.1	Ejection fraction	73
5.3.2	Rate of Filling in the initial diastole period	74
5.3.3	Torsion of the left ventricle	75
5.4	Discussion and Conclusion	75
5.4.1	The importance of the normal double looped response	75
5.4.2	Comparing different model results	77
5.4.3	Conclusion	78
6	The filled-out heart model: pressure in the left ventricle	80
6.1	Introduction	80
6.2	Methods	81
6.2.1	Geometries of the chambers	81
6.2.2	Active Material Properties	83
6.2.3	Non-active material properties	84
6.2.4	Excitation	85
6.2.5	Computational Methods	86
6.2.6	Modeling the Blood	86
6.2.7	Valves	86
6.2.8	Data Analysis	87
6.3	Results	87
6.4	Conclusion	89
7	Outlook and possible future directions	91
A	Additional Analytical Calculations	94
A.1	Inherent limit on pumping efficiency of structures with non-helical fibers	94
B	Analytical estimate of energy efficiency of twist vs. contraction pumps	95
B.1	Introduction	95
B.2	Pumping from a Cylindrical shell	95
B.2.1	Radial shortening of the tube	95
B.2.2	Twisting of the tube	98
B.2.3	Pumping against inner pressure	103
B.2.4	Comparing the two different methods of pumping	103

B.3	Pumping from a half ellipsoid shell	104
B.3.1	Radial Contraction in a Shell	105
B.3.2	Twisting of a Shell	106
B.4	Conclusion	108
C	Additional Methods	109
C.1	Geometrical parameters in formulating the Double helical heart: healthy and diseased	109
C.2	Calculating Twist of the Left ventricle	110
C.3	Calculating radius of curvature	112
C.4	Radius of Curvature for a helix about a cylinder	113
D	Extra Figures	114
D.1	Additional figures for chapter 2	114
D.2	Additional figures for chapter 4	115
D.3	Alternate figures for chapter 5	116
	Bibliography	119

List of Figures

1.1	Embryonic heart images of zebra fish and model.	2
1.2	The photograph of the Torrent-Guasp heart model.	4
2.1	Images of the spiral muscle band models for the embryonic heart.	15
2.2	Initial band shape and fitted volume shown from different points of view.	16
2.3	Parametric plots for five excitation waves: step, temporal, spatial wave types.	23
2.4	The left ventricular ejection fraction vs. time for adult heart model subject to different excitation patterns.	27
2.5	Snapshots of the movies for the adult heart model.	28
2.6	Snapshots of the movies for the embryonic heart model.	29
2.7	The dependence of the ejection fraction on the pitch angle for four different contraction schemes for a tube spiral geometry.	30
2.8	The volume evolution with time for four different excitation schemes applied to a spiral with a pitch angle of 60°	32
3.1	Images of the muscle fibers in the heart contrasted with the band model.	35
3.2	A possible set of steps in the development from a spiral tube to a double helix band.	36
3.3	Images of the spiral muscle band models for the embryonic heart.	38
3.4	Images of the double helical band model of the adult heart.	39
3.5	Snapshots of the ABAQUS simulations at different time steps for the embryonic heart spiral model with a 50° pitch (fiber) angle.	45
3.6	Snapshots of the ABAQUS simulations at different time steps for the adult heart double helix model.	47
3.7	Plots of normalized volume of the tube chamber vs. time and ejection fraction vs. time	49
4.1	DTMRI images contrasted with Torrent-Guasp model of fiber architecture.	54
4.2	Initial shape of the double helical model.	55
4.3	The double helical band with the twist markers.	56
4.4	The contour plots show the degree of activation for each of the dynamic excitation schemes tried.	58

4.5	Snapshots of the movies for the adult heart model.	60
4.6	Ejection Fraction vs. Time for four cases	61
4.7	Plots of twist vs. normalized ejection fraction.	62
5.1	Sketches of plots of torsion vs. normalized ejection fraction.	65
5.2	The model contrasted with DTMRI images of fiber band architecture.	66
5.3	Image of the left ventricular surfaces with the band.	67
5.4	Double helical band with various fiber architecture.	68
5.5	Double helical band with different degrees of dilations.	69
5.6	Double helical band with other types of damage.	70
5.7	Top view of the double helical band model color coded for excitation.	71
5.8	Volume of the left ventricle vs. time for each model.	74
5.9	Plots of torsion vs. normalized ejection fraction.	76
5.10	Rough schematic drawing of different torsion ejection fraction relationships.	77
6.1	Images of the elements of the filled-out model.	83
6.2	The effect of bulging out through the soft material.	88
6.3	Plots of pressure vs. time.	89
B.1	A schematic of radially squeezed tube, with a few wires drawn.	96
B.2	Two different ways to create radial shortening through bending of the wires.	97
B.3	The plot of work required vs. the ejection fraction achieved for radial contraction in a tube, $n=5$	98
B.4	Twisting of helically arranged fibers.	99
B.5	The cylinder laid out flat, showing the twist angle and the distance between the wires.	100
B.6	The maximum ejection fraction possible with the twist method as a function of γ	101
B.7	The plot of work required vs. the ejection fraction achieved for twisting of the bottom of the tube.	102
B.8	The plot of work required vs. the ejection fraction achieved for both the twisting of the bottom of the tube and radial shortening of wires.	103
B.9	The plot of work required vs. the maximal ejection fraction achieved for both the radial shortening of wires and the most efficient twisting of the bottom of the tube.	104
B.10	The plot of work required vs. the ejection fraction achieved for both the twisting of the bottom of the tube and radial shortening of wires.	104
C.1	A sketch of the two dimensional projection of the “sandwich” with markers.	111
D.1	The form of the band before Factor 1 and Factor 2 were included into equation 2.5.	114

D.2	Twist vs. normalized ejection fraction for spatial waves with varying origin of excitation.	115
D.3	Top view: The model double helical band is color coded for the fiber angle.	116
D.4	Different view: The model double helical band.	117
D.5	Side view of the double helical band model color coded for excitation.	117
D.6	The double helical band after “infarction” with the twist markers.	118
D.7	Twist vs. normalized ejection fraction	118

List of Tables

2.1	The ejection fraction values for double helical pumps under different excitation patterns	26
3.1	The ejection fraction values for double helical pumps under different excitation patterns	46
3.2	The ejection fraction values for tubular pumps with different pitch (fiber) angles, under different excitation patterns	50
5.1	Results for different model types	73

Chapter 1

Introduction

Heart disease is the leading cause of death in America [1] and in the rest of the developed world. The American Heart Association (AHA) has promoted cardiovascular research for more than half-a-century, yet more than a million people suffer from heart attacks each year. Amazing progress has been achieved in medicine, allowing for both open chest surgeries (such as coronary artery bypass surgery) and less invasive procedures to be used in preventing fatalities caused by heart disease. There are many stages of heart disease, and in most of them the patients exhibit clear symptoms, such as shortness of breath and fatigue. However, by the time such symptoms appear unrecoverable damage has likely been done to the heart. According to AHA guidelines, patients in stage B of heart disease are not yet exhibiting symptoms, but have structural remodeling of the myocardium [2, 3]. This makes diagnosis of patients in this stage a challenge, yet crucial to our ability to correct the damage with non-invasive means. Through dedicated work, doctors and scientists have found risk factors, such as high blood pressure and high cholesterol. Still, no current technology has the capability of diagnosing the initial stages of heart failure, because of our limited understanding of the mechanics of heart failure. So what do we know?

1.1 Background

1.1.1 Physiology of the human heart

The human heart beats about once every second, or more than two and a half billion times during an average lifetime. The heart is very adaptive, providing sufficient amounts of blood to our body while we rest or strenuously exercise. This biological pump has evolved to be amazingly efficient, to adjust and to correct itself in a wide range of situations. The heart exhibits this flexibility and agility in response to mechanical stimuli from the first stages of development.

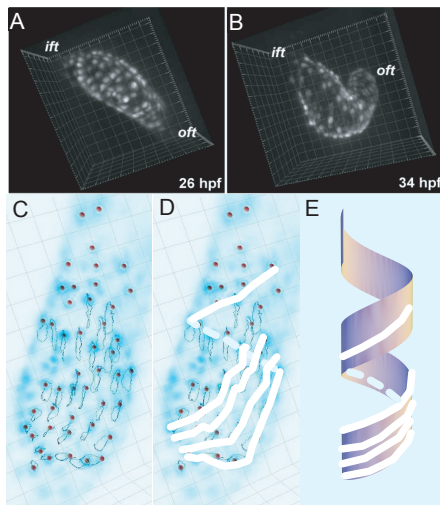


Figure 1.1: Three-dimensional reconstruction of a transgenic embryonic zebrafish heart at (A) 26 hours past fertilization and (B) 34 hours past fertilization. The inlet and outlet have been labeled. At both ages, analyzed region is mostly located in the ventral side towards the left lateral direction. (C) The trajectories of the fluorescent myocardial cells are tracked and marked at 26 hours post. The reconstruction was obtained by acquiring 40 optical sections (3 μ m intervals) at high speed (151 fps) with a confocal microscope (Zeiss LSM 5 LIVE). These sections were synchronized using a wavelet-based registration algorithm. (D) Shows possible direction of the fibers consistent with the trajectories of the myocytes. (E) A helical band is shown for comparison. (A)&(B) Produced by Michael Liebling and Arian S. Forouhar; (C) Produced by Abbas Moghaddam.

1.1.1.1 Heart development

At initial formation, the embryonic heart is a tube with two sulcus [4]. It starts beating on the twenty second day after conception. The initial form of the heart – a tubular pump – is often studied using fish embryonic hearts as model systems [5, 6]. It has been found that the muscle cells in the wall of the embryonic heart tube are arranged in a helical fiber framework [7, 8] (see figure 1.1).

Fibers wound around a cylinder have been studied as far back as the 1950s in worm locomotion [9, 10]. It was discovered that, for a given length of fiber and cylinder radius, the greatest volume change at a given fiber length change could be achieved at a helix angle of 55° . In these studies of worms, it was assumed the fibers were rigid and the muscles would be acting either radially or longitudinally. However, even the authors point out that diagonal muscles cannot be modeled by such a system. In the embryonic tubular heart, the diagonal fibers are active and their arrangement could impact both the efficiency of the early pumping and the further development.

Indeed, soon after the embryonic heart starts to beat, it begins its road to an adult heart by starting to loop. The driving mechanism for this change has not been fully understood. The heart tube goes through a sequence of bending and twisting transformations, first going into a “c” loop, then an “s” loop that is “matured,” after which the main architecture of the four chamber heart is

discernible [11]. This looping have been experimentally modeled using elastic tubing and compared to direct images from chick embryos [12]. However, the simulations performed by Manner et al. start at the “c” loop stage and explore the mode of rotation of the looping heart, not the driving forces necessary for such a deformation. By the eighth week, with the looping complete, some of the chamber walls are remodeled and the heart takes on the form of the four chamber pump.

1.1.1.2 Adult heart anatomy

The heart has four chambers: right and left ventricles, plus right and left atria. The atria chambers receive blood and pump it into the ventricles. The left atrium and ventricle are separated by the Mitral valve, which is sometimes also called the A-V valve. The right atrium and ventricle are separated by the tricuspid valve. The right ventricle (RV) and the left ventricle (LV) are the main pumping mechanisms of the heart. The right ventricle pumps the blood into the pulmonary system through the pulmonary valve. The left ventricle supplies the systemic circulation through the aortic valve, which leads into the the aorta (the main aortic vessel) [13]. A heart goes through a cardiac cycle during each heart beat. The cardiac cycle is divided into two distinct periods: systole and diastole. During systole, the heart contracts pumping blood out of the ventricles. While during diastole, the heart relaxes and the ventricles are filled with blood from the atria.

The two ventricles are separated by the septum. The plane where the ventricles meet the atria is called the basal plane. The other end of the heart, the lowest point, is called the apex. The outside surface of the heart is, for ease of terminology, divided into four surfaces. The anterior, or sternocostal, surface mainly bounds the right ventricle. The right pulmonary surface is formed by the right atrium. The left pulmonary surface bounds the left ventricle from the side of the left lung. The diaphragmatic, or inferior, surface bounds the left ventricle from the diaphragm side.

The heart is surrounded by a fibrous sack called the pericardium. The pericardium prevents the heart from over dilating (expanding too much). The pericardial cavity is the small space between the heart and the pericardium wall. On the outside of the heart there is a thin layer of tissue called the epicardium. The inside of the chambers is lined with a similar tissue called the endocardium. The myocardium is the main musculature of the heart and is between these two linings [14].

1.1.1.3 Myocardium architecture

The myocardium is a matrix, consisting of collagen, muscle and some other proteins. There are three types of cardiac muscle: atrial and ventricular types, plus the excitatory and conductive muscle fibers. The atrial and ventricular types behave very similarly to skeletal muscle, although the duration of contraction is much longer. The excitatory and conductive muscle fibers, which exhibit rhythmicity and varying rates of contraction, provide a fine tuned control of the rhythmical beating of the heart. The excitation of the heart muscles is controlled through the specialized



Figure 1.2: The photograph of the Torrent-Guasp heart model.

conductive system of the heart called the Purkinje system [15]. The excitation starts at the sinus node in the right atrium, moves to the A-V node located in the septum, where it is delayed and then passed into the ventricles going from the apex of the heart towards the outside and up through the heart walls. The different types of muscle and collagen cells are organized into muscle fibers called myofibrils. These fibers can contract by about 15% [16]. This biological constraint is very important when considering the efficiency of the heart, and we will come back to it many times.

The three dimensional layout of the fibers in the myocardium is not random. The heart has been described as a helical arrangement of fibers as far back as 1600s by Lower [17]. In 1891, Krehl described the multiple spirals formed by the muscle bands [18]. In 1933, some of these spirals were connected by Rob and Rob, creating a helical framework for the myocardium [19]. In 1969, using then cutting edge imaging technology, Streeter mapped the fiber orientation in the free wall of the left ventricle. He found that the fiber angle linearly varies from the endocardium to the epicardium [20]. It was proposed from these findings that the myocardium consists of sheets of helical fibers with changing orientation from the epicardium to the endocardium [16]. Another histological study done in the early seventies by Torrent-Guasp was aimed at isolating the muscle fibers from the collagen network. He showed that the muscle fibers are combined into a single band, which is wound about the two ventricles in a double helical arrangement [21]. The photographs of a cast of a heart that has been unwrapped are shown in figure 1.2. Most recently, the fibers in the heart were mapped using magnetic resonance imaging [22]. Figures 4 through 6 of the paper by Zhukov and Barr [22] show the fibrous network to be more complex than a simple combination of sheets. Another MRI study, in which Helm et al. were able to isolate the muscle fibers in the images, using DTMRI [23], showed an arrangement more closely resembling a helical band than sheets of fibers [24]. It has been realized that the way these fibers are arranged has a great impact on heart function [25, 26].

1.1.1.4 Functional properties of the left ventricle

The volume of the relaxed left ventricle is about 130 mL. During each of its two and a half billion beats, the left ventricle of the heart pumps out about 70 mL of blood, or in other words about 60% of its volume (this volume exchange ratio is commonly referred to as the ejection fraction). This

number gains new meaning when we recall that the muscle fibers providing for this volume ejection can only contract by 15%. One interesting fact is immediately evident from this information: if the muscle fibers were arranged circumferentially around the LV, the highest possible ejection fraction would be about 30% (see appendix A.1 for the calculation).

The pressures in the cardiovascular system are measured relative to the atmosphere, therefore all the pressures quoted in this manuscript will be the gauge pressures. The pressure in the left ventricle ranges from 0 Pa to 1.7×10^4 Pa (≈ 130 mmHg). Between 0 Pa and 1.3×10^4 Pa (≈ 100 mmHg), the contraction is isochoric, or in medical terminology isovolumetric. When the pressure in the ventricle reaches 1.3×10^4 Pa (≈ 100 mmHg), the aortic valve opens and the ejection of the blood begins. The ejection of the blood continues until the pressure in the ventricle falls back below 1.2×10^4 Pa (≈ 90 mmHg). The pressure continues to fall isovolumetrically until about 1.3×10^3 Pa (≈ 100 mmHg), when the mitral valve opens and filling begins. By the end of the cycle the pressure in the ventricle is back to zero.

As the heart performs its pumping function, it moves within the pericardium sack. The base of the heart is constrained by the vessels from rotating in the basal plane, while the apex of the heart is prevented from moving up or down. The remaining movement can be characterized by the twisting of the left ventricle. As is evident from the advanced imaging done of the heart, the dynamics of the left ventricle are not as simple as squeeze and release, which brings us to another interesting parameter that characterizes the dynamic behavior of the left ventricle pump: the twist. The twist is the rate of change of the angle of rotation in the left ventricle from the apex to the base. The heart gradually twists during systole as the left ventricular volume decreases, then, while the volume remains almost constant, there is rapid “un-twisting.” The volume then increases with almost no change in twist. This hysteresis loop behavior has been documented by many studies, and it has been shown to be altered in damaged hearts [27–32]. The variations of twist during the cardiac cycle have also been shown to change with age [33]. This is an important observation because solid mechanics suggests the twisting of the left ventricle to be most likely responsible for the efficient operation of the heart [34, 35]. To intuitively convince yourself of this, consider the energy efficiency of two purely analytical pump models: one that operates by twisting, and the other that operates by squeezing. It is relatively easy to show that twisting can be more efficient at any given ejection fraction (see appendix B for calculations). Therefore, through out this work we will use the twisting behavior as a gauge of the appropriateness of our models.

1.1.1.5 Pathologies

With the heart’s intricate design and its non-stop operation, it is no wonder that more people suffer from heart problems as life expectancy increases. Early diagnosis of heart disease is widely recognized as one of the important steps in battling the high mortality rates of patients suffering from heart

failure. The earlier the patient is diagnosed, the better the chances of halting the progress of heart failure.

Many types of MRI protocols can give high quality images of the heart, and are mostly used to diagnose the morphological and static aspects of the heart, but not the underlying causes of the symptoms that different diseases exhibit. Indeed, physicians primarily rely on correlation and statistical analysis, rather than an understanding of the mechanisms behind the disfunction.

For example, it is well known that Hypertrophic Cardiomyopathy produces a thickening of the heart muscle, usually at the septum below the aortic valve and in the left ventricle. However, it has not been clearly demonstrated how these changes lead to reduced heart function (especially during exercise) [36].

Another area that would benefit from a deeper understanding of cardiovascular mechanics is the surgical restorative procedures. For example, dilated cardiomyopathy is sometimes treated with cardiac surgical anterior ventricular endocardial restoration procedure. However, while there are studies showing that it is reliable, it would benefit greatly from a better understanding of the mechanical properties of the arrangement of the muscle fibers [37]. Another example is a surgical procedure called cardiomyoplasty, in which surgeons place healthy muscle tissue around the heart in an effort to aid it while it recovers from damage. However this procedure does not have a good success rate [38].

Each type of heart disease is a complex combination of many factors. For example the dilated cardiomyopathy mentioned above usually develops after an infarction. In an infarction part of the heart muscle, to which the blood flow was cut off, dies. The dead muscle has different mechanical properties than healthy tissue, thus impacting the performance of the heart [39]. As the heart attempts to compensate the ventricle is remodeled. However without assistance it cannot recover back to its healthy shape.

To gain a better understanding of the causes of these diseases, many studies have been performed on healthy hearts and ones with pathologies. Not only values for left ventricular ejection fraction, pressure and twist, but a range of other data are available, including longitudinal, circumferential and radial strain measurement, material property measurements, data on rotations and pressure measurements [16, 40]. All of these data are available for comparison with models.

1.1.2 Modeling the Heart

Modeling of the heart started long before computers were around to aid in the process. As soon as Streeter came out with his findings on helical fiber arrangement, an analytical model was constructed to show the importance of such structures [41]. In this work, Sallin showed that a shell shrunk by contracting the length of fibers on its surface produces high enough ejection fraction only if the fibers are helical. By necessity, these analytical models could only handle one shell and had unrealistic

boundary conditions.

Modeling the heart in general presents a problem of scales. The active element in the heart, the muscle cells, can only contract by a small amount of 15%, yet the global structure deformations are large. With the advance of computing technology, it became possible to approach this problem. Two distinct methods have been used to strive for a solution.

The first, is the immersed boundary method developed by Peskin et al. [42, 43]. This is a general way to simulate elastic materials interacting with fluids. While this is very interesting computationally, it is not yet possible to create models with realistic conditions. Also, using this method it is not possible to account for the preexisting stresses in the fibers. In this method the authors can achieve the proper ejection fractions, however the strain they put on the material greatly exceeds the ones observed physiologically.

The second method is based on the histological studies done by Streeter et al. and utilized the finite element method to model the solid structure of the heart. These models assume that the myocardium consists of concentric shells with varying fiber directions. Meaning, that the epicardium and endocardium will have axially directed fibers, while the fibers in the middle will be directed circumferentially [16, 35, 44]. These models have been modified and developed extensively to simulate both volume and pressure inside the left ventricle.

The paper by Vendelin et al. shows how these models can be used to optimize the fiber organization with strain, stress, or ATP consumption. However, even the most optimal models provide less than 40% ejection fraction [45].

The blood flow in combination with the left ventricular wall motion is studied using fluid-structure interaction finite element method in a paper by Watanabe et al. [46]. The authors are able to reproduce the relationship between pressure and volume in the left ventricle. However, the structure maximal contraction is assumed to correspond to the ejection fraction of 60%. In other words, they assume that the walls of the left ventricle will contract by a large enough strain to accommodate the physiological ejection fraction. This phenomenological approach made sense for this study, since it was looking at the changes in blood flow with arrhythmia, but it does not answer the question of how such a high ejection fraction is possible with the contractile limit on the muscle fibers [46].

The major advances in computational modeling of the heart based on the sheet model have been done in the McCulloch group [47, 48]. They have created a comprehensive model for the three-dimensional heart that allows for large elastic deformation and keeps the strain in the fibers to below 20%. To create more reliable constitutive relations the three dimensional strains inside the myocardium were measured [49]. As a result constitutive relations for the different tissues in the heart were formulated [16, 50]. However, the maximal ejection fraction achieved with this model is less than 40% [51].

The models based on the finding by Streeter, have been getting progressively more complicated.

In the paper by Kerckhoffs et al. [52], the researchers added the circulatory system to the cardiac model by coupling a finite element model for the ventricles and a circulation model for the circulatory system. This provided better accuracy for the relationship between pressure and volume in the left ventricle for multiple beats. However, the maximal left ventricular ejection fraction in this model was still below 45%, which is borderline heart failure [52].

In the papers by Usyk et al. [53, 54], the authors considered a three dimensional cardiac models with electromechanics for normal and dilated failing hearts. The maximal ejection fraction for the healthy system is below 45% in this model. It is unsurprising that the ejection fractions are very low for the dilated heart model ($< 30\%$). However, it is interesting to note that the authors make no attempt to measure the twist of the left ventricle to verify that the model corresponds to the physiological dilated hearts in its motion.

None of these models answer the simple question of how it is possible for the heart to achieve a 60% ejection fraction without the fibers constructing over their physiological limit of 15%.

1.2 Overview of the Present Work

In modeling the heart we took a different approach. We wanted to create the simplest possible model that would still capture the main functionality of the heart. This would allow us to isolate the dominant structures in the myocardium and to gain a deeper understanding of at least some pathologies. To do so, we turned to the histological model proposed by Torrent-Guasp and focused on bands of muscles. We follow the previous modeling work by assuming that the heart tissue can be modeled as an elastic body. In other words, all the chemical and electrical processes are lumped together into an elastic relation that has approximately the same phenomenological response as the biological tissue. We used our models to study both the embryonic hearts and the adult heart. In this we approach the problem from a number of different directions.

1.2.1 Modeling of helical muscle bands

We present a framework for modeling biological pumping organs based on coupled spiral elastic band geometries and active wave-propagating excitation mechanisms. Two pumping mechanisms are considered in details by way of example: one in the shape of a simple tube, which represents a embryonic fish heart, and another, more complicated structure with the potential to model the adult human heart. Through finite element modeling, different elastic contractions are induced in the band. For each version the pumping efficiency is measured and the dynamics are evaluated. We show that by combining helical shapes of muscle bands with a contraction wave, it is possible not only to achieve efficient pumping, but also to create desired dynamics of the structure. As a result we match the function of the model pumps and their dynamics to physiological observations.

We then take a look at the problem from the developmental point of view. What causes the heart to loop in an embryo?

1.2.2 Spiral elastic bands and development

We explore the heart phylogeny – the development of the heart from embryonic to adult shape. For the shape change (from tubular to four chamber) to be initiated, a mechanical twist needs to be present in the embryonic heart tube. We show that the helical shape of the muscle fibers in the embryonic heart is a necessary but an insufficient condition for the transformation to occur. It is also necessary for the excitation pattern to be in the form of a spatio-temporal wave. We illustrate that such a combination, while producing twist, does not negatively impact the heart’s ability to work as a pump.

Our next step is to look at the twist quantitatively.

1.2.3 Adult Heart Model: Ejection Fraction and Twist

Simple models have always been highly appreciated for their ability to isolate the dominant factors of a system. Surprisingly, this concept has never before been applied to modeling of the myocardium. Here, we report a computational study of the heart’s spiral structure modeled as a closed elastic double helix band with active local excitation following the physiological activation pattern. This model is reduced to basic essentials, allowing us to focus on the dominant structure of the heart. By means of finite element computational modeling we address two features of heart mechanics and, most importantly, their timing relationship: one of them is the ejection volume efficiency and the other is the twist of the heart. The corner stone of our approach is the assumption that the double helical muscle fiber band represents the dominant active macrostructure behind the function of the myocardium. We show that this double helical model easily reproduces a physiological maximal ejection fraction of up to 60% without exceeding the limit on local muscle fiber contraction of 15%. Moreover, a physiological ejection fraction can be achieved independently of the excitation pattern. The left ventricular twist is also largely independent of the type of excitation. However, the physiological relationship between the ejection fraction and twist can only be reproduced with Purkinje type excitation schemes. Our results indicate that the proper timing coordination between twist and ejection dynamics can be reproduced only if the excitation front originates in the septum region near the apex. This shows that the timing of the excitation is directly related to the efficient pumping operation of the heart and give credence to the possibility of using twist as an important diagnostic tool.

We also show that the simple model can be used to study the cause of pathological symptoms.

1.2.4 Modeling pathologies in the heart

In a common heart pathology, dilated cardiomyopathy, the ventricular chamber undergoes a complex remodeling that changes the shape of the ventricle and the architecture of the fibers in the myocardium. In order to effectively surgically reconstruct the heart it is necessary to understand the relative impact of these changes on heart function. Here we present a series of simulations that model different pathological changes separately. We use the sensitive relationship between twist of the ventricle and its ejection fraction to judge the functional impact of the different damage types. We show that the anomalies found in the relation between torsion and ejection fraction for dilated cardiomyopathy are predominantly caused by the damage to the architecture of the myofibrils of the heart, rather than gross geometry.

As the last step we show that this arrangement of muscle fibers is capable of producing high enough pressures to provide efficient pumping to the circulatory system.

Chapter 2

Computational models of heart pumping efficiencies based on contraction waves in spiral elastic bands

2.1 Introduction

The human heart is well known as a mechanical pumping device of amazing efficiency, but we do not completely understand it. But it is not widely recognized how simple are the questions for which we do not know the conclusive answers. Here is one example: Myofibrils can contract by at most 15% [16]. If we imagine, for the sake of estimate, that myofibrils surround the heart as planar loops, then a simple geometrical argument suggests that with circumference contracting to 0.85 of its length, the surrounded cross-sectional area, and, therefore, the internal volume contracts to $(0.85)^2 \approx 0.72$, i.e., by at most 28%. This estimate is in a stark contrast with the physiologically well known fact that at each beat the healthy heart ejects blood in the amount of above 50% of the left ventricle volume. Thus, there is a glaring paradox between the physiologically possible contraction of myofibrils and physiologically realized ejection fraction.

Biological pumping organs, including the heart, are complex multi-scale systems. The function of the heart involves intricate physiological, biochemical, biophysical, cytological, hydrodynamical and many other aspects [15]. We would like to emphasize that all these aspects, however important, cannot resolve the above mentioned simple geometrical paradox. Indeed, whatever happens on the cell scale and on a smaller scale, whatever happens on the scale of microns, cannot resolve the contradiction between the amount of myofibril contraction and volume ejection on the scale of several centimeters.

An important progress in understanding this problem was achieved in paper by Sallin [41]. It was shown by a geometrical argument that helical arrangement of fibers, as a matter of principle,

can help resolve this paradox. Indeed this way of thinking was launched by the discovery of helical arrangements of fibers in histological studies [20]. The helical arrangements have also been confirmed by more recent MRI studies [22]. However, it remains unknown how specifically the helical arrangement is used by nature to resolve the efficiency issue in the heart. One of the reasons for this uncertainty is that MRI used in work [22] does not differentiate the muscle fibers from inactive fibers, showing a very complicated network of helical fibers.

One of the approaches to understanding heart mechanics is through modeling. For the purpose of simulations, the complex arrangement of the helical fibers requires simplification. The most popular simplification is based on the idea that the myocardium is a series of shells that contain helical fibers with changing angles of orientation. Very significant resources are directed at modeling the heart with a variety of approaches, sometimes with a very high degree of computational sophistication [42, 43, 46]. Most of these models simply ignore the physiological constraint on the maximum myofibril contractility and assume that fibrils can contract by any desirable amount. In some such models, authors simply take the physiological ejection fraction as an input parameter [46]; as a result the strain in the fibers is much greater than possible in nature. Other models, while never taxing the contractile ability of the fibers, never achieve the physiological ejection fraction, instead focusing on other aspects of heart function [45, 51].

We believe that the key to resolving the pumping efficiency paradox is not just in the helical arrangement of the myofibrils, but in the way these helical myofibrils bundle together. At about the same time that the helical fibers were discovered, another histological study found that the muscle fibers seem to be arranged in a single bundle in the shape of a double helix [21, 55]. Recently, through new imaging techniques this histological evidence has been given more weight. Modern MRI technology, such as DTMRI, illuminate the actin in the muscle cells, thus imaging exclusively the muscle fibers instead of a combination of muscle and other tissues [23]. These images show a bundled arrangement that is closer to a one double helical muscle band configuration than to the popular shell model. Our goal in this chapter is to demonstrate how double helical arrangement of the myofibrils explains the physiologically achieved volume ejection fraction without overstraining the fibrils.

Helically arranged fibrils can also be seen in the images of embryonic fish hearts [5–7] where, however, overall geometry is much simpler – in the early stages of development the entire heart can be thought of as a cylinder surrounded by the helical fibrils. For the sake of comparison, we will reproduce all our model calculations for this simpler geometry.

For our purpose, the model does not require too many details, there is no need to incorporate any microscopic features, they only matter in determining the phenomenological parameters of our large scale model. Additionally, among the decisive simplifications we do not have to take explicit account of blood hydrodynamics.

We model the myocardium as an elastic band. The material of the band becomes active when it is excited, which can generate volume forces in its body. As a corner stone of our simulations we specify that at maximal excitation the material contracts by 15% in the direction of the fibers. Despite a long standing knowledge of the Purkinje network that excites the adult heart, the timing of the cardiac muscle response to excitation is still unclear [16]. To get around this issue we assume a simple linear response to excitation, but vary the excitation patterns in our simulations.

Besides checking the performance of our “model hearts” as pumps we also pay close attention to their dynamics. The dynamics of the adult heart is very important to its proper function [56]. Indeed the twist of the left ventricle can be used to judge the relative health of the heart [27–29]. Part of the reason twisting is so important is that it is used as a spring mechanism for rapid refilling. As a result the dynamics are more complicated than simply turning one way with the contraction and the other with the relaxation. There is a qualitative jerkiness to the twisting motion of the heart that can be seen in open heart surgeries. We use the existence of the twist as an benchmark to the appropriateness of the excitation pattern we pick.

The plan of this chapter is as follows. In section 2.2, we formulate our model in greater detail, and explain how we choose the values of its parameters. We also describe our way of computational implementation of this model and data analysis. In section 2.3, we concentrate on the results obtained using our model. First, we demonstrate the adult heart model’s ability to reach physiological maximal ejection fractions under the simplest of excitation schemes. Second, we show that there is no dynamical twist in either of the two models of the adult heart and embryonic tube heart in response to a step or a temporal wave excitation. Third, we find that the spatio-temporal wave excitation patterns are able to overcome this barrier without losing the pumping efficiency. We conclude with the discussion and outlook in section 2.4.

2.2 Methods

2.2.1 Geometries of muscle bands

Fibers in both the adult and embryonic heart form a complex matrix. In our models, we simplify this complexity by taking into account only the dominant bundles of the muscle fibers. To model the muscle fiber bundle it is necessary to know where it is in space and how it is oriented. We choose to describe this mathematically. To do so, we specify the centerline of the bundle. This centerline can be thought of as a single fiber, around which all of the other fibers will bundle. The shape of the centerline is roughly determined by averaged orientation of all fibers of the dominant bundle. Here, we mathematically describe the centerline using parametric equations in cylindrical coordinates- $[\theta, r, z]$, where we choose the circumferential coordinate (polar angle), θ , to be the parameter.

Once the centerline is determined, we describe the rest of the bundle by specifying the other

fibers to run parallel to the centerline: For every θ the new fiber is at a constant distance from the centerline at the same θ . To make sure that the new fibers do not cross, this is done by stepping away from the centerline in a direction that is perpendicular to the tangent of the centerline. In this work the muscle bundles we model have the shape of bands, meaning that the thickness of the bundle is much smaller than either the length or the width of the bundle. In our models, bands enclose pumping chambers by surrounding them with their wider side; that means the bands are orientated in such a way that the thickness is always taken to be in the radial direction. And the 3D band geometry is described in cartesian coordinates, $[x, y, z]$, with three parameters, θ along the length of the band, ξ along the width, and ζ in the thickness direction.

2.2.1.1 A simple tube

One of the simplest chambers we can enclose with a band is a tube. The fibers can be arranged circumferentially or longitudinally, or they could form a spiral about the tube. There are many examples in nature where there is a helical muscle structure, ranging from worms to embryonic fish hearts [5, 10, 57]. Such muscle bands can be easily described by a set of parametric equations. In cylindrical coordinates, $[\theta, r, z]$, the centerline of the spiral band is defined such that radius, r , is a constant, while z grows linearly with θ :

$$r = R, \quad z = R\theta \cot \alpha, \quad (2.1)$$

where α is the pitch (fiber) angle, and R is the radius of the cylinder. The polar angle θ parameterizes the curve and ranges, $0 \leq \theta < \theta_{max}$.

As it is known from differential geometry, the orientation of the centerline determines in each point a triplet of mutually orthogonal vectors (called Frenet vectors), namely tangent, normal, and binormal [58]. In our case, normal vector everywhere points in r direction away from the cylinder, while tangent vector and binormal vector have no r components and lie on the surface of the band, and their other components are given by:

$$t_\theta = \sin \alpha, \quad t_z = -\cos \alpha, \quad n_\theta = -\cos \alpha, \quad n_z = -\sin \alpha. \quad (2.2)$$

Based on the known equations for the centerline and its binormal, we can define a surface of a spiral band by simply stepping away by a small length along the binormal from the centerline. The thickness of the band is given by small variations in the constant R . The parameterized description of the 3D spiral with fiber angle α are then given in cartesian coordinates by:

$$z = r\theta \cot \alpha + \xi n_z; \quad x = (R + \zeta) \cos(\theta + \xi n_\theta); \quad y = (R + \zeta) \sin(\theta + \xi n_\theta). \quad (2.3)$$

The variables ξ and ζ identify the position within the band in the direction of width and thickness, respectively. These variables change in the range $-w/2 < \xi < w/2$ and $0 < \zeta < t$, where w and t width and thickness, respectively. The constants R , α , and θ_{max} , allow us to specify which parameters (cylinder radius, cylinder length, fiber length, cylinder volume) are to be kept constant. Different configurations of the spirals used in this work are shown in figure 2.1.

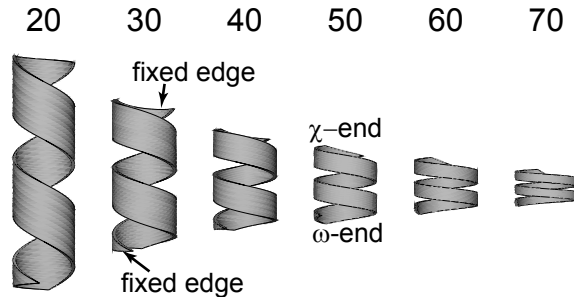


Figure 2.1: Images of the spiral muscle band models for the embryonic heart. The numbers indicate the pitch (fiber) angle, $\alpha = 20^\circ, 30^\circ, 40^\circ, 50^\circ, 60^\circ, 70^\circ$ are shown. For all the spirals shown here the radius of the tube is constant. The length of the band is also constant, and as a result the length of the tube varies with the pitch angle. The width of the band is taken to be half of the value that would have fully covering the surface of the tube, and as a result the width varies with the pitch angle. The edges that are fixed during simulations are shown on the spiral of $\alpha = 30^\circ$. On the spiral $\alpha = 50^\circ$ the ends of the tube are labeled corresponding to the start of spatial contractions at χ -end, and the end of contraction at the ω -end.

2.2.1.2 A two chamber structure

The adult human heart is a more complex structure than a tube, but its chambers are also bound by helical fibers. In order to explain our way of modeling this structure, let us first define the same nomenclature as used in heart physiology. There are two pumping chambers, the left and right ventricles. We can crudely describe the left ventricular volume as bounded by the left pulmonary surface on the outside of the heart and the septum on the inside. Likewise, the right ventricular volume is bound by the septum on the inside of the heart, and the anterior (sternocostal) surface on the outside. Importantly, this structure is not axisymmetric. In other words, when we introduce the z -axis, along the long-axis of the heart, directed from the apex to the center of the basal plane, it does not imply any rotational symmetry.

We describe the ventricular surfaces by introducing the polar angle θ in the horizontal plane perpendicular to the z -axis. For the left ventricular surface, we assume that its cross-section by the vertical plane going through the z -axis at any θ represents a parabola, $z = ar^2$, with parabola vertex at the heart apex, but with different, θ dependent coefficient: $a = a(\theta)$. Although the left ventricular surface is not completely axisymmetric, it looks roughly like a paraboloid, which means variations of $a(\theta)$ are not large throughout the closed surface, for $0 \leq \theta \leq 2\pi$. Part of this surface

represents the left pulmonary surface, while the other part - septum. Adjacent to the septum part, on its outer side, there is another surface, significantly more curved, which represents the anterior surface; it joins smoothly the left ventricle surface along the boundary of septum and left pulmonary surface, and extends significantly outwards in between (the latter means that, at the basal plane level, the horizontal distance from the long axis (or from the z -axis) to the middle of anterior surface is significantly longer than the distance from long axis to the middle of the septum). We do not need to specify any mathematical description of the anterior surface, because we do not plan to address the right ventricular volume. For simplicity, we will refer in this chapter to the left and right ventricular chambers shapes as non-axisymmetric paraboloid and half-paraboloid, respectively. The surfaces of the ventricular chambers can be seen as part of our model in figure 2.2A. In the heart these surfaces are formed by the fibers of the myocardium.

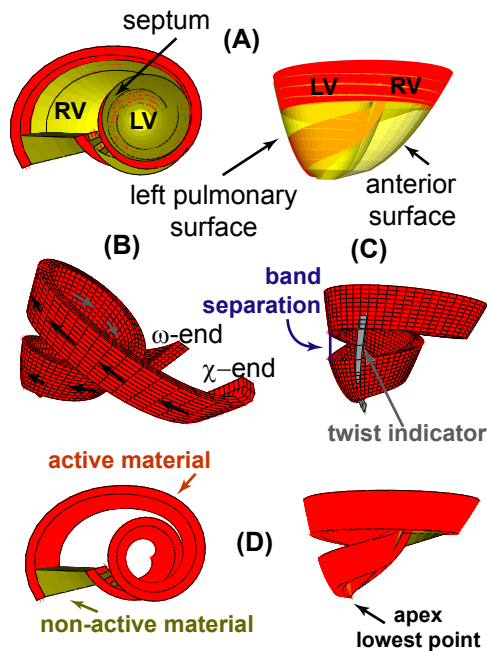


Figure 2.2: Initial band shape and fitted volume shown from different points of view. (A) The chambers for left ventricles (LV) and right ventricle (RV) are drawn in yellow. The left pulmonary and anterior surfaces, and the septum are indicated. The left ventricle is in the shape of a non-axisymmetric paraboloid, and the right ventricle is a half-paraboloid. The model band is shown in red on the surfaces of LV and RV. (B) The proposed double helix band is shown with the fiber angle indicated by the arrows. The ends of the band are labeled corresponding to the start of spatial contractions at χ -end, and the end of contraction at the ω -end. (C) The double helix band is shown from the back, with the separation between the loops indicated. This separation was picked, such that at minimum long-axis of the left ventricle the band would not impinge on itself. The soft material of the twist indicator is shown in grey. (D) The band in different orientation, with labeled active and nonactive material, as well as the apex of the heart. The non-active material that connects the two ends of the band is fixed in the horizontal plane, while the apex is fixed vertically.

There is histological evidence that the fibers are arranged in a spiral band, as shown by Torrent-

Guasp [21], who postulated that the heart muscle is a single band that starts from the pulmonary aorta, hugs the right ventricle, winds down to the apex, as the descending segment, and then spirals up to the aortic valve as the ascending segment. To mathematically describe this intertwined double helix we took the original physical model created by Torrent-Guasp and approximated its shape with mathematical equations. It is, of course, more complicated in terms of mathematical presentation than a simple spiral. Theretofore, as a first step we describe the orientation of the fibers by specifying the long-axis coordinate, z_{cent} , as a function of polar coordinate θ for the centerline:

$$z_{cent} = C_1 - C_2 \frac{\theta^{A_1}}{A_2} \exp \left[-\frac{\theta}{B_2} \right] \quad (2.4)$$

where C_1, C_2, A_1, A_2, B_2 are constants. The polar coordinate θ varies $\theta_{max} \geq \theta \geq 0$, where θ_{max} corresponds to the start of the band at the pulmonary aorta, and $\theta = 0$ corresponds to the end of the ascending segment. This interpolation formula is designed such that at large θ the change in z is dominated by the exponential factor, thus describing the fibers hugging the right ventricle; at small θ , z decreases sharply due to the power law factor θ^{A_1} , thus describing the ascending segment; at the cross-over range of θ the interplay between these two factors describes the descending segment.

The r -coordinate of the centerline should now be constructed in such a way that the centerline correctly skirts the ventricular surfaces, the non-axisymmetric paraboloid and half-paraboloid, which we discussed a few lines back. The simplest idea would be to take just the paraboloid $r_{cent} = \sqrt{(z_{cent} + C_3)/a}$, with some constant a (C_3 determines the position of 0 on the z -axis). However, we should keep in mind that the band and, therefore, its centerline in the adult heart has to make two turns around the heart's long-axis. That means, θ will have to change over the interval significantly longer than one full turn of 2π . Therefore, for the centerline skirting the paraboloid, there will inevitably be two points with the same r and the same z , corresponding to angles $\theta_{crossing}$ and $\theta_{crossing} + 2\pi$; and this will mean the physically meaningless self-overlap of the band at $\theta_{crossing} = \pi \left(-1 + \cot \frac{\pi}{A_1 B_2} \right)$. To avoid this self-overlap, we force the radii at these two points to be different by introducing the Factor 1 which bends the centerline away from self-crossing. We also introduce Factor 2, which is only significant in the region of anterior surface and describes the fact that this surface bends significantly outwards from the septum. An illustration of the resultant shape of the band if Factor 1 and Factor 2 were not included can be found in appendix D figure D.1. We choose the middle of anterior surface to correspond to $\theta_{right} = 3.8\pi$ and write:

$$\begin{aligned} r_{cent} &= \sqrt{z_{cent} + C_3} [\text{Factor 1}] [\text{Factor 2}], \\ \text{Factor 1} &= 1 + C_4 \cos \left(\frac{\theta - \theta_{crossing}}{2} \right), \\ \text{Factor 2} &= 1 + C_5 \exp \left(-(\theta - \theta_{right})^2 \right), \end{aligned} \quad (2.5)$$

where, C_3, C_4 and C_5 are constants. The constants of equations 2.4 and 2.5 are not independent when related to the geometry of the heart.

To make the mathematical description of the 3D shape of the band simpler, we approximate the direction of the width to be along the z -axis. The parameterized three dimensional structure is then described in cartesian coordinate, (x, y, z) , by:

$$\begin{aligned} z &= z_{cent} + \xi, & r &= \sqrt{z + C_3} [\text{Factor 1}] [\text{Factor 2}] + \zeta, \\ x &= r \cos \theta, & y &= r \sin \theta, \end{aligned} \quad (2.6)$$

where $-w/2 < \xi < w/2$ and $0 < \zeta < t$, with w and t are the width and the thickness of the band, respectively. The resulting structure can be seen in figure 2.2B.

2.2.2 Choosing the Geometrical Parameters

In both models, embryonic and adult heart, there is a range of parameters that can be varied. Some of the parameters were specified during the mathematical formulation of the model, others we varied in different simulations. We base the choice of parameters on physiological observations, the goals of the simulations, and computational needs.

2.2.2.1 Embryonic tube heart

Pitch angle: It is not possible to extract the pitch angle (fiber angle) from the images of the embryonic heart. We therefore wanted the ability to vary the fiber angle. In the experiments the angle is varied between $5^\circ \leq \alpha \leq 85^\circ$.

Radius of the tube: In the embryonic heart model the radius of the tube is known. Thus, we chose to keep the radius of the tube constant, namely $R = 0.25$ cm.

Number of turns: From the available images it is unclear how far up the tube the spiral fibers extend. Therefore we base our choice for the number of turns on the adult heart model – this ensures that the two models are easier to compare to each other. As a result, we specify for the spiral to make two full turns. In these simulations we specify it to go around another quarter of a turn, so that the boundaries do not impact the main body of the spiral. Therefore, $\theta_{max} = 4.5\pi$.

Length of the tube: Once the number of turns of the spiral, the radius, and the pitch angle are specified, the length of the tube is mathematically determined: $\{\text{Length}\} = \theta_{max} R \tan \alpha$.

Fiber length: Once the above parameters are chosen the fiber length is determined:

$$\{\text{Fiber Length}\} = \theta_{max} R / \cos \alpha.$$

Band width: The choice of the above parameters also defines the width of the band necessary to cover the whole surface of the tube. We chose for the width of the band to be limited to half of what would cover the tube, to insure that the material did not impinge on itself during twisting: $w = 0.25\pi r \cos \alpha$.

Band thickness: The thickness of the band is constant and small compared to the width:
 $t = 0.02\text{cm}$.

2.2.2.2 Adult heart

Unlike the constants that described the shape of the spiral the constants in equations 2.4-2.6 are given by a complicated relationship with physical quantities, so we will present their values where they first occur.

Number of turns: This parameter is dictated to be two turns by the histological evidence. This places the limit on θ_{max} to be 4π . We extend this a little to connect the two ends of the band:
 $\theta_{max} = 4.08\pi$.

Long axis dimension: The long axis dimension is taken to be the same as in the normal adult heart, about 7 cm. Therefore, in equation 2.4 the constant $C_2 = 7$.

Fiber angle: Unlike the pitch angle of the simple spiral, the fiber angle is not constant in the double helical arrangement. We took the information from the histological studies done by Torrent-Guasp [17, 21]. The fiber angle dictates the formulation of equation 2.4 and the values for the other constants are: $C_1 = 4.9$, $A_1 = 1.3$, $A_2 = 0.5$, $B_2 = 2$. The fiber orientation differences in the thickness of the myocardium at the crossing point dictates that in equation 2.5 the constant $C_4 = 1/6$. The fiber orientation at the apex is also dictated by the position of the vertex on the long axis: $C_3 = -0.77$.

Basal radius: The basal radius of the left ventricle is taken to be the same as in the adult heart, about 3.5 cm. This is also inherent in the parameters described above.

Right heart size: The parameter controlling the size of the right heart, was estimated so that the fitted right ventricle volume would correspond to the volume in a normal adult heart (about 130 mL): $C_5 = 1$ in equation 2.5.

Band width: To ease computation the band width is assumed to be a constant. The width is chosen ($w \approx 2.5$ cm) such that the bottom of the mitral left segment does not impinge on the top of the descending segment during maximal contraction. The separation between the two parts of the band are shown in figure 2.2C.

Band thickness: The thickness of the band is constant and small compared to the width ($t \approx 0.5$ cm).

2.2.3 Material properties

The properties of the material of the organ’s muscle are inevitably dictated by the muscles building blocks – muscle cells. The muscle fibers contract along the length of the fiber, thus the muscle band, which consists of a group of parallel muscle fibers, will contract in the same direction. The cells cannot contract over 15%, and thus the band will not exceed this maximum shortening ratio at any point along its length. To conserve volume, while it is shortening in the fiber direction the band will expand in the other two. The band can contract as a whole, or parts of it can shorten independently of each other. That means that the cells can act separately along the length of the fiber and the fibers in the width of the band can contract at different times from each other. For simplicity, we assume a linear elastic response while the material is not excited. The material is incompressible, so the maximal computationally possible Poisson ratio is chosen, $\nu = 0.48$ (an ideal incompressible material has $\nu = 0.5$). The only forces in these models are those produced by the active material, so we choose to normalize all the stresses by the Young’s modulus, E_Y , of the muscle fiber. Therefore, the Young’s modulus for any material included in the model is described in terms of E_Y of the active material.

As regards to the structure of the adult heart, it would have been impossible to model the double helix without the band coming into contact with itself. Indeed, in some areas of the ventricles the interaction between the material with different fiber direction is very important as illustrated by other works [46]. It was, therefore, necessary to insert a few pieces of the collagen matrix, a non-active material, to make the model applicable. The non-active material was chosen to be four times softer than the active material, i.e., the Young’s modulus of the non-active material is one fourth of the Young’s modulus of the active material. One piece of collagen is placed at the cross over point connecting the band at $\theta_{crossing}$ and $\theta_{crossing} + 2\pi$. The other piece is used to connect the two ends of the band, i.e., between $\theta = 0$ and $\theta = 4\pi$. The collagen pieces are labeled in figure 2.2D in green.

2.2.4 Boundary conditions

Our models are not part of a whole organism, so there is no vasculature to hold them in place. It is, therefore, necessary for us to fix them in space, otherwise in response to the force produced by excitation, the structure will gain acceleration and fly away. To do that we need to constrain at least three degrees of freedom.

2.2.4.1 Embryonic tube heart

We found that the most meaningful behavior is obtained by fixing both ends of the tube (shown in figure 2.1 for 30° pitch angle). This allows us to consistently look at pumping in a range of different contraction schemes. If only one end of the tube is fixed, the other flaps about, which makes it hard to determine the internal volume.

2.2.4.2 Adult heart

In order to easily compare the medical data on heart twist to the dynamics of our model, we wanted to fix the model in space by the same rules as are observed in nature. In the body, the top of the heart does not rotate, while the heart's apex does not move up or down. Therefore, the band structure is fixed in the horizontal plane by restraining the non-active material in the x - y -directions, in the same manner as the heart is constrained by the vessels. The lowest point of the double helix is assumed to be the apex, and is constrained in the vertical z -direction (figure 2.2D).

2.2.5 Different Excitation schemes

To begin with, let us consider what happens to the active material when it is excited. In the language of solid mechanics the deformation of the band will be described in terms of strains, ε , along the fiber direction and in both perpendicular directions. Since maximal contraction in response to excitation is 15%, the minimum strain in response to activation would be -0.15 . We express the strains in response to excitation as $\varepsilon_{fiber}^{Ex} = 0.15Ex$ in the fiber direction and in both perpendicular directions as $\varepsilon_{perpend}^{Ex} = -0.085Ex$. Here, the excitation factor, Ex ranges between 0 for no excitation and -1 for a full excitation. If the structure is constrained the activation will induce stress. For example in the fiber direction the stress of a fully constrained structure would be $\sigma_{fiber} = E_Y \left(\varepsilon_{fiber} - \varepsilon_{fiber}^{Ex} \right)$, where ε_{fiber} is the total strain in the fiber direction. This means that the excitation factor, Ex , is the only input which activates the model, and drives its deformation.

The simplest dynamic scheme is to excite all the cells at the same time and have the fibers contracting in sync – making a uniform contraction. We also apply a wave-type excitation to our models. Of course, in creating waves there are a lot of degrees of freedom. We can change the duration of the excitation, the length of the wave, the origin point of excitation, etc. For a band, some of the simpler waves would be one dimensional. To ease the explanation let us label one end of the band χ and the other ω (these are labeled on figure 2.1 for pitch angle 40° and in figure 2.2B). A one dimensional contraction wave would then be described as originating from end χ of the band and traveling to end ω . This means that all the elements in width and thickness, the ones at the same centerline natural coordinate, will contract and relax together. For ease of comparison to the uniform contraction, where all the elements are contracted together, we create a wave that has the

contraction front traveling from end χ of the band to end ω . Once the contraction front reaches the ω end of the band, the relaxation front starts from the original χ end. This means that there is one instance of time where the whole band is contracted. To contrast this long wave, we also run a simulation where the wave is shorter and the relaxation front starts before the contraction front reaches the ω end. The excitation factor (Ex) is then dependent on both time, t , and the band coordinate, s , and can be approximated by the following piece-wise linear interpolation:

$$\text{Ex}(s, t) = \begin{cases} 0 & : t < t_1 \\ \frac{-(t-t_1)}{t_2-t_1} & : t_1 \leq t < t_2 \\ -1 & : t_2 \leq t < t_3 \\ \frac{-(t_4-t)}{t_4-t_3} & : t_3 \leq t < t_4 \\ 0 & : t \geq t_4 \end{cases} \quad (2.7)$$

$$t_1 = \frac{L_1}{s_{max}}x, \quad t_2 = \frac{L_1}{s_{max}}x + T_1, \quad t_3 = \frac{L_2}{s_{max}}x + T_2, \quad t_4 = \frac{L_2}{s_{max}}x + T_3,$$

where s_{max} is the length of the band, and L_1, L_2, T_1, T_2, T_3 are constants that determine the shape of the excitation wave. Figure 2.3 shows a graphical representation of the excitation patterns used in this work. The x -axis on this plot shows the coordinate on the band, s . End χ is considered the origin at zero, and end ω is the end of the band at 100% of the bands length (s_{max}). The y -axis shows time. To read one of these contour plots, you can draw a horizontal line at the time of interest, then at each point on the band you will find a color that represents the degree of contraction (blue - contracted, red - relaxed). The following is a description of each excitation pattern and the constants corresponding to it:

Step excitation: For a uniform contraction $L_1 = L_2 = 0$, and thus there would be no dependence on the spatial variable. The other constants were taken to be $T_1 = 0.4$ sec, $T_2 = 0.7$ sec, $T_3 = 1$ sec. See the contour plot for this wave in particular in figure 2.3A.

Long spatial wave excitation: For the full band length wave the constants are $L_1 = L_2 = s_{max}$, $T_1 = 0.005$ sec, $T_2 = 0.45$ sec, $T_3 = 0.5$ sec. See the contour plot for this wave in particular in figure 2.3D.

Medium spatial wave excitation: For a spatial wave shorter than a full band length the constants are $L_1 = L_2 = 1.2s_{max}$, $T_1 = 0.005$ sec, $T_2 = 0.375$ sec, $T_3 = 0.4$ sec. See the contour plot for this wave in particular in figure 2.3C.

Shifted long wave excitation: For the shifted long wave the constants are $L_1 = 0.4s_{max}$, $L_2 = 0.95s_{max}$, $T_1 = 0.005$ sec, $T_2 = 0.275$ sec, $T_3 = 0.325$ sec. See the contour plot for this wave in particular in figure 2.3E.

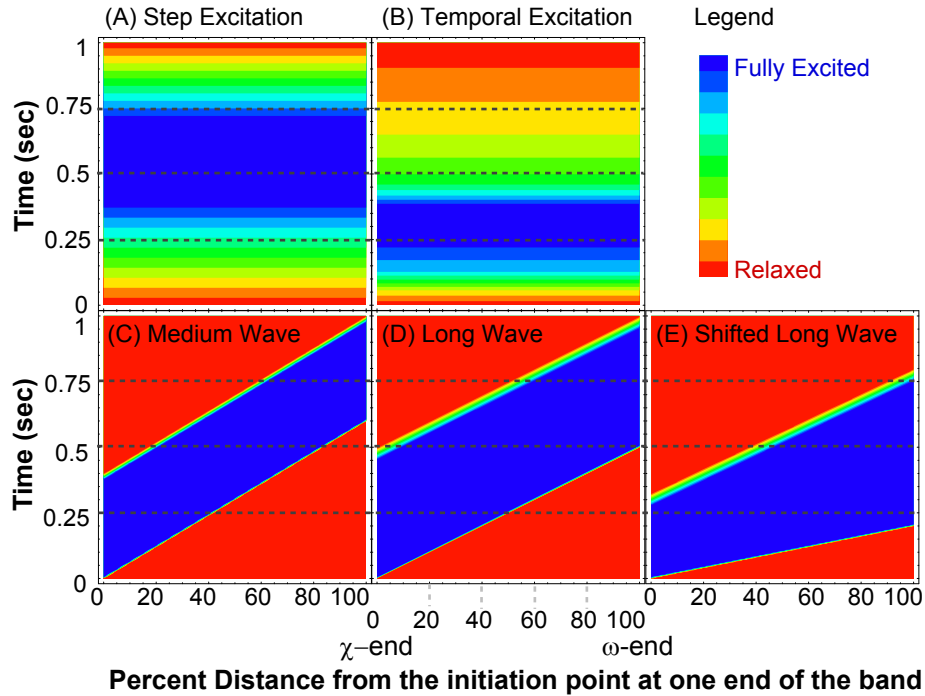


Figure 2.3: Parametric plots for five excitation waves. To read these plots follow a horizontal lines, at a time of interest, the color at the position of the band indicates the contraction state. The scale at the top right corner shows the legend with red-relaxed and blue-fully contracted. At the top are plots for uniform excitation schemes, where the whole band contracts at once. At the bottom are plots of spatial wave excitation schemes, where the excitation wave starts at χ -end of the band and travels to the ω -end of the band. (A) A step excitation, with the whole band being excited rapidly, and held at the fully excited state for 0.5 seconds. (B) A temporal excitation, with the whole band excited gradually - mirroring the change in volume of the physiological left ventricle. (C) Medium Wave, the band is never contracted all at once. (D) Long Wave, at 0.5s the band is fully contracted. (E) Shifted Long Wave, the speed of the excitation and relaxation fronts are adjusted, such that the full excitation occurs earlier (0.25s).

Temporal excitation: For the temporal wave, there was no dependance on time, and the activation was described by a table with linear approximations between values. See the contour plot for this wave in particular in figure 2.3B.

Time (sec)	Excitation
0	0
0.055	-0.25
0.09	-0.50
0.13	-0.75
0.225	-0.938
0.375	-1
0.415	-0.75
0.47	-0.50
0.545	-0.375
0.66	-0.25
0.83	-0.125
1	0

2.2.6 Computational methods

To enable spatio-temporal excitation it is necessary to allow different parts of the band to contract independently. This creates a complex coupling between local small deformations and large global shape responses, making it a challenging modeling problem. Another difficulty is that we are considering three dimensional geometries. To combat these problems, we utilize finite element analysis. It is possible, with small quadrilateral elements, to build very complicated shapes. The finite element method also breaks down a complicated problem of the dynamics of a complicated system in response to excitation into a set of manageable equations. Since this set is very large, it behooves us to use the computing power available to solve it. We therefore, model these bands using a finite element package, ABAQUS/Standard, designed to handle such problems. In the finite element code we use ABAQUS built in tools to independently “excite” each node, and when the nodes of an element are “excited,” the element contracts in the longitudinal fiber direction.

Please note that the finite element formulation of these models forces the s band coordinate in equation 2.7 to be discrete. The effects that this has on the results can be easily seen by varying the number of elements along the band. However, with the large number of elements used here (over 3000), the effect is very small compared to the overall changes in the structure.

2.2.7 Data Analysis

In this work we do not model fluid. If the blood was included it would be necessary to add valves to the chamber. Otherwise, most of the blood pumped during a contraction would flow back during relaxation. As a result, the pump would be very ineffectual. Therefore, for our simulations we simply

assume that the valves are present. This assumption implies that if the volume of the chamber is increased, there will be blood sucked into the pump from the inlet. When the volume of the chamber is decreased, the blood is forced out through the outlet. Therefore, we can simply keep track of the volume that would fit inside the spiral to calculate the effectiveness of the pump.

For the purposes of calculating the volume, the results from the ABAQUS/Standard analysis were processed with Fortran and Matlab code. To define the bounding surface, we extract the position of each node of the inner surface of the band for each time step. For the embryonic model the pumping chamber in its initial state is approximated as a cylinder. Although during the deformation the radius of the chamber varies with the z -coordinate, the chamber as a whole can still be approximated as a figure of revolution. When considering finite elements we view every small layer dz as a cylinder. The volume of the whole chamber is then the sum of the volume of all these cylinders.

For the adult heart model, the double helical band, the left ventricle volume was described in section 2.2.1.2. We assume that this general description of the left ventricular chamber as a non-axisymmetric paraboloid is valid throughout the deformation. Therefore, as the chamber deforms, the parabolic parameter $a(\theta)$ changes. In finite element formulation the chamber is broken into small polar sections of $d\theta$. Each slice is bounded by a piece of paraboloid and two vertical planes intersecting at the long-axis. The volume of the left ventricle is calculated by adding the volumes of each of the $d\theta$ slices.

To measure the pumping, volume reduction, efficiency of the pumps we calculate the ejection fraction, EF. For the tubular model we use a generic formula:

$$EF(t) = \frac{V_{\max} - V(t)}{V_{\max}}, \quad \text{and} \quad EF_{\max} = \frac{V_{\max} - V_{\min}}{V_{\max}}, \quad (2.8)$$

where, $V(t)$, V_{\max} and V_{\min} are the volume at time t , maximum volume and minimum volume of the chamber, respectively. For the adult heart model we use the same formulation as is used in the medical field:

$$EF(t) = \frac{V_{\text{initial}} - V(t)}{V_{\text{initial}}}, \quad \text{and} \quad EF_{\max} = \frac{V_{\text{initial}} - V_{\min}}{V_{\text{initial}}}, \quad (2.9)$$

where, $V(t)$, V_{initial} and V_{\min} are the volume at time t , initial volume and minimum volume of the chamber, respectively. Note, that the initial volume is the end-diastolic volume, and the minimum volume is the end-systolic volume.

We use ABAQUS/CAE to look at the dynamical aspects of the simulations. To ease the visual comparison we fix a strip of material to the outside of the left ventricle. The strip is made from a very soft elastic non-active material (Young's modulus two orders of magnitude less than that of the other inactive material). As a result the strip has no effect on the deformation of the structure

as a whole. The presence of twist can be judged by the deformation of this strip, like temperature is judged by the use of a thermometer. Initially the strip of material is in an $r - z$ -plane. During the contraction of the chamber the long-axis shortens, as a result the deformation of the strip will always have a component in the plane. If the strips deforms out of the plane there is twist in the left ventricle. If during deformation it remains in the plane there is no twist.

To look at the dynamical aspects of the embryonic model we include an outline of the original configuration for comparison. As a result it is possible to see changes in pitch angle, i.e., twist.

2.3 Results

In this work we look at two types of models - a double helical adult heart model and a simple spiral embryonic tube model. Each model is subject to different excitation schemes. For the embryonic heart there is very little data for comparison. Indeed, while, it has been found that there are helical fibers in the embryonic heart tube, there is no data for the pumping efficiency under different conditions. By contrast, for the adult heart there is a large volume of data for comparison with the model results. Consequently, we guide our exploration of both models, by comparing the adult heart model results with medical data.

	Contraction Type				
	Physiological	Step	Uniform Temporal	Medium Spatial Wave	Long Spatial Wave
EF_{\max}	50%-60%	54%	54%	53%	54%

Table 2.1: The ejection fraction values for double helical pumps under different excitation patterns

2.3.1 Step excitation

In considering helical structures let us begin with looking at the simplest possible excitation scheme – a step excitation. In this scheme the whole band is excited at once, leading to an immediate contraction of all elements.

We first looked at how the double helical adult heart model responds to this type of excitation. Table 2.3 shows the maximal ejection fraction for this type of contraction. In this case the maximum ejection fraction is 54%. This is well in the range of normal physiological values of 50% – 60%. However, as can be seen in the plot of figure 2.4A, in a step contraction the volume changes in a completely different manner from the physiological. As a consequence, it is unsurprising that the dynamics of the left ventricle in this model has no visible twist. This effect is illustrated in the snapshots of the simulations in figure 2.5. We next looked at how the tubular model was affected. Like in the adult heart model there is no visible twist (figure 2.6). In figure 2.7 the maximal ejection

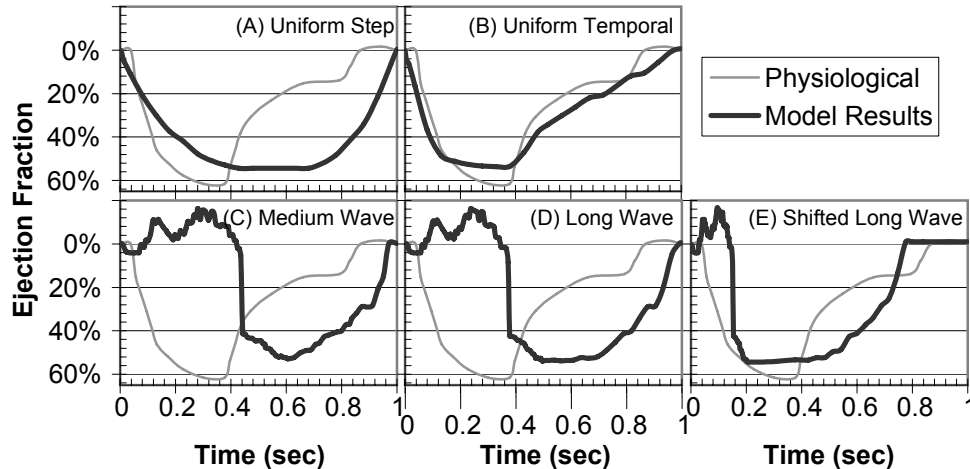


Figure 2.4: The left ventricular ejection fraction vs. time for adult heart model subject to different excitation patterns. The ideal physiological data taken from [15] is drawn in grey for comparison with model data in black. (A) Uniform Step excitation: the maximal ejection fraction is sufficiently close to physiological, but the speed with which it increases and decreased is completely different from physiological. (B) Temporal excitation: Both the maximal ejection fraction and the shape of the response are close to ideal physiological. (C, D) Medium and Long spatial waves: The maximal ejection fraction matches physiological needs, but it occurs at 0.6s instead of 0.38s. The shape is different, with the initial increase in volume, and the initiation of pumping at 0.4s. The medium wave response has more rapid filling than the long wave. (E) The shifted long wave: The maximal ejection fraction timing is shifted quite close to physiological.

fraction as a function of pitch angle for this excitation pattern is shown in dark blue. These results never top the 28% that would be possible with circumferential fibers. The only surprise is that at very low pitch angles the ejection fraction starts to increase instead of going to zero as we expected (see appendix A.1 for analytical calculations for non-helical fibers). This happens because in these models the fiber length and θ_{max} are kept constant. As a result for pitch angles below 20° the length of the tube is so much larger than the radius that the structure buckles in the middle to reduce stress, making the volume appear larger. This effect is unlikely to be of any biological significance, because in reality the muscle band is encased in a collagen matrix.

2.3.2 Temporal excitation

To fit the model's left ventricular ejection fraction evolution with time to the physiologically observed throughout the course of a beat, we apply a temporal excitation. In this activation scheme, the excitation factor is approximated directly from physiological data, $Ex(t) \approx -EF^{physio}(t)/EF_{max}^{physio}$.

As a result, the maximal ejection fraction remains unchanged, at physiological value of 54%. The plots of the ejection fraction vs. time in figure 2.4 show that using this method we can reproduce how the left ventricular volume changes with time in real physiological experiment. However in the snapshots of the simulation no significant twist is visible (figure 2.5).

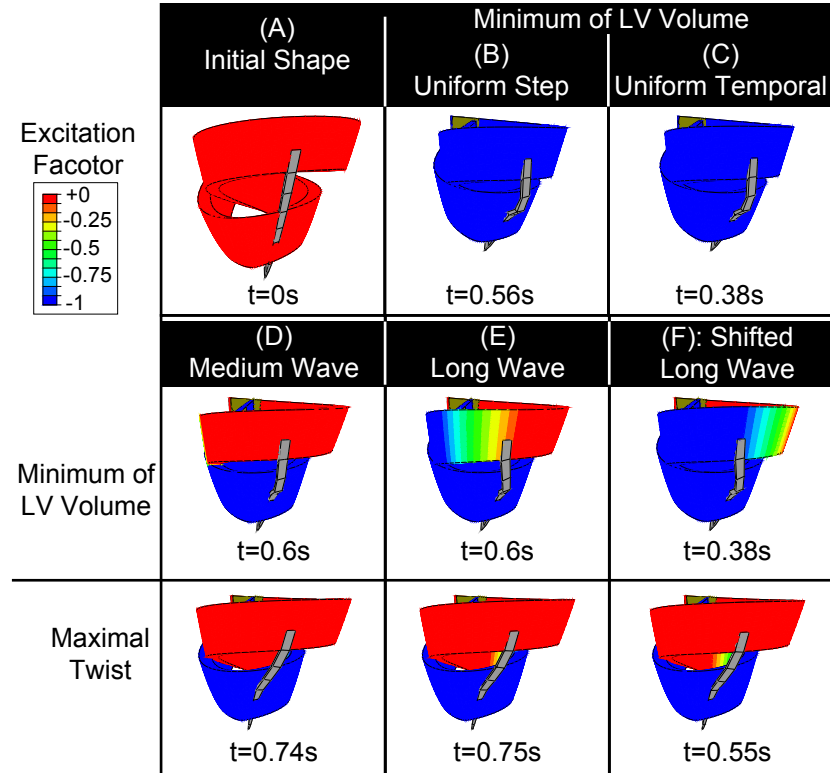


Figure 2.5: Snapshots of the movies for the adult heart model. The legend for the excitation factor is at the left (red-relaxed, blue-contracted). For each type of excitation discussed in this chapter we show the snapshots of the time at which LV volume was at a minimum. The presence of twist can be qualitatively judged by the out of plane deformation of the grey twist indicator. For the uniform excitation, no out of plane movements can be seen at any time. The models subject to the spatial excitation have twist indicator deformations out of plane. To showcase this, we provide another series of snapshots for the spatial wave excitations for times at which the twist was maximal (bottom panels). (A) Initial shape at time, $t = 0s$. (B) Uniform step: Minimum volume at $t=0.56s$. (C) Uniform temporal: Minimum volume at $t=0.38s$. (D) Medium wave: Minimum volume at $t=0.6s$; Maximal twist at $t=0.74s$. (E) Long wave: Minimum volume at $t=0.6s$; Maximal twist at $t=0.75s$. (F) Shifted long wave: Minimum volume at $t=0.38s$; Maximal twist at $t=0.55s$.

For a tube this type of excitation produced no significant differences in results when compared to the step excitation (shown in figure 2.7 in violet and blue). Any variations are slight and due to the time step - the time at which the maximal contraction occurs is in between sampled time steps. Figure 2.8 shows this difference between the response to the step and temporal excitations for a spiral with pitch angle of 60° , in blue and violet, respectively. Practically, the only difference in the response to the temporal excitation and the step excitation is in the timing. This makes sense, since the only variation we introduce for the temporal excitation is in the timing of the excitation. As a result it is unsurprising that, qualitatively, we cannot see any type of twist (figure 2.6).

To summarize, there are two problems with this type of contraction: First, we do not see any dynamic twist in the adult heart simulations, which we know is an integral part of a healthy heart.

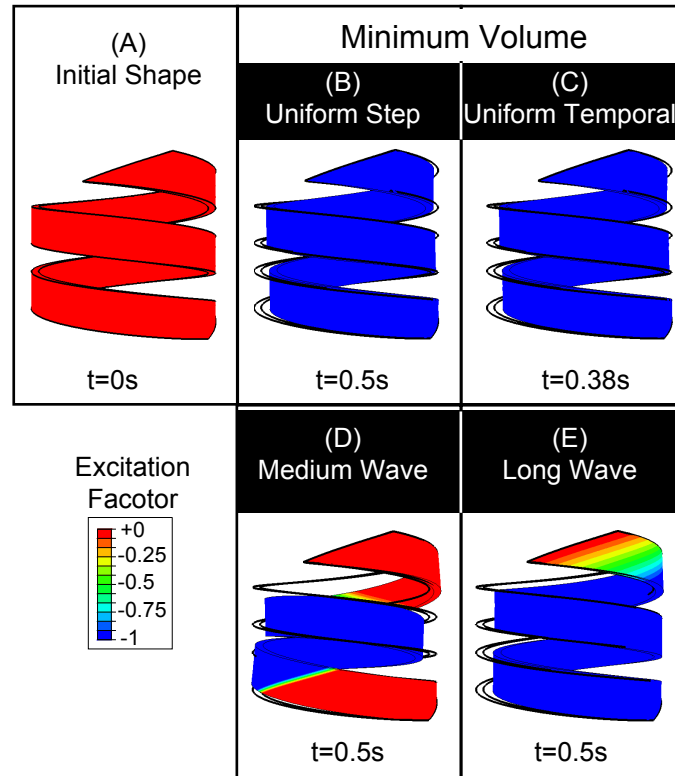


Figure 2.6: Snapshots of the movies for the embryonic heart model. The legend for the excitation factor is at the left on the bottom (red-relaxed, blue-contracted). For each type of excitation discussed in this chapter we show the snapshots of the time at which LV volume was at a minimum. The presence of twist can be qualitatively judged by comparing the initial band outline (thicker black lines) to the current shape. For the uniform excitation, no change in centerline angle can be seen at any time, i.e., only the radius of the spiral changes. The models subject to the spatial excitation have twist, which is indicated in the shift of the band away from the original outline. (A) Initial shape at time, $t = 0s$. (B) Uniform step: Minimum volume at $t=0.5s$. (C) Uniform temporal: Minimum volume at $t=0.38s$. (D) Medium wave: Minimum volume at $t=0.5s$ (E) Long wave: Minimum volume at $t=0.5s$;

Second, this is an unrealistic type of contraction. In biology the muscles will either be excited or not; it is unlikely that a muscle cell would have such a complicated response to an excitation.

2.3.3 Spatial wave excitation

To resolve these problems we try a spatial wave excitation. For the purposes of this work we try a simple wave that starts at one end of the band and moves to the other, as described in section 2.2.5. A wave contraction is also very flexible in terms of easily imaginable compensation mechanisms available in case of damage.

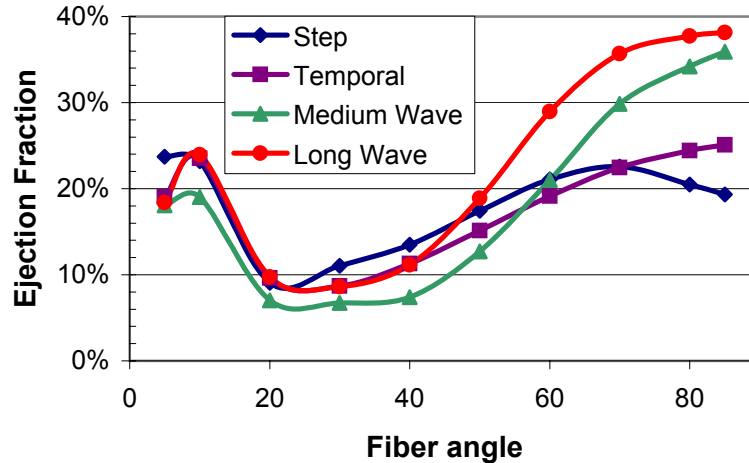


Figure 2.7: The dependence of the ejection fraction on the pitch angle for four different contraction schemes for a tube spiral geometry. Step excitation - blue, Temporal excitation - violet, Medium spatial wave - green, Long spatial wave - red. For pitch angles above 50° the spatial waves can achieve better ejection fractions than the uniform contractions. For pitch angles of 70° and above, it is possible to overcome the 30% ejection fraction possible with circumferential fibers.

2.3.3.1 Simple spatial waves: Adult Heart

The snapshots in figure 2.6 show that wave-type contractions produce a qualitatively visible twist. This twist, once calculated, can be used to judge independently from the volume-time relationship whether the excitation pattern is physiological. But how was the pumping ability affected?

The range of maximal ejection fractions for the adult heart model subject to different spatial wave contractions is 53% – 54%, which is within the physiological range. Figure 2.4D show how this simple constant speed spatial wave excitations produces a complicated volume reduction response. We performed calculations for a broad range of values of the wave length $((L_2T_3 - L_1T_2)/s_{max}$ in equation 2.7 above). The ejection fraction results for the medium length wave (figure 2.4C), show that maximal ejection fraction was not impacted. In general, we found that the reduction in the length of the wave does not negatively impact the maximal ejection fraction until the wave is shorter than the portion of the band that defines the left ventricle. However, there are some significant differences between the responses of the model to the simple spatial wave excitations and physiological data, as we show and discuss below.

2.3.3.2 Timing of maximal contraction: Adult Heart

The simplest spatial excitation, the long wave, makes our model to respond in such a way, that the maximum ejection fraction is timed differently from the physiological response – it is late by 0.2 s. Obviously, this is caused by the speed of the contraction and relaxation wave fronts, which we chose arbitrarily. Thus, it is easy to fix by varying the speeds of the wave fronts. Figure 2.4E shows the

model response to a full length spatial wave with a different speed of the contraction and relaxation wave fronts (shifted long wave). In this case the maximal ejection fraction is timed quite closely to the physiological maximal contraction.

2.3.3.3 Initial increase in volume: Adult Heart

Another discrepancy between the model's response to the long wave excitation and the physiological behavior is that for the first 0.3s the volume increases from the diastolic value, which does not happen in a real heart (figures 2.4C, 2.4D). The initial increase in volume is due to the helical nature of the band. When one end of the band is activated, it pulls on the portion of the band that bounds the left ventricle, increasing its volume. Our preliminary results (not shown) indicate that this initial increase in volume can also be adjusted, or taken out altogether, by making the spatial wave a little more complicated.

2.3.3.4 Simple spatial waves: Tube

When the spatial waves are applied to the spiral of the embryonic heart model the results are surprising. Figure 2.7 shows the maximal ejection fraction as a function of fiber angle for the long and medium spatial waves in red and green, respectively. At some pitch angles, if a helical structure is combined with a wave-like contraction, it is possible to exceed the maximal ejection fraction of the uniform excitation. Additionally, it is possible to overcome the limit on maximal ejection fraction previously achieved only with circumferential fibers (appendix A.1). The possibility to achieve over 28% ejection fraction without contracting the entire band at once could be beneficial in nature where muscle fatigue comes into play. But what is the mechanism behind the higher efficiency?

2.3.3.5 Pumping with suction: Tube

The plot in figure 2.8 shows how the volume of the tube with the spiral subject to spatial wave excitations initially increases. This is in contrast to uniform excitations, which have no initial increase in volume. Note, that while the increase in volume is the same for both the long and medium spatial wave excitation, the long excitation achieves a smaller minimum volume. This happens because in both types of excitations initially the activated end of the band pulls open the other end. However, the long spatial excitation wave contracts the whole spiral, which in the end produces a larger contraction compared to the initial configuration.

Since we assumed that the valves were present, the effect of initial increase in volume creates suction. Thus, during the initial stages of the contraction the volume increases, leading to a higher change in volume overall. The mechanism for suction here is different from the one observed in embryonic fish hearts early in their development [5]. In paper [5], the embryonic hearts acted as an impedance pump. The impedance pumping that produces the suction is caused by the dynamical

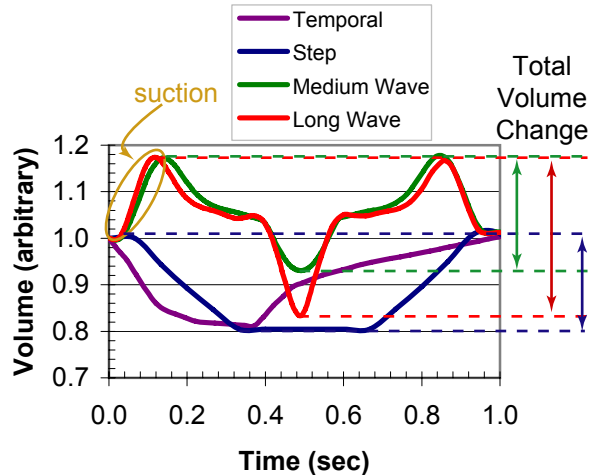


Figure 2.8: The volume evolution with time for four different excitation schemes applied to a spiral with a pitch angle of 60° . Step excitation - blue, Temporal excitation - violet, Medium spatial wave - green, Long spatial wave - red. The area where the volume is initially decreasing for models subject to spatial wave contractions is labeled as suction in yellow. The overall change in volume is indicated at the right. Here it is possible to see, that because of the suction effect the spirals driven by spatial wave excitations due a better job at pumping than the the spirals driven by uniform excitations.

movements of the spiral, which is seen in our model for most pitch angles with spatial excitation. At this point, it is impossible to know if the effect of suction from combining the helical nature of muscle fibers and a spatial wave excitation is used in embryonic pumping. It would be interesting to see what pitch angles the muscle fibers in the embryonic heart have and if the helical shape depends on the presence of valves.

2.4 Conclusions

Helical designs in living creatures are generally appreciated for their static structure, rather than the dynamics. In this respect, Torrent-Guasp model is distinct where a strong functional relationship between the heart's pumping function and its spiral muscle structure as a single band is proposed. By avoiding the complexity of modeling the whole structure at once, including all of the collagen and blood, we show that this simple band structure is akin to an engine behind the heart pumping action, for both a simple tube like the embryonic fish heart and a two ventricle pump.

In this work we have shown that it is possible to capture the adult's heart left ventricular volume evolution with time using a double helical model. This includes reproducing the maximal ejection fraction observed physiologically. The fact that we capture the maximal ejection fraction without overstraining the fibers is unique to this double helical model. However, this type of activation is biologically unrealistic and produces no dynamical twist of the left ventricle. Conversely, by activating this double helical structure with a spatial excitation, we can produce a visible left ventricular

twist without losing our ability to capture the proper ejection fraction.

We have also shown that there is no benefit to helically arranged fibers in a tube-like embryonic heart unless the muscle cells are activated with a spatial wave excitation. This combination, also produces a dynamical twisting response, which might play a part in other pumping mechanisms.

By coupling this band like helical structures of the myocardium with a wave-like contraction schemes it is possible not only to exceed pumping efficiency expectations, but to take advantage of the dynamics such a system can provide. The beauty of this model is in its simplicity, which leads to great flexibility. We realize that a real cardiac system involves many factors on a lot of scale levels that have not been accounted for here, but because our model captures some of the important properties of these biological systems, such factors as the calcium excitation, the presence of different types of muscle cells, collagen, blood, and complicated excitation patterns, can now be treated as additions to the already constructed solid base.

Chapter 3

Physiology in phylogeny: Modeling of mechanical driving forces in cardiac development

3.1 Introduction

In pursuing the evolutionary history, or phylogeny, of the heart we look for common characteristics between the embryonic and adult hearts. One pronounced similarity is in the helical organization of the muscle fibers. The simple helical organization of the fibers has long been observed histologically [20]. Moreover, there is some evidence that the muscle fibers, unlike the collection of fibers that includes collagen, are in a double helical bundle. This has been observed in a controversial illustration where the collagen is removed from the heart by boiling [21, 59]. While the idea that such a band exists was formed on the basis of disputed histological evidence, in recent DTMRI studies done by Helm et al. one can easily identify the band architecture (figure 3.1) [23]. This is significant, because this method images the actin, which is present in muscle fibers, but not in the collagen matrix or any other part of heart tissue.

By Ernst Haeckel's premise that ontogeny follows phylogeny, researchers use embryonic fish heart as a biological model for the human embryonic heart [5, 6]. By keeping track of the fluorescent myocardial cells, it is possible to create a picture of their movement during a heart beat. The resulting looped movement is not symmetric, forming an oval for each cell. The long axis of these ovals has to be aligned with the direction of the fiber, since that is the major direction of the contraction. The directionality of the oval paths of the myocardial cells is not constant throughout the heart tube. The only way, that a muscle fiber could have such a non-constant direction as seen in the images is if it was helically arranged [7, 8]. These fibers are not only helically shaped but they seem to be bundled into a band. Thus, both the adult heart and the embryonic heart seem to be comprised of helical muscle bands. How are these two observations related?

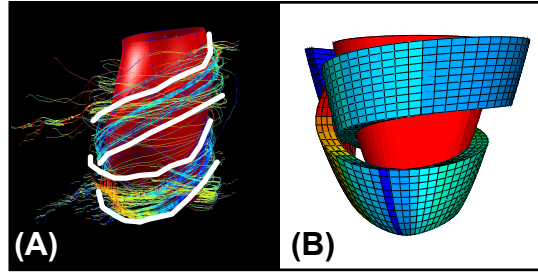


Figure 3.1: Images of the muscle fibers in the heart contrasted with the band model. (A) DENSE MRI image of the muscle fibers in the myocardium given to us by Helm. The muscle fibers are color coded for the value of the pitch angle; blue - horizontal to red - vertical. The red structure in the middle indicates the endocardial surface and represents the left ventricle volume. We overlay white lines on the image to indicate where the band lies. The muscle fibers are more horizontal at the top band section, while at the left section of the bottom band they are more vertical and are accordingly colored yellow and red. (B) The double helix model, color coded in the same manner as the DTMRI images. Blue for horizontal pitch angles to red for vertical pitch angles. The model band repeats the same pattern as the muscle fibers in the DTMRI images - the top portion of the band is dominantly horizontal, while the left section of the bottom portion of the band is going sharply up. The red structure inside the band is the modeled left ventricular volume.

3.1.1 Some Hints from Embryonic Heart Development

In the embryo, the heart muscle fibers start as a simple spiral, but as the embryo develops, the fibers transform into a more complex double helical structure. It would be interesting to track how this development occurs, and how it is reflected in the fiber arrangement of the adult heart.

In general we can imagine a transformation, intriguing in its simplicity, which can be performed on the helix of the embryonic heart converting it to the double helix shape of the adult heart. This transformation is easy to perform on a ribbon (figure 3.2). Of course, there is a world of difference between deforming ribbons and the actual heart muscle. So how does nature achieve this transformation?

3.1.1.1 The development of the heart

The embryonic heart in the beginning stages of its development is a tube with two sulcus [4]. In humans, it starts beating on the twenty second day after conception, and soon thereafter it starts to loop. The driving mechanism for this change of shape has not been fully established. The heart tube goes through a sequence of bending and twisting, first going into an “c” loop, then an “s” loop that is “matured,” after which the main architecture of the four chamber heart is discernible [11, 60]. By the eighth week some of the chamber walls are remodeled and the heart takes on the form of the four chamber pump.

This looping has been experimentally modeled using an elastic tube [12]. It was observed, that the tube upon increasing twist deforms in the same way as the heart tube seen in direct images

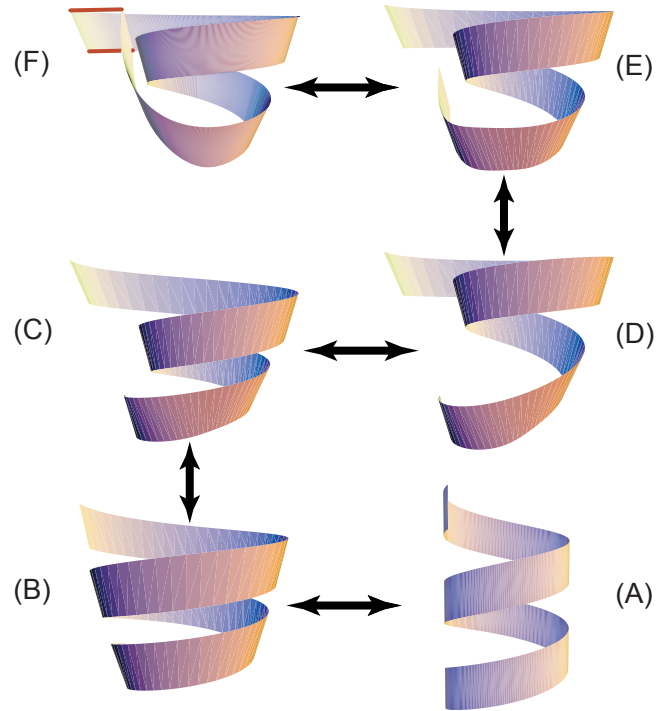


Figure 3.2: A possible set of steps in the development from a spiral tube to a double helix band. (A) A spiral wound around a tube like in an embryonic model. (B) A spiral wound around a tube, that has a varying diameter. (C) The diameter of the tube changes such that the bottom and top loops of the spiral have a larger diameter than the middle loop. (D) The pitch angle of the bottom part of the band is changed to be more vertical. (E) The end of the spiral band is brought up toward the top end. (F) Both ends of the band are at the same level and can be connected to each other; This shape is the same as the double helix proposed by Torrent-Guasp as a heart model.

from chick embryos. Most importantly, the shape of the tube evolves in the same manner as the transformation of ribbon depicted in figure 3.2. However, the mechanical experiment of paper [12] starts at the “c” loop stage and explores the mode of rotation of the looping heart, not the driving forces necessary for such a deformation. Neither do these authors investigate the causes of the twist necessary to induce this transformation. Nevertheless, this experiment strongly suggests that the shape change is governed by elastic mechanical properties of the material rather than a specific genetically encoded biological mechanism.

3.1.1.2 A basic observation

In support of the hypothesis of the dominant role of the mechanics in the heart’s transformation, let us consider a simple tactile experiment. Take a rubber tube, such that your thumbs fit snugly at the ends, insert your fingers into the tube and twist it – you can feel the stress on your fingers. Now, without untwisting, deform the tube to relieve the stress. It is remarkable how similar the resulting shape is to the “c” shape of the developing heart. This type of deformation is a well

known phenomenon in solid mechanics, where the structure bends to relieve stress caused by twist. Additionally, it is common in nature for stresses to play an important role in biological growth and development, for example in the growth of tree branches [61]. From these arguments we hypothesize that the stress from the twist causes the deformation in the embryonic heart. However, in our tactile experiment, we first needed to rotate our fingers to produce any change. So, what happens in the heart tube to induce the twist in the first place? In this light, it is curious that the heart begins to loop almost immediately after it starts beating. This is intriguing, since the contraction of the heart muscle is the only source of the force on the tube, not present before the looping was initiated. Thus we will look for the causes of the twist in the tube’s response to the muscle fiber contractions.

H.R. Crane once wrote on the general problems of biological growth. He pointed out, that while the process in the whole can be too complex for us to produce an equation describing it, we can understand it if we know “the principles involved and something of the order of their importance” [62]. In following his insight, we postulate that for the property of heart function and development the leading order of importance belongs to the bundled helical arrangement of muscle fibers. We follow this road map and utilize modeling tools to approach this question.

3.1.2 Modeling

Biological pumping organs are complicated multi-scale systems, and great efforts are directed at their computational modeling [41–43, 45, 51]. Despite the very significant resources applied and the impressive results achieved, it is currently an insurmountable challenge to computationally represent all the scales and aspects of these systems in their entirety. There exist neither a powerful enough computer, nor a sufficient understanding of the chemistry and control of muscle fibers to model complicated structure encompassing all the scales from the actin filaments up to the organ as a whole. At the same time, there is a great demand especially from the medical community, for models that trade the microscopic details for predictive power [55, 59]. In our opinion, and according to the experience of the engineering field, models should be based on the insight into the biologically dominant features of the system. In such a situation it would benefit us to be able to model the action of muscle without its intricate details. While the popular cardiac models are based on the fact that the fibers inside the heart are helical [20], the notion that they bundle into a single band that is arranged into a double helix [21], has never been properly simulated. It is easy to fathom that such helical structures could be used to optimize the functional properties of the organ, such as for example pumping. We model these macrostructures as applied to a problem of pumping. Meanwhile, knowing that a lot of times band like muscle fiber structures are results of self-assembly, we watch for characteristics that would be responsible for pushing the development of the tubular heart into the double helical arrangement. In that we take advantage of how nature uses these larger scale geometries and intricate dynamics to create wonderfully efficient mechanisms.

Here we present two simple models of biological pumps, for an embryonic fish and adult human hearts. We also consider different possibilities of contracting the muscles that operate these pumps.

3.2 Methods

3.2.1 Geometry of the ribbon models

3.2.1.1 Embryonic tube heart

An embryonic heart is shaped like a tube, which is one of the simplest chambers we can enclose with a band of fibers. The fibers can be arranged circumferentially or longitudinally, or they could form a spiral wound about the tube. Mathematically, such bands can be easily described by a set of parametric equations, which we omit for the sake of brevity [58]. Using these equations we can vary the different parameters of the spiral and tube: pitch (fiber) angle, number of turns, tube radius, tube length, fiber length, cylinder volume, width and thickness of the spiral band. The spirals with varying pitch angles are shown in figure 3.3. However, these parameters are not independent.

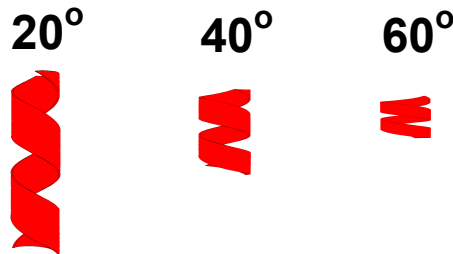


Figure 3.3: Images of the spiral muscle band models for the embryonic heart. The numbers indicate the pitch (fiber) angle: 20° , 40° and 60° are shown. For all three spirals shown here the radius of the tube is constant. The length of the band is also constant, and as a result the length of the tube varies with the pitch angle. The width of the band is taken to be half of the value that would have fully covering the surface of the tube, and as a result the width varies with the pitch angle.

3.2.1.2 Adult heart

A more complicated structure that also involves helical muscle fibers is the human adult heart. There is histological evidence that the fibers are arranged in a spiral band, as shown by Torrent-Guasp, who postulated that the heart muscle is a single band that starts from the pulmonary aorta, hugs the right ventricle, winds down to the apex, as the descending segment, and then spirals up to the aortic valve as the ascending segment. It is, of course, more complicated in terms of mathematical presentation than a simple spiral, but the parametric equations can still be written down using the same mathematical tools [58]. The resulting structure can be seen in figure 3.4A,

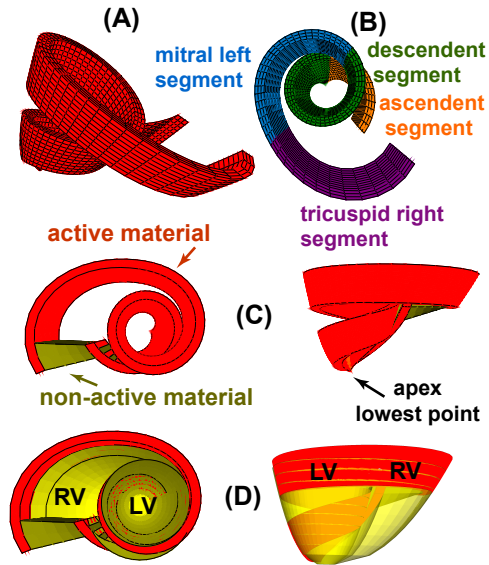


Figure 3.4: Images of the double helical band model of the adult heart. The initial band shape and fitted volume shown from different points of view. (A) The double helical band; (B) the same band color-coded corresponding to physiological segments. (C) The same band in different orientation, with labeled active and non-active material, as well as the apex of the heart. (D) The fitted volumes for left ventricles (LV) and right ventricle (RV) are labeled on these pictures.

with the physiological sections referenced in 3.4B. Figure 3.4D shows how such a relatively simple band structure could be filled out to form a full two ventricle heart.

3.2.2 Choosing the Geometrical Parameters

In both geometrical models, of tube-like embryonic heart and a double helical adult heart, there is a range of parameters that can be varied. We base the choice of parameters on physiological observations, the goals of the simulations, and computational needs.

3.2.2.1 Embryonic tube heart

Number of turns: In order for the spiral wound about a tube to be deformable into a double helix it needs to make two complete rotations. Thus the spiral makes two full turns. In our model we specify it to go around another quarter of a turn, so that the boundaries do not impact the main body of the spiral.

Pitch angle: It is not possible to extract the fiber angle (fiber angle) from the images of the embryonic heart. We therefore wanted the ability to vary the fiber angle. In the experiments the angle is varied between 5° and 80° .

Radius of the tube: In the embryonic heart model the radius of the tube is known, but it is

unclear how far up the tube the spiral fibers extend. Thus, we chose to keep the radius of the tube constant, namely 0.25 cm.

Length of the tube: Once both the number of turns of the spiral and the pitch angle are specified, the length of the tube is mathematically determined.

Fiber length: Once the above parameters are chosen the fiber length is determined.

Band width: The choice of the above parameters also defines the width of the band necessary to cover the whole surface of the tube. We chose for the width of the band to be limited to half of what would cover the tube, to insure that the material did not impinge on itself during twisting.

Band thickness: The thickness of the band is constant and small compared to the width (approximately 1/5 of the width).

3.2.2.2 Adult heart

Number of turns: This parameter is dictated to be two turns by the model design.

Fiber angle: Unlike the pitch angle of the simple spiral, the fiber angle is not constant in the double helical arrangement. We took the information from the histological studies done by Torrent-Guasp. As a result, the math description, although more cumbersome than in the case of the tube, is still known.

Long axis dimension: The long axis dimension is taken to be the same as in the normal adult heart, about 7 cm.

Basal radius: Again the basal radius is taken to be the same as in the adult heart, about 3.5 cm.

Right heart size: The parameter controlling the size of the right heart, was estimated so that the fitted right ventricle volume would correspond to the volume in a normal adult heart (about 130 mL).

Band width: To ease computation the band width is assumed to be a constant. The width is chosen such that the bottom of the mitral left segment does not impinge on the top of the descending segment ($w \approx 2.5$ cm).

Band thickness: The thickness of the band is constant and small compared to the width ($t \approx 0.5$ cm).

3.2.3 Material properties

The properties of the macrostructures of the organ’s muscle are inevitably dictated by the muscles building blocks. The muscle fibers contract along the length of the fiber, thus the muscle band which consists of a group of parallel muscle fibers will contract in the same direction. The fibers cannot contract much over 15% [16], and thus the band will not exceed this maximum shortening ratio at any point along its length. While it is shortening in the fiber direction the band will expand in the other two to conserve volume. The band can shorten as a whole, or parts of it can contract independently of each other. That means that the cells can act separately along the length of the band, the fibers in the width of the band can also contract at different times from each other. For simplicity, we assume a linear elastic response while the material is not excited. The material is incompressible, so the maximal computationally possible Poisson ratio is chosen, $\nu = 0.48$ (an ideal incompressible material has $\nu = 0.5$). The choice of the Young’s modulus will be discussed in section 3.2.5.

As regards to the structure of the adult heart it was necessary to hold it together with a non-active material shown in figure 3.4C. The non-active material was chosen to be four times softer than the active material, i.e., the Young’s modulus of the non-active material is one fourth of the Young’s modulus of the active material.

3.2.4 Boundary conditions

Unlike inside a body, our models are not part of a whole organism. It is, therefore, necessary for us to fix them in space. To do that we need to constrain at least three degrees of freedom, i.e., the x -direction, y -direction, and z -direction.

3.2.4.1 Embryonic tube heart

We found that the most meaningful results are obtained by fixing both ends of the tube. This allows us to consistently look at twisting and pumping in a range of different contraction schemes. If only one end of the tube is fixed, the other flaps about, which makes it hard to determine if there is any twist present.

3.2.4.2 Adult heart

In order to easily compare the dynamics of our model to the heart’s dynamics, we wanted to fix the model in space in the same manner as the heart. In the body, the heart’s apex does not move up or down, while the top of the heart does not rotate. The band structure is fixed in the horizontal plane by the non-active material, in the same manner as the heart is constrained by the vessels.

The lowest point of the double helix is assumed to be the apex, and is constrained in the vertical direction (figure 3.4C).

3.2.5 Excitation schemes

The simplest dynamic scheme is to excite all the cells at the same time and have the whole band contracting in sync. In this case the only periodicity is in time, so we call this a “uniform contraction.”

The other choice is to excite a spatio-temporal wave contraction in the bands. Of course, in creating spatial waves, there are a lot of degrees of freedom. We can change the duration of the contraction, the length of the wave, the origin point of contraction, etc. Here we consider two examples of one dimensional spatial-wave excitation.

To ease the explanation let us label one end of the band α and the other β . A one dimensional contraction wave would then be described as originating from end α of the band and traveling to end β . This means that all the elements in width and thickness, the ones at the same centerline natural coordinate, will contract and relax together.

For ease of comparison to the uniform contraction, where all the elements are contracted in sync, we create a wave that has the contraction front traveling from end α of the band to end β . Once the contraction front reaches the β end of the band, the relaxation front starts from the original α end. This means that there is one instance of time where the whole band is contracted. We call this the “long wave contraction.”

We also run simulations where the wave is shorter and the relaxation front starts before the contraction front reaches the β end. We called such a wave a “medium wave contraction.”

For all the different types of contractions the maximal amplitude of enforced stress was adjusted such that at the given Young’s modulus of the active material, the resulting strain does not exceed physiological constraints discussed in section 3.2.3.

3.2.6 Computational methods

To enable spatio-temporal excitation it is necessary to allow different sections of the bands to contract independently. This creates a complex coupling between local small deformations and huge global shape responses, making it a challenging modeling problem. Another difficulty is that we are considering three dimensional geometries. To combat these problems, we utilize the idea of finite elements. It is possible, with small quadrilateral elements to build very complicated shapes. The finite element method also breaks down a complicated problem of the dynamics of a complicated system in response to deformation into a set of manageable equations. Since this set is very large, it behooves us to use the computing power available to solve it. We therefore, model these bands

using a finite element package, ABAQUS, designed to handle such problems. In the finite element code we use ABAQUS built in tools to independently “excite” each node, and when the nodes of an element are “excited,” the element contracts in the direction of the longitudinal fiber direction.

3.2.7 Data Analysis

Fortran and Matlab codes are used to extract and analyze the data from the simulations. For the purpose of this analysis we extract the position of each node from the simulation. Using this information we calculate the volume. In case of the embryonic one chamber tube model, the volume is approximated as a cylinder. During the deformation the diameter of the cylinder may vary as a function of the long axis. For the double helical, two pumping chamber model of the adult heart, the left ventricle volume is approximated as non-axisymmetric paraboloid. The shape of this paraboloid varies in the course of the beat.

In these simulations we do not model fluid. That means that it is unnecessary for us to model valves. Unless an actual pump has valves, it is very ineffectual. Indeed in the absence of valves most of the blood pumped during a contraction will flow back during relaxation. We thus assume that the valves are present. This assumption implies that if the volume of the chamber is increased, there will be blood sucked into the pump from the inlet. When the volume of the chamber is decreased, the blood is forced out through the outlet. Therefore, we can simply keep track of the volume that would fit inside the spiral to calculate the effectiveness of the pump.

To create a meter stick for our computational experiment we calculate the ejection fraction, for each system as it deforms with time:

$$EF(t) = \frac{V_{\max} - V(t)}{V_{\max}} \quad \text{and} \quad EF_{\max} = \frac{V_{\max} - V_{\min}}{V_{\max}}, \quad (3.1)$$

where, $V(t)$, V_{\max} and V_{\min} are the volume at time t , maximum volume and minimum volume of the chamber, respectively. This is the same formula that is used to find the ejection fraction in physiology for adult hearts, where $V_{\max} = V_{\text{end diastolic}}$ and $V_{\min} = V_{\text{end systolic}}$.

To judge the dynamics of the simulations we use the visualization techniques available in a specialized software – ABAQUS CAE. For the tube model we overlay a wire-frame of the initial configuration on the transformed configuration. This way it is possible to directly compare the original and deformed spiral shape. For the double helix adult heart model, we create a piece of very soft material that is fixed to the side of the simulated left ventricle. To make sure that this indicator does not impact the dynamics, it’s made from a material that is two orders of magnitude softer than the material of the band (i.e., the Young’s modulus of the elastic indicator is one hundredth of the Young’s modulus of the active material). Since the elastic indicator is attached along the length of the left ventricle, it will indicate the amount of twist. If the elastic indicator deforms symmetrically

there is no twist. However, if it deforms sideways, there has to be a twist present.

3.3 Results

We originally hypothesized that the cause of twisting in the embryonic tube heart is the response of the helical structure of the muscle fibers to muscle contractions. To test our hypothesis we created a spiral band wound about a tube. As our first simulation we induced a uniform periodic contraction. This means that at each heart beat the spiral was uniformly contracted and then released.

3.3.1 No twist in a uniformly contracted spiral band

The fiber angle did not have appreciable impact on the dynamics, throughout the range of meaningful values of 5° to 80° . Figure 3.5A shows a series of snapshots of the simulation for a representative fiber angle of 50° . Initially the muscle bands are relaxed (red), then they are gradually contracted, until the elements reach the maximum allowable strain (blue), and then they are relaxed again. The outline of the original configuration is overlaid on each spiral band. The radius of the band at the maximum contraction ($t = 0.4s - 0.6s$) is smaller than the original radius. The snapshots of the simulation show how the spiral smoothly contracts about the central axis and then gradually releases. No perceptible twist is apparent in these images. Thus the forces present are incapable of inducing a twist in the structure. We could have been disappointed by this result, if we did not have an insight from modeling the adult heart.

3.3.2 Back to the future: Adult heart model

To answer this quandary we turn forward, in ontogeny time, to the adult heart. In the adult heart the contraction of the muscle fibers yields an intricate dynamics, the heart twists at each beat [27–29]. If we understand the origin of this twist, we can hope to understand the twist in the embryonic heart. We can draw conclusions about the dynamics of the embryonic heart from our findings on the adult heart, because in both cases any movements are caused by the contraction of the muscle fibers.

In the adult heart the contraction is induced by the Purkinje network. This nerve network does not excite the whole myocardium at once. It is, therefore, unlikely that the myocardium contracts all at once. As a result, the adult heart is subject to spatial-wave contractions instead of a uniform contraction.

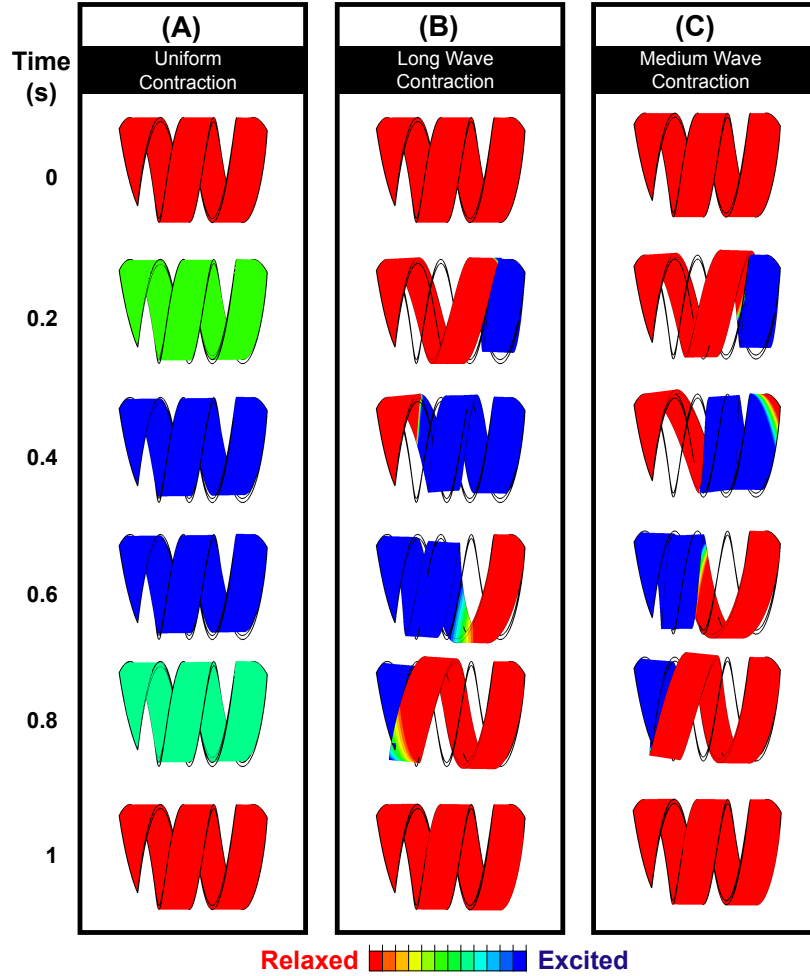


Figure 3.5: Snapshots of the ABAQUS simulations at different time steps for the embryonic heart spiral model with a 50° pitch (fiber) angle. The left column indicates the time in seconds. Each snapshot shows the current configuration of the spiral. The colors indicate the level of excitation as shown in the panel at the bottom, blue-fully excited, red-relaxed. Each simulation starts at the relaxed state ($t = 0s$), goes through the contraction scheme and relaxation scheme, and ends back in the fully relaxed state ($t = 1s$). For comparison purposes, an outline of the initial shape of the spiral is overlaid on each picture as a thick black line. (A) Uniform contraction. Here the spiral smoothly contracts during $t = 0s - 0.4s$, and smoothly relaxes during $t = 0.6s - 1s$. The radius is smallest when the band is fully contracted $t = 0.4s - 0.6s$. There is no change if pitch angle as seen by comparing the current configuration with the outline of the initial shape. Thus, there is not twist in this simulation. (B) Long wave contraction. The contraction wave front starts at the right end ($t = 0.2s, 0.4s$) and travels through the band to the left end. The band is fully contracted at approximately $t = 0.5s$. The relaxation front starts at the left end of the band ($t = 0.6s, 0.8s$) and travels to the other end. The radius is reduced unsymmetrically along the length of the tube ($t = 0.4s - 0.6s$). The pitch angle is changed drastically as seen from comparing the current band to the outline of the initial configuration ($t = 0.2s - 0.8s$). This indicates that there is a twist in the tube. (C) Medium Wave contraction. The contraction wave front starts at the right end ($t = 0.2s, 0.4s$) and travels through the band to the left end. The band is never fully contracted. The relaxation front starts at the left end of the band ($t = 0.6s, 0.8s$) and travels to the other end. The radius is reduced unsymmetrically along the length of the tube ($t = 0.4s - 0.6s$). The pitch angle is changed drastically as seen from comparing the current band to the outline of the initial configuration ($t = 0.2s - 0.8s$). This indicates that there is a twist in the tube.

3.3.2.1 Simulations of the Adult heart

The idea of spatial-wave contractions is rarely considered in cardiac modeling. This is mostly due to the fact that the majority of cardiac models are so complex that it is a challenge to test such cases. For our simplified model we were able to test such spatial-contraction patterns. Figure 3.6 shows time snapshots of simulations with different excitation schemes. In each of the series of pictures the level of excitation is color coded, with red as relaxed, and blue as fully excited. The excitation wave front starts at one end of the band and travels to the other. It is followed by a relaxation front moving in the same direction. We can vary the time between the contraction and relaxation fronts as one of the variables of the system. Thus, one of the possible wave-like contractions will have the whole band fully contracted at some point in time (figure 3.6B). However, it is also possible that the spatial-contraction wave never contracts the band fully (figure 3.6C). One may worry that the wave contraction would negatively impact the pumping ability.

3.3.2.2 How uniform vs. spatial-wave contractions affect pumping ability: Adult heart model

To insure that pumping efficiency was not negatively affected we tested the double helix model of the adult heart under both a uniform contraction and a spatial-wave contraction. The results of these tests were judged by calculating the left ventricular ejection fraction. The use of this particular criteria is justified by the fact that a large amount of physiological data is available for the left ventricular ejection fraction. To calculate the ejection fraction, we approximated the left ventricle as a paraboloid and calculated the volume at each time step. The ejection fraction is then simply given by equation 3.1.

The results for our simplified model easily match the physiological data of maximal ejection fraction. The values in table 3.3.2.2 show no drawback to having a spatial-wave contraction, as compared to a uniform contraction.

		Contraction Type		
	Physiological	Uniform	Medium wave	Long wave
Maximal EF	50%-60%	54%	54%	53%

Table 3.1: The ejection fraction values for double helical pumps under different excitation patterns

3.3.2.3 Different dynamics caused by spatial-waves

What is more fascinating is that the different contraction schemes produce different dynamics of the structure. Figure 3.6 shows the snapshots of the three simulations side by side. The twist is easily visualized by keeping track of the elastic parabolic indicator we fixed at the side of the structure's left

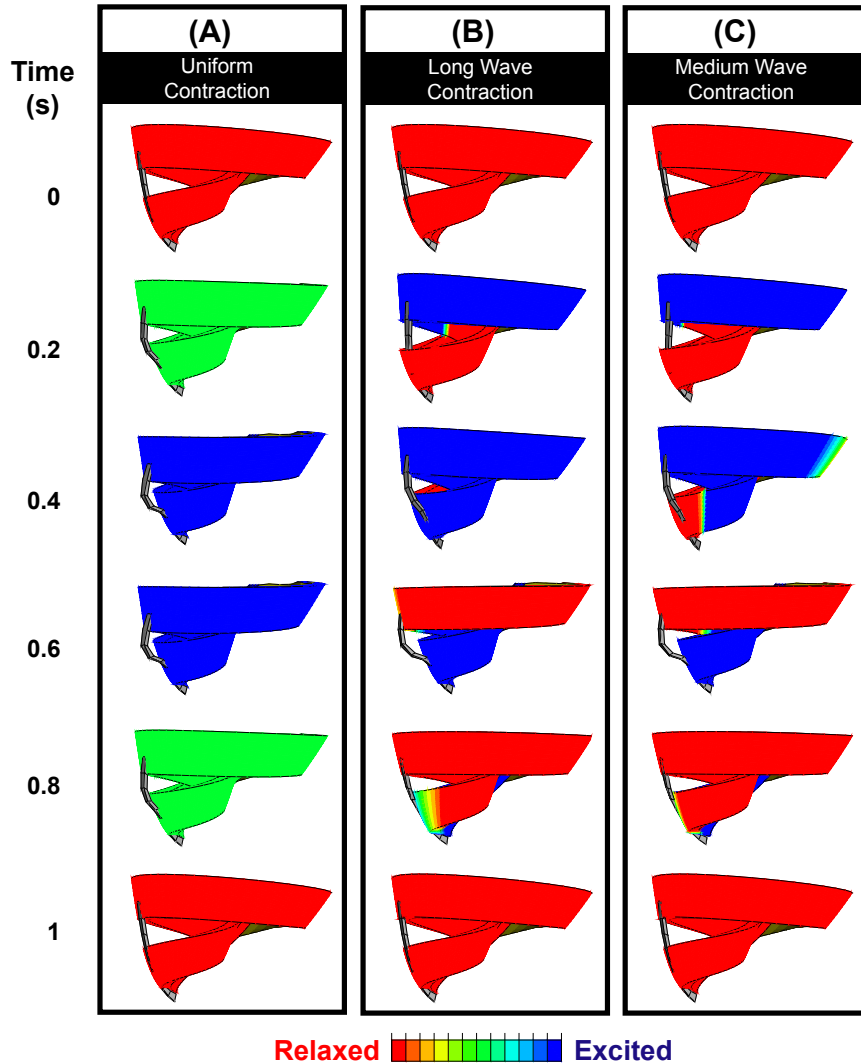


Figure 3.6: Snapshots of the ABAQUS simulations at different time steps for the adult heart double helix model. The left column indicates the time in seconds. Each snapshot shows the current configuration of the double helix. The colors indicate the level of excitation as shown in the panel at the bottom, blue-fully excited, red-relaxed. Each simulation starts at the relaxed state ($t = 0s$), goes through the contraction scheme and relaxation scheme, and ends back in the fully relaxed state ($t = 1s$). From this point of view, the volume reduction can be seen in how the top and bottom parts of the band come together during the contraction. A soft elastic material piece, indicated in dark gray, is fixed to the side of the left ventricle. (A) Uniform contraction. Here the double helix smoothly contracts during $t = 0s - 0.4s$, and smoothly relaxes during $t = 0.6s - 1s$. There is no twist of the left ventricle as indicated by ends of the gray material piece having a symmetric vertical position on the helical band. (B) Long wave contraction. The contraction wave front starts at right heart end ($t = 0.2s, 0.4s$) and travels through the band. The band is fully contracted at approximately $t = 0.5s$. The relaxation front starts at the right ventricle end of the band ($t = 0.6s, 0.8s$) and travels to the other end. The gray elastic material does not deform symmetrically ($t = 0.4s - 0.6s$). This indicates that there is a twist of the left ventricle. (C) Medium Wave contraction. The contraction wave front starts at right heart end ($t = 0.2s, 0.4s$) and travels through the band. The band is never fully contracted. The relaxation front starts at the right ventricle end of the band ($t = 0.6s, 0.8s$) and travels to the other end. The gray elastic material does not deform symmetrically ($t = 0.4s - 0.6s$). This indicates that there is a twist of the left ventricle.

ventricle. The piece of elastic material deforms in a the same radial plane for the uniform excitation scheme (figure 3.6A, $t = 0.2s - 0.8s$). For the both the long and medium wave contraction, at some time step the indicator deforms out of the radial plane (figure 3.6B and 3.6C $t = 0.4s - 0.6s$). This means that the double helical structure twists in cases where the excitation is wave-like and does not in the case of a uniform excitation. This gives us a hint that maybe a wave type excitation in a tubular model could also be related to the twist.

3.3.3 Forward to the Past: Embryonic heart model

We tested a spatial-wave contraction scheme in the spiral wound about a tube. Figures 3.5B and 3.5C show the time snapshots in which the contraction, represented in blue, starts at one end of the spiral and travels to the other end. The relaxation front, in red, follows the same pattern. As in the adult heart, the time between the excitation and relaxation front can be varied. In the uniform contraction scheme the whole spiral is contracted at once, which is not necessarily true for a spatial-wave contraction. The whole structure will be contracted, only if the two fronts are separated from each other by at least the length of the spiral.

3.3.3.1 How uniform vs. spatial-wave contractions affect pumping ability: Embryonic heart model

To insure that the wave-form contraction does not affect pumping we track the volume of the tube during the course of the beat.

Looking at the snapshots of the uniformly contracting tube simulation, one would suspect that the volume should change just as smoothly as the contraction (figure 3.5A). Indeed that is the case as seen in the figure 3.7.

As a matter of principle, it is possible for the spatial-wave contraction to affect pumping beneficially. Indeed, the spatial-wave contraction can induces not only simple shrinking, but also suction. In the plot of a representative fiber angle spiral undergoing a wave contraction the volume increases, then sharply decreases (figure 3.7A). This means that initially more fluid is sucked in and then a larger amount is ejected – larger than would otherwise be possible. The subsequent increase in volume would not produce back flow because of the valves. In the snapshots in the figures 3.5B and 3.5C it is possible to see qualitatively the cause of this suction. In the spatial-wave contraction, the part of the spiral that is contracting pulls on the piece that is still relaxed. In coming to mechanical equilibrium, part of the helix opens up, to reduce the stress on the band. So is this suction effect sufficiently beneficial to offset the fact that the whole band is not contracted at the same time?

For each contraction scheme we compared the maximal ejection fraction at different fiber angles. We use equations 3.1 to calculate the ejection fraction of these pumping tubes. Table 3.3.3.1 shows

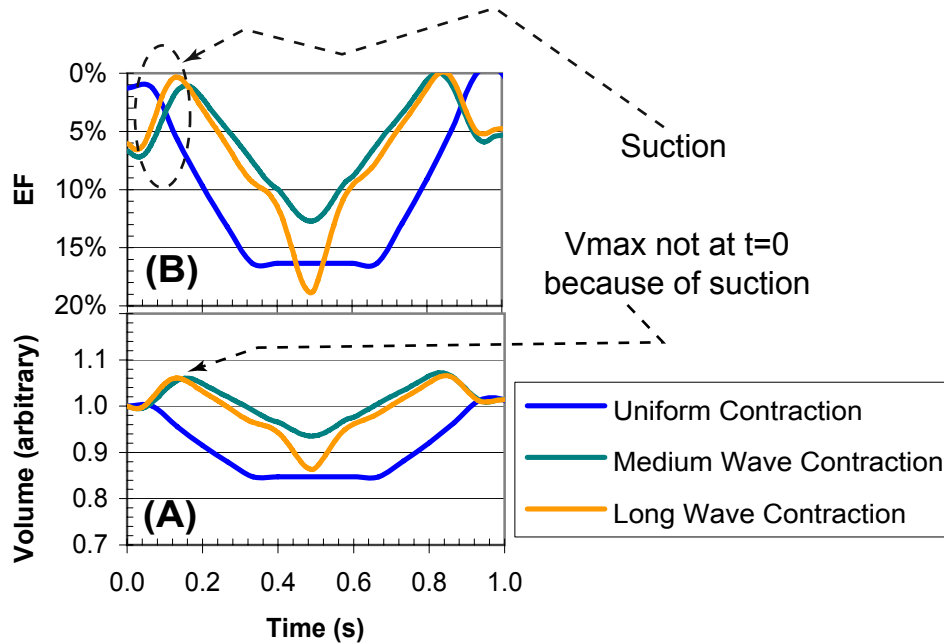


Figure 3.7: (A): Plot of normalized volume of the tube chamber vs. time. In case of wave-type contractions, the volume initially increases ($t = 0.04s - 0.15s$), because of suction. The volume is normalized over the initial value, and as a result the maximum volume in the case of wave contractions is at approximately $t = 0.15s$, as indicated by the arrow. (B): Plot of ejection fraction vs. time. The ejection fraction of the long wave contraction is greater than that of the uniform contraction, because of suction. The period of suction is circled with a dotted line.

the ejection fraction for spirals with different fiber angles undergoing different contraction schemes.

Even a spatial-wave contraction that does not contract the whole spiral is not a significant detriment to the pumping efficiency of the tube. Indeed, at some fiber angles a spatial-contraction scheme is beneficial to the effective pumping. This shows that the spatial-wave does not negatively impact the pumping efficiency. So did it produce twist?

3.3.4 Evidence of twisting in a spiral undergoing a spatial-wave contraction

The snapshots in figure 3.5B and 3.5C qualitatively show that there is an asymmetry in how the spiral deforms. Unlike the deformations in response to a uniform excitation, for both wave excitation patterns the deformed shape is significantly offset from the original outline. Indeed the same mechanism that causes suction produces this radical deformation. In a tube, this deformation would correspond to a twist, to accommodate the change in pitch angle of parts of the spiral.

This begs the question: Maybe the characteristic of leading importance is the wave like contrac-

Pitch Angle	Contraction Type		
	Uniform	Medium Wave	Long Wave
5	24%	18%	18%
10	23%	19%	24%
20	9%	7%	10%
30	11%	7%	9%
40	13%	7%	11%
50	17%	13%	19%
60	21%	21%	29%
70	23%	30%	36%
80	20%	34%	38%

Table 3.2: The ejection fraction values for tubular pumps with different pitch (fiber) angles, under different excitation patterns

tion, and not the helical shape as we originally claimed? If we had induced the propagating wave contraction in a simple tube with either longitudinal fibers or circumferential fibers the forces would have been in the axial or circumferential directions, respectively. As a result, the pumping efficiency would be reduced, since there would be no suction effect. In the longitudinal fiber case the length of the tube would decrease, without opening up any part of the tube. In the radial fiber case, the radius of the tube would simply decrease unsymmetrically, but no twist would occur. Therefore, this model shows that only the combination of the helical structure and the spatial-wave type contraction scheme produces the twist necessary for further development. And this is the main result of this study.

3.4 Conclusions

As Martin Kemp observed in his treatise on “spirals of life” [63], helical designs in living creatures are generally appreciated for their static structure, rather than the active functional benefits they bring. There are many examples in nature where there is a helical muscle structure, ranging from worms to embryonic fish hearts [5, 10, 57]. We have shown here that the helical structure cannot be the sole cause of the mechanical twist necessary for development. If the contraction of the spiral is smooth and symmetrical it cannot lead to twist.

In the adult heart the twisting dynamics are well documented. But, it is also well known that the adult heart is excited in a complicated pattern. By modeling spatio-temporal excitation waves and simple temporal excitation in the adult heart model we show that the twist is only possible if the excitation is in the form of spatial waves. Additionally, we have shown that no negative effects on pumping efficiency are brought about by wave-like contractions.

By applying this knowledge to the embryonic heart we were able to demonstrate twisting of the spiral structure. The spiral tube’s pumping ability is also not impacted by switching from a uniform

excitation to a spatio-temporal excitation.

In light of these results we can form a better understanding of the development history of the heart. In the embryonic tube heart the fibers are organized helically. As it starts to beat the excitation pattern is not uniform, but is instead wave-like. The stress produced by the twisting of the tube under these conditions forces the tube to bend. Thus, begins the road of phylogeny changing the simply spiraled muscle fibers into a double helix structure of the adult heart.

Chapter 4

Modeling the macrostructure of the heart as a dynamic double helical band

4.1 Introduction

Importance of heart modeling hardly needs a justification – it is widely accepted. However, it is less widely recognized how simple and yet profound are some of the questions in the field which remain either completely open or incompletely understood. Here, we will focus on two such questions: First, we consider the ability of the heart to produce large ventricular cavity volume changes with only small local cellular deformations. And second, we look at the principles behind the heart’s intricate dynamical behavior in terms of changing twist of the left ventricle during each heartbeat. Let us comment in more details on these two aspects and their relation to each other.

On the one hand, the active components of the myocardium mass – the myocyte cells – deform by a relatively small amount, with maximum contraction ratio of only 15% [16]. On the other hand, the left ventricular volume exchange ratios, known as ejection fractions, are normally above 55%. Thus, the volume of the internal chamber of the heart decreases by more than half its diastolic value, while each cell contracts by less than a sixth length-wise. Geometrically this would be impossible to achieve without wall thickening effects or helical fibers. In the present chapter, we will concentrate on the latter, because the helical arrangement of the fibers is responsible for the twisting-untwisting of the heart with its beating cycles [55].

In the beating heart, the changes in these two geometrical aspects of cardiac behavior, volume and twist, are intricately coordinated. Indeed, in their ground breaking imaging studies that involved surgically placing markers on the heart Beyar, [29] and Miller [27, 28] were able to provide first accurate measurements of the left ventricle’s twist. Based on these measurements, they hypothesized that the sensitive timing relationship between the twist of the left ventricle and the volume exchange

dynamics is an important aspect of the heart’s volume efficiency. This hypothesis has received further confirmation with investigators taking advantage of the improvements in speckle-tracking imaging [30, 33] and MRI techniques [32], showing that the relationship between ejection fraction and twist changes differently with age and various heart diseases. The characterization of this timing relationship could lead to innovative diagnostic procedures [64]. In the present chapter, we aim to understand and model the well orchestrated correlation between twist and volume exchange.

The nature of the questions which we want to address implies that we should employ a fairly simple model which only captures the very basic features of heart geometry and dynamics. This will allow us to understand to which extent the twist-volume exchange timing is a reliably generic property which could give rise to a diagnostic technique. In general, heart modeling attracted a lot of efforts over the years (see [16] and references therein), and some of the models examined were beautifully simple. One of these models constructed by Sallin [41] explored the need for helical fiber architecture in order to achieve physiological ejection fractions. Another simple left ventricle membrane model, by Needleman et al. [65], explored the difference for normal and infarcted left ventricle in the important pressure volume relationship of the cardiac cycle. An alternative approach, time-varying elastance model, characterized the pumping function of the heart [66]. Sunagawa and Sagawa also gave the most useful summary and comparison of models developed at the time [66].

The most popular current cardiac models simulate the myocardium as a series of shells with differently directed helical fibers [16, 35, 44]. This type of model is based on histological images taken by Streeter in 1969 [20], which show that there is a gradual change in the direction of the fibers with the epicardium and endocardium fibers directed axially, while the fibers in the middle are directed circumferentially. These models have been greatly advanced by the McCulloch group through the development of the constitutive relations for the myocardium materials based on the three dimensional strain measurements [47, 48, 51]. The computational approaches based on finite element models are capable of exploring such issues as optimization of fiber architecture [45], performance of normal and dilated failing hearts when the finite element model included electro-mechanics [53, 54], and a combination of the circulatory system with the ventricular models [52]. Other finite element models explore ischemic left ventricles [67] and arrhythmia [46]. Yet another type of models developed by Peskin et al. uses the immersed boundary method [42, 43]. These current models rarely achieve physiological ejection fractions while observing the limit of 15% fiber contraction. A notable exception is a “one fiber” model developed by Arts et al. [68, 69]. The idea of a “one fiber” model based on the work of both Streeter [20], mentioned previously, and Torrent-Guasp [21], which we describe below. However, none of these modeling works touched upon the important relationship between the twist of the left ventricle and the ejection fraction.

In our approach, we will build our model based on the idea of a single helical band representing the dominant structure in the heart. This idea was originally proposed by Torrent-Guasp [21] alongside

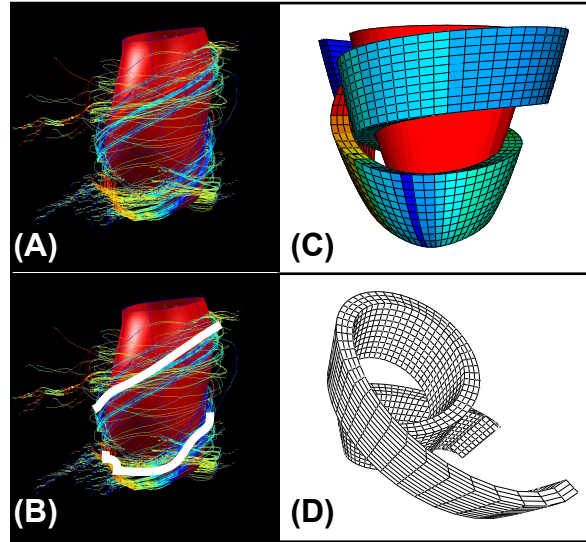


Figure 4.1: (A) Figure of muscle fiber DTMRI provided to us by Helm; (B) The DTMRI image of the muscle fibers overlaid with the major band direction; (C) The simplified band color coded with the direction of the fibers in the same manner as the DTMRI images; (D) The simplified band with no color coding.

Streeter's fundamental work [20]. Torrent-Guasp postulated that the heart muscle fibers form a helical single band that starts from the pulmonary aorta, hugs the right ventricle, winds down to the apex as the descending segment, and then spirals up to the aortic valve as the ascending segment [21]. Recent advancements in MRI technology, specifically the DTMRI technique, enable us to create isolated images of the myocyte fibers, instead of a combination of muscle and collagen fibers [23]. Images obtained using this technology provide further credence to the representation of the heart as a helical band (figure 4.1).

The similarities between the heart myocardium fiber structure and the double helix band give rise to a simplified model, one that allows simulation of more complicated excitation patterns and the dynamic response. It is worth our while to evaluate this simplified model as the dominant structure because it gives us an opportunity to isolate the macrostructure responsible for the behavior of the heart. The excitation patterns are picked so the double helix band model produces the same ejection fraction characteristics as a physiological left ventricle. The full dynamic model is then validated by comparing its twist behavior with the twist of an actual heart over one beat.

4.2 Methods

To give a framework for the structure of the myocardium we assume that the macrostructure of the muscle fibers takes the form of the double helical band described earlier. To simplify the model we assume the band to have a constant width (seen in figure 4.1D). The first necessary step then is to

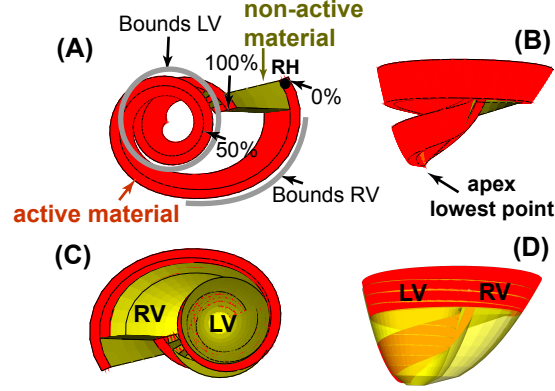


Figure 4.2: Initial shape of the double helical model. The active material is shown in red, the non-active material is shown in dark green, and the fitted chamber surfaces are shown in transparent yellow. (A) The band is shown from the top. The grey lines indicate the portion of the band that bounds the right and left ventricles. The coordinate system used to specify the excitation pattern is specified, with zero at the pulmonary aorta start of right heart (RH), and 100 at the opposite end of the band. (B) The side view of the band, with the apex indicated at the lowest point. (C) Top view with the fitted volumes for left ventricles (LV) and right ventricle (RV) labeled on the pictures. (D) Side view with the ventricles labeled the same way as in (C).

formulate mathematical description of this rather complex three dimensional object. To do that, we first consider an axis line of the band that follows in the direction of fibers through the center of the proposed shape. The next step is to expand the line into a strip with both a width and a thickness. Notice, that with this approach the tangent direction of the centerline is, by construction, the same as the direction of the muscle fibers. The following is the equation of the centerline of such a strip in cylindrical coordinates, where θ ranges from zero to slightly over 4π . Factor 1 is responsible for separating the band at the cross-over point, and Factor 2 regulates the size of the right ventricle. The values of the constants were taken to be such that the resulting shape matched the size of an average human heart: $C_1 = 4.9$ cm, $C_2 = 7$ cm, $A_1 = 1.3$, $A_2 = 0.5$, $C_3 = -0.77$ cm, $C_4 = 1/6$ and $C_5 = 1$.

$$\begin{aligned}
 z_{cent} &= C_1 - C_2 \frac{\theta^{A_1}}{A_2} \exp\left[-\frac{\theta}{B_2}\right], \\
 r_{cent} &= \sqrt{z_{cent} + C_3} \left[1 + C_4 \cos\left(\frac{\theta - \theta_{crossing}}{2}\right) \right] \\
 &\quad \left[1 + C_5 \exp\left(-(\theta - \theta_{right})^2\right) \right] \\
 &= \sqrt{z_{cent} + C_3} [\text{Factor 1}] [\text{Factor 2}].
 \end{aligned} \tag{4.1}$$

Once the centerline of the band is fixed, the band itself can be built about this line:

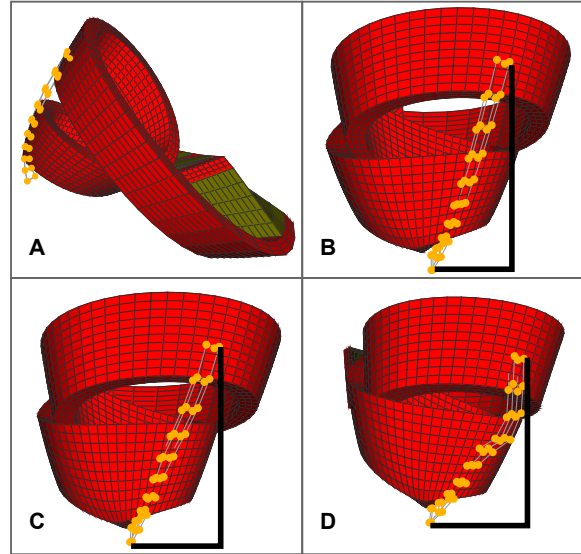


Figure 4.3: The double helical band with the twist markers. The band is indicated in red, the markers are yellow circles connected with grey lines. The thick black lines are drawn for assist visual estimates of out of plane deformation. (A) The relaxed band model with the markers used to calculate twist shown from the side; (B) The relaxed band with the marker shown from the back; (C) The markers shown for a band that has started to contract – notice that there is already an out of plane deformation. (D) The markers shown at end-systole – notice that the elastic material with the markers has buckled in plane as well as twisted out of plane.

$$\begin{aligned}
 z &= z_{cent} + \xi \\
 r &= \sqrt{z_{cent} + C_3} [\text{Factor 1}] [\text{Factor 2}] + \zeta \\
 x &= r \cos \theta \quad y = r \sin \theta,
 \end{aligned} \tag{4.2}$$

where ξ regulates the width of the band and ζ regulates its thickness.

To close the loop, the ends of the band are connected with a non-active material, like collagen, which is not subject to excitation-induced active contraction. A piece of the same material is also used to keep the band together at the cross-over point. The band bounds both the left and right ventricle as shown in figure 4.2A. The volumes were calculated by virtually extending the muscle band to create an enclosed space (figure 4.2C and 4.2D). The left and the right ventricles of the heart were modeled as a paraboloid and a half-paraboloid, respectively.

To calculate the twist, it was necessary to mimic the measuring techniques used in experimental studies where markers are placed along one side of the left ventricle and their positions recorded. In our model, the initial position of the markers was in a vertical plane, on a single parabola on the side of the left ventricle (figure 4.3A and 4.3B). As the band contracted, this parabola was distorted as shown in figure 4.3C and 4.3D.

In a physiological study, the twist is calculated by plotting the degree of rotation at each marker

against their long axial positions and estimating the slope. The computational counterpart of this procedure can be implemented as follows. During the deformation of the band the set of markers can deform in the vertical plane or out of this plane. When the long axis of the left ventricle shortens during contraction the set of indicator markers deform in plane. In the shortening of the long-axis the top and bottom portions of the left ventricle band come closer together, and to accommodate this deformation the strip with the markers buckles outwards. However, unless the top and bottom portions of the band rotate with respect to each other, the buckling will occur in the same vertical plane. Conversely, in twisting of the left ventricle the bottom and top portions of the band move with respect to each other in the horizontal plane. As a result the set of markers deform out of the vertical plane. The greater the twist of the left ventricle, the greater is this out of plane deformation. To calculate the value of the twist, we directly relate it to the out of vertical plane deformation of the set of twist markers. The magnitude of the out-of-plane movement, d , was calculated from knowing the position of the markers, and the twist was then given by:

$$\text{twist} = -\frac{3\sqrt{3}}{2} \frac{d}{(\text{LA})(r_{\text{top point}})}, \quad (4.3)$$

where, LA and $r_{\text{top point}}$ are the long axis length and the radial position of the top point, respectively. This relation between d and twist is easily derived by assuming that a paraboloid shell is twisted such that the rotation angle around z -axis is linearly dependent on z . For ease of visualization the markers are made to be a part of a soft strip of material, a “twist indicator.” The material is three orders of magnitude softer than the material of the band, and thus does not impact the deformation of the band.

For the model examined in the present chapter, we assumed that the double helical band remains in elastic equilibrium at all times. This assumption is motivated by the fact that the forces developed in the muscle fibers are much greater than the resistance of the collagen network and blood pressure. To facilitate the complex task of computing elastic equilibrium in the highly non-trivial geometries of the dynamically evolving fiber shape, we adopt a software package: ABAQUS 6.5 Standard and its nonlinear static analysis. The output was analyzed using the ABAQUS 6.5 CAE in combination with Fortran and Matlab code. The contraction is modeled by providing a material characteristic of an expansion coefficient, so, when fully excited, the element can contract up to 15% in the direction of the fibers. Conservation of volume of the material is enforced by specifying appropriate expansion in the two perpendicular directions in response to the excitation. The excitation coefficient is specified to vary throughout the band with time, allowing for time dependent contraction waves.

To describe the intensity of excitation and its spatio-temporary pattern, we define a unitless quantity, which we simply call Excitation(x, t). We imagine that the fiber, at every point x at time t , contracts proportionally to the value of Excitation(x, t) such that when Excitation equals

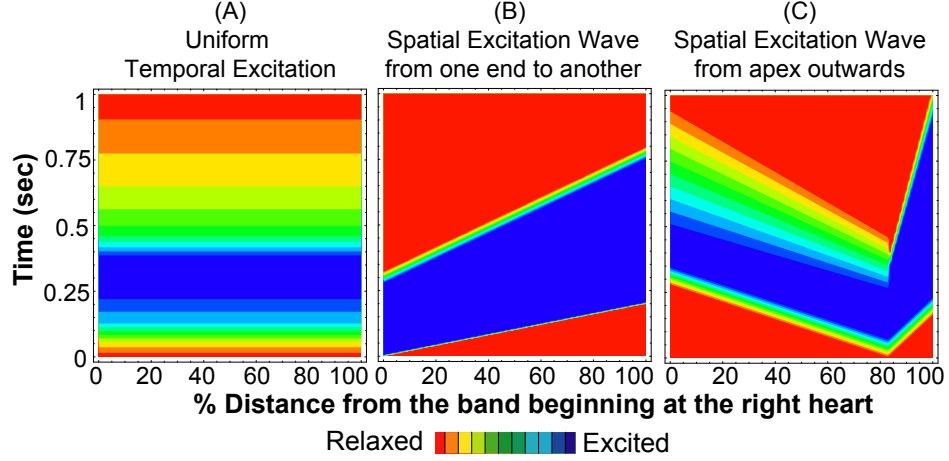


Figure 4.4: The contour plots show the degree of activation for each of the dynamic excitation schemes tried. From left to right it shows, (A) uniform temporal excitation, (B) a spatial excitation wave from one end of the band to the other, and (C) a spatial excitation wave starting at the apex. Below is the legend indicating that the red color represents the relaxed muscle fiber, while blue represents fully excited.

to -1 the element gets fully contracted, by 15% of its length. Therefore, the strain of the element due to excitation is given by $\varepsilon = 0.15 \times [\text{Excitation}(x, t)]$. A series of different excitation waves were simulated, including a step wave (uniform excitation), a time dependent uniform excitation, and traveling waves of various shapes, including a spatial wave that follows the Purkinje excitation pattern [15], which has the contraction wave start at the apex and move outward and upward. For excitation schemes that are not spatial waves, the excitation value was simply specified to match roughly the desired ejection fraction evolution with time (figure 4.4A). A spatial wave excitation scheme is interpolated by the piece-wise linear profile:

$$\text{Excitation}(x, t) = \begin{cases} 0 & \text{at } t < t_1 \\ -(t - t_1)/(t_2 - t_1) & \text{at } t_1 \leq t < t_2 \\ -1 & \text{at } t_2 \leq t < t_3 \\ -(t_4 - t)/(t_4 - t_3) & \text{at } t_3 \leq t < t_4 \\ 0 & \text{at } t \geq t_4 \end{cases} \quad (4.4)$$

where x is the coordinate on the band, starting from the beginning of the band at the right heart's pulmonary aorta (labeled RH in figure 4.2A), and t is time, and t_1, t_2, t_3, t_4 are specific to each contraction scheme. For a simple excitation scheme in which the excitation starts at the pulmonary aorta end of the band, and travels first through the right ventricle, and then through the left one, these are given by:

$$t_i = \frac{U_i}{L_{tot}} x + T_i, \quad (4.5)$$

where $i = 1, 2, 3, 4$, L_{tot} is the total length of the band, and U_i/L_{tot} is the inverse of the speed of the wave front. The parameters are $U_1 = U_2 = 0.2$ s, $U_3 = U_4 = 0.475$ s, $T_1 = 0$ s, $T_2 = 0.005$ s, $T_3 = 0.275$ s, $T_4 = 0.325$ s. For the excitation pattern that starts at the apex and moves outwards the equations become more complex:

$$t_i = \begin{cases} \frac{U_i^R}{AI}(AI - x) + T_i^R & \text{at } 0 \leq x < AI \\ \frac{U_i^L}{L_{tot}-AI}(x - AI) + T_i^L & \text{at } AI \leq x < L_{tot} \end{cases} \quad (4.6)$$

where $AI = 0.85L_{tot}$ is the position of the apex (figure 4.2B), L_{tot} is the total length of the band, and U_i^R/AI and $U_i^L/(L_{tot}-AI)$ are the inverse wave front velocities moving towards the right (pulmonary aorta) and left sides, respectively. The parameter values are: $U_1^R = U_2^R = 0.275$ s, $U_3^R = 0.225$ s, $U_4^R = 1.0$ s, $U_1^L = U_2^L = 0.15$ s, $U_3^L = 0.55$ s, $U_4^L = 0.625$ s, $T_1^R = T_1^L = 0$ s, $T_2^R = T_2^L = 0.075$ s, $T_3^R = 0.25$ s, $T_4^R = 0.475$ s, $T_3^L = 0.325$ s, $T_4^L = 0.375$ s. The contour plots of the excitation pattern for the wave forms used in this chapter are shown in figure 4.4. For this Purkinje type spatial wave the point where the excitation and relaxation fronts start can be moved by changing the value of the constant AI.

4.3 Results and Discussion

4.3.1 Large volume changes – small local deformations

The first step in assessing the validity of the double helical macrostructure model is to track the volume changes in the left ventricle. Figures 4.5A and 4.5B show the band at diastole (initial configuration) and systole (most contracted) for different excitation patterns, respectively. The snapshots demonstrate qualitatively how the volume of the left ventricle is reduced.

To quantify the left ventricular pumping ability, the ejection fraction is calculated. Figure 4.6 shows the plot of the ejection fraction vs. time for three sample excitation schemes along with idealized physiological data. The double helical myocardial model provides physiological ejection fractions of over 55% for any type of excitation wave. It is worth emphasizing that this is achieved without forcing the myofibrils in excess of their physiological contractile ability and without optimization of the temporal excitation scheme and without the wall thickening effect. All three of the excitation schemes considered in this chapter produce physiologically plausible left ventricular volume changes with time.

4.3.2 Twist in the left ventricle

The second step in validating our model is to consider the twisting action of the left ventricle. To aid in estimation of twist we use the “twist indicator” shown in grey in figure 4.5: this is a piece of very

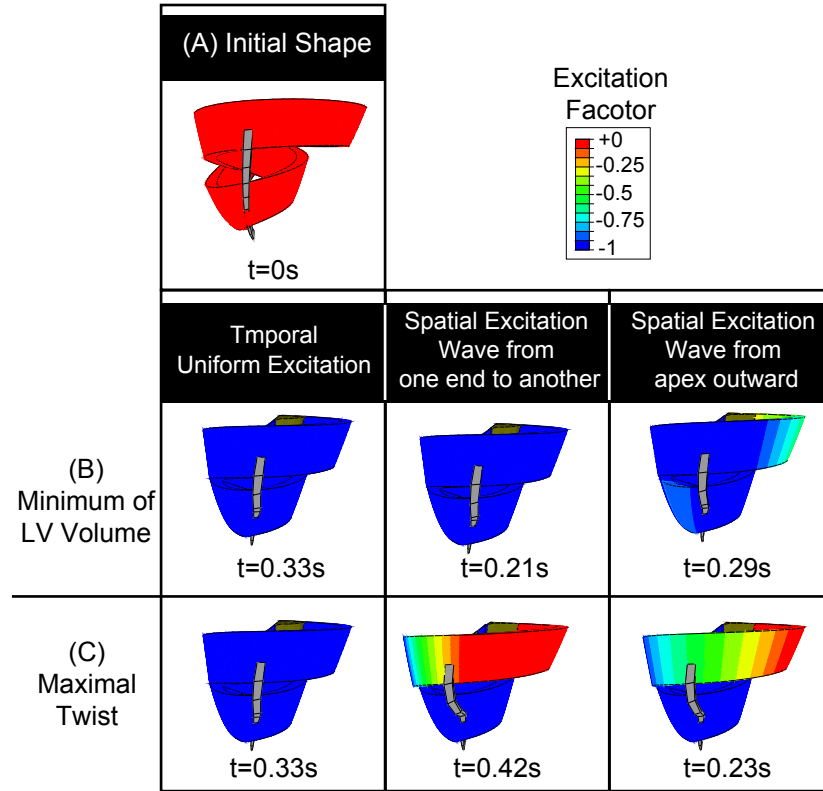


Figure 4.5: Snapshots of the movies for the adult heart model. The legend for the excitation factor is at the top right corner (red-relaxed, blue-contracted). For each type of excitation discussed in this chapter we show the snapshots of the band at the time at which left ventricular (B) volume was at a minimum and (C) the twist was at a maximum. The presence of twist can be qualitatively judged by the out of plane deformation of the grey twist indicator. For the uniform excitation, no out of plane movements can be qualitatively seen. The models subject to the spatial excitation have twist indicator deformations out of plane. To showcase this, we provide another series of snapshots for the spatial wave excitations for times at which the twist was maximal (bottom panels). (A) Initial shape at time, $t = 0s$. (B) Minimum volume: Uniform excitation at $t=0.33s$; Spatial excitation wave from one end of the band to the other at $t=0.21s$; Spatial excitation wave from apex at $t=0.29s$. (C) Maximal twist: Uniform excitation at $t=0.33s$; Spatial excitation wave from one end of the band to the other at $t=0.42s$; Spatial excitation wave from apex at $t=0.23s$.

soft material (100 times softer than collagen) which we computationally attached to the band; it is so soft that it does not affect the band dynamics, but its deformation, driven by the band, can be used to measure twist. Figure 4.5C shows qualitatively that the spatial (traveling) excitation wave causes greater twist than a temporal excitation scheme. Indeed, strongest twist in the cases of the spatial waves is close to physiological with absolute values of over 0.04 rad/cm, while the maximum of the absolute value of the twist in a uniform excitation is only 0.03 rad/cm. However, the main differentiation factor between the different excitation scheme is the timing of the minimum volume of the left ventricle relative to the timing of maximal twist.

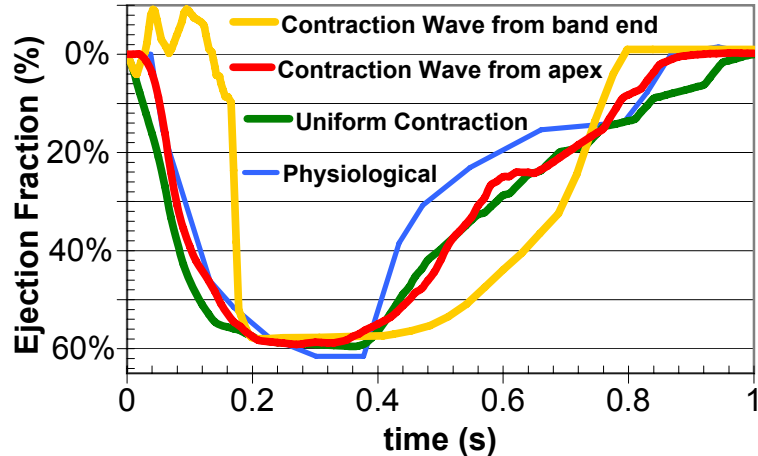


Figure 4.6: Ejection Fraction vs. Time for four cases: green - uniform (entire band contracting at once), time dependent contraction; yellow - a spatial wave contraction starting from the RH end of the band and traveling to the opposite end; red - a traveling Purkinje type spatial wave starting at the apex and moving outward; blue - physiological case adapted from Guyton and Hall [15]. The response to the time dependent contraction is piece-wise linear corresponding to the degree of excitation. The response to the simple (going from one end of the band to the other) spatial wave contraction presents an unphysiological initial increase in volume. The response to the Purkinje type spatial wave does a much better job at matching both the systolic and diastolic physiological behavior than the other spatial wave.

4.3.3 Timing relationship between twist and ejection fraction

We found that all of the trial excitation patterns are able to match the physiological ejection fraction. Additionally, the spatial excitation waves are able to induce physiologically large twist in the ventricle. But how are these correlated? The relationship between these two ventricular properties is important, as Miller [27] and others have observed that it is an important aspect of the volume efficiency. The best way to characterize this timing relationship between the twist of the left ventricle and the volume exchange dynamics is the parametric plot of twist against ejection fraction, parameterized by the time through the beat. We can imagine that a representation point moves on the plane of twist versus ejection fraction as the heart beat develops. In normal heart, this results in a peculiar double-looped shape, as indicated in figure 4.7A. The shape of this parametric representation is very sensitive to the damage in a myocardium [64].

In our simulations we show that only spatio-temporal excitation patterns give rise to a hysteresis-like double-loop relationship. In case of a uniform excitation the ventricle simply twists and untwists uniformly (figure 4.7B). As we follow the looped relationship between twist and ejection fraction for the model activated by a spatial wave starting at the pulmonary aorta and moving to the other end, we notice that we move through the loop in the reverse direction from the normal case (figure 4.7C). This means that instead of taking advantage of the potential energy stored during the contraction

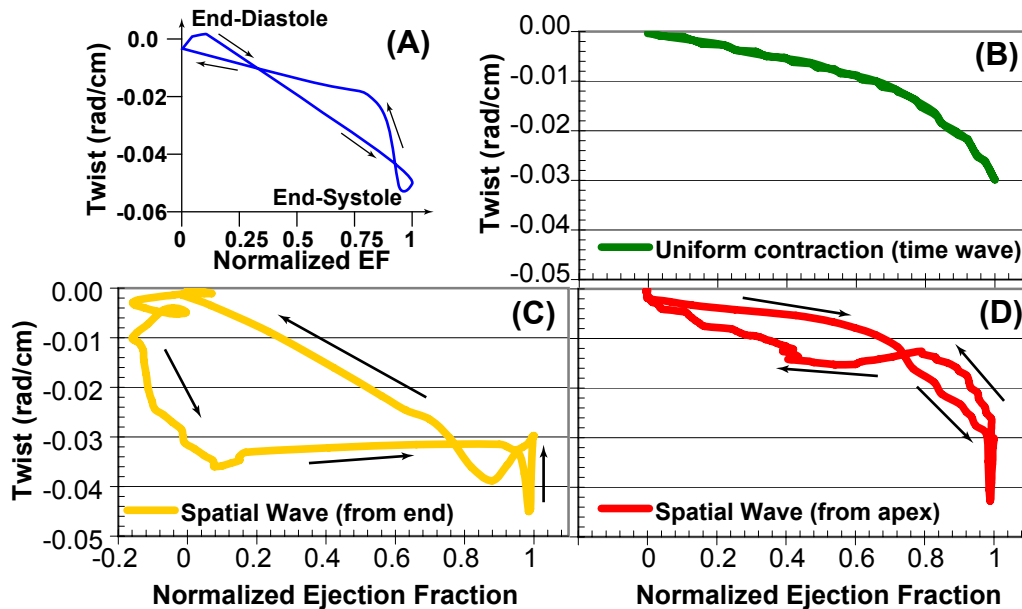


Figure 4.7: Plots of twist vs. normalized ejection fraction. The arrows indicate the progression direction with time. (A) A schematic representation of physiological results adapted from a paper by Moon et al. [27]. (B) Model results for uniform time dependent contraction. The ventricle simply twists and untwists along the same path. (C) Model results for simple spatial wave (traveling from one end to the other). While this presents a looped behavior, the arrows are in reverse of physiologically observed, which means the ventricle is working against the twist instead of utilizing it during the filling stages. (D) Model results for the Purkinje type wave. The relationship between twist and ejection fraction in this case is a physiological type double loop with the correct directions and the magnitude of the twist also matches experimental observations.

stage in the deformed material, the heart needs to perform extra work to overcome the twisting. Importantly, we conclude that the traveling contraction wave mimicking the Purkinje activation system is the one to reproduce the intricate relationship between twist and ejection fraction (figure 4.7D).

4.3.4 Varying the point of the initiation of spatial excitation waves

So far we have presented in detail the effect of two different spatial excitation waves: in one of them, the excitation wave starts at the pulmonary end of the band and travels to the other end; in another, the excitation starts in the middle of the band at the lowest point - the apex. It is possible, by varying the value of parameter AI , to create excitation schemes that lie in between of these two extremes, where the excitation starts neither at the end of the band nor at the apex. Additionally, by adjusting the speed of the excitation and relaxation wave fronts (adjusting constants U_i) the left ventricular volume changes can be made to closely match physiological. However, the relationship

between twist and ejection fraction is very sensitive to the location of the initial wave fronts. Indeed, if the wave fronts do not initiate in the inner loop, i.e., the septum and apex region, it does not seem to be possible to reproduce the double looped hysteresis. Therefore, we conclude that unless the excitation is initiated in the septum close to the apex, the refilling of the ventricle will not be efficient.

It is also possible to create excitation patterns that would move through the layers of the band, rather than only longitudinally along the band. This would provide a fine tune control of the timing of the twisting of the ventricle. Indeed, if the location of the initiation of excitation impacts each region of hysteresis loop, an ability of the signal to propagate through the layers could provide for control of the different parts of the loop. However, it is worth it to note here, that to an imaging technique incapable of resolving the muscle fibers from the myocardium wall the excitation wave that are modeled here would appear to move through the layers of the wall from the inner wall toward the outer.

4.4 Conclusion

By avoiding the complexity of modeling the whole heart structure at once, including all of the collagen and blood, we show that the double helical simple band structure is akin to an engine behind the heart pumping action. Indeed, by coupling this band-like structure of the myocardium with a Purkinje-type contraction scheme, we were able to achieve both the physiological ejection fraction of 60% and the important twisting pattern, without exceeding the contractile ability of the myofibrils. It is also possible to use this simple model to show the reduction in pumping efficiency when the main fiber orientation at the apex becomes more oblique, as happens after an infarction if the heart dilates in DCM. The model can also be used to model infarctions of different parts of the myocardium. Our results illustrate the dominance of the single-band structure, which can now be used to develop a new generation of heart models.

Chapter 5

Modeling the macrostructure of the heart: healthy and diseased

5.1 Introduction

One of the common heart diseases is dilated cardiomyopathy (DCM). Dilated cardiomyopathy is associated with a number of pathological signs. The outward symptoms presented by patients with this disease are caused by the reduction in heart function, i.e., a reduced maximal left ventricular ejection fraction. Structurally there is a whole series of events called left ventricular remodeling, the most glaring of which is that the chamber dilates (loosing its normal ellipticity and becoming more spherical in shape), and the walls become thinner. However, it is presently unclear what else is involved in the remodeling, and in general the fact that chamber dilation is easily observed does not imply that this is the most important factor in the reduced functionality of the heart. Particularly, there is no consensus on the significance of myofiber orientation changes: some groups consider it essential [17, 56], while others claim that the only important factor is the change of the ventricle shape [25]. In this chapter we strive to gain some insight into the dominant cause of the functional reduction – whether it is a result of the anatomical shape change or the change in the fiber angle.

Such an insight has a potential to guide the ventricular surgical restorations, such as the DOR procedures, which are commonly used to treat patients with left ventricular remodeling pathologies [70]. Indeed, papers [25, 59, 71] discuss whether the ventricular surgical restoration should aim to primarily address the change in myofiber orientation or to focus on fixing the shape of the ventricle chamber. Of course, the choice between these two strategies depends on how much relative weight is given to the change in chamber shape as opposed to the change in fiber orientation.

It is unsurprising that this issue is difficult to resolve clinically, since it is hard to judge which factor is important – the changes to the shape of the chamber and the orientation of the fibers happen more or less simultaneously. To untangle this conundrum we use computational modeling, which allows us to look at the effects of chamber shape change and fiber orientation change separately.

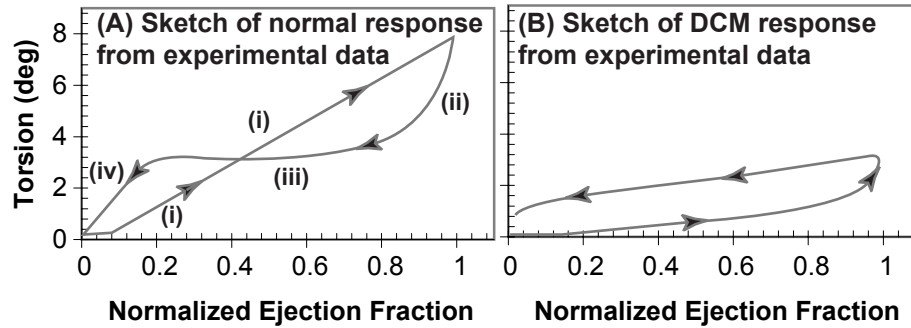


Figure 5.1: Sketches of plots of torsion vs. normalized ejection fraction. The arrows indicate the progression through the loops with time. (A) A schematic sketch showing the physiological torsion for a normal heart adapted from works by Tibayan et al. and Nakai et al. [72, 73]. (i) Systole. (ii) Early diastole - rapid inflow. (iii) Diastasis. (iv) Late diastole or atrial systole. (B) A schematic sketch for a heart with DCM adapted from [73];

To resolve by modeling whether or not the shape change is the leading cause of the reduced maximal ejection fraction we need a diagnostic tool that is independent from visual observations of structural changes. The reduction in ejection fraction alone cannot serve as such an indicator, as it is also reduced in other types of heart disease. Instead, we turn to the observation of the twisting motion of the left ventricle. It has long been observed that the left ventricle rotation changes significantly if the heart is damaged or is being stressed [31, 32, 56]. It was found that the relationship between the twist of the left ventricle and the ejection fraction is very sensitive to damage of heart and in the future might be used as a diagnostic tool [27–29]. During a beat of a healthy heart, the volume of the left ventricle is reduced as it is twisted, after end systole, but before filling starts, the heart untwists isovolumetrically, i.e., without a change in the left ventricular volume. This is best visualized in a parametric plot of the twist vs. the ejection fraction as both of these variables develop in time. In such a plot a healthy response has a characteristic shape with two loops, a schematic of which is shown in figure 5.1A. Some researches associate dilated cardiomyopathy with an initial negative twist [56], however such a characteristic is sometimes found in healthy patients as well [72]. It has been found that in dilated cardiomyopathy, unlike other pathologies, there is only one counterclockwise loop in this relationship [73] (figure 5.1B shows a sketch of this relationship). In other words, the ventricle does not twist as much initially as the healthy heart, and there is no isovolumetric (isochoric) untwisting. We use this characteristic to judge whether the model represents a heart with dilated cardiomyopathy.

The models used in this dissertation are based on the histological and DTMRI evidence that the myocardium can be approximated as a double helical muscle band (as seen in figure 5.2) [21, 23]. A detailed discussion of different characteristics of this model is published elsewhere. In this chapter, our objective is to test whether the change of the shape of the left ventricle or of the fiber orientation is responsible for presenting the dilated cardiomyopathy symptoms. The plan for this chapter is as

follows: After presenting all relevant methodical issues in section 5.2, we describe simulation results in section 5.3. We discuss the finding in section 5.4, starting with the general qualitative description of the importance of the double-loop relationship between twist and ejection fraction. We formulate the main conclusion in section 5.4.3.

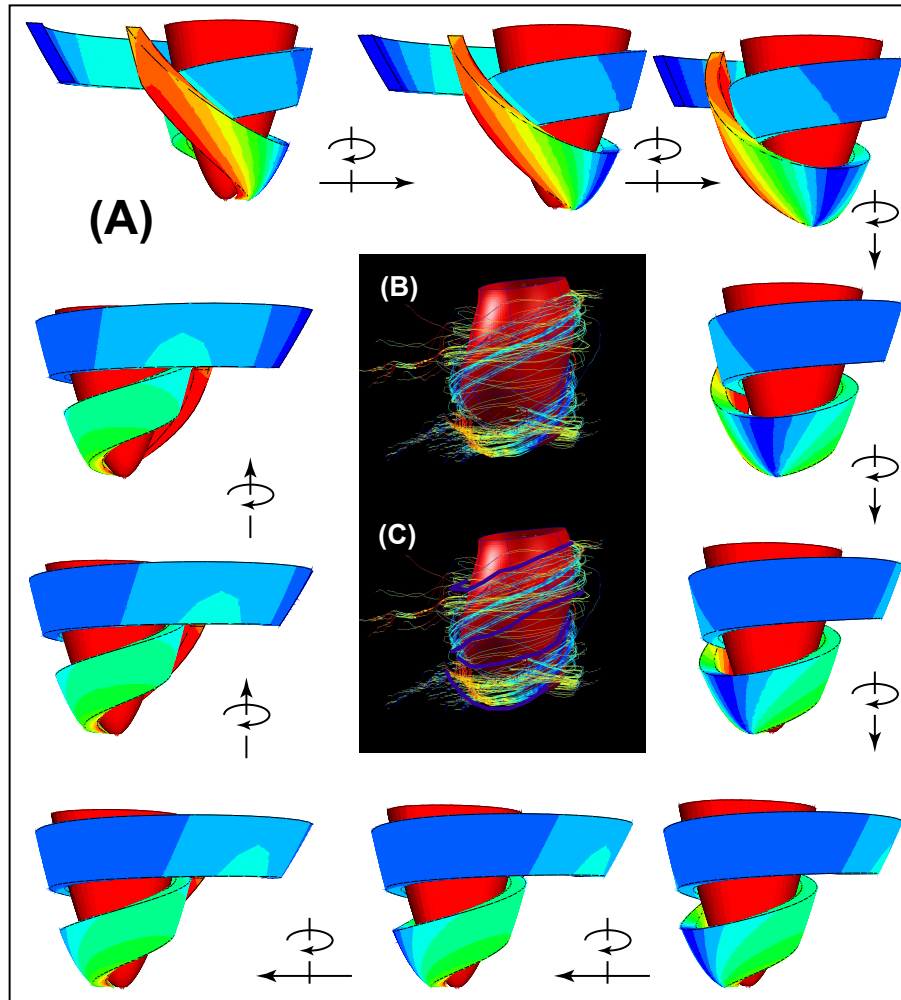


Figure 5.2: (A) The model double helical band is color coded for the fiber angle – blue and red representing circumferential and axial fibers, respectively. The fiber angle was calculated in the same way as in paper by Helm et al. [23]. The red chamber is the left ventricle. The series of snapshots around the perimeter show the model from different view points. (B) DTMRI of the muscle fibers in the myocardium color coded for fiber angle – blue and red representing circumferential and axial fibers, respectively. The red chamber is the left ventricle. The image was given to us by Helm. (C) The DTMRI image with the band outlined in dark blue.

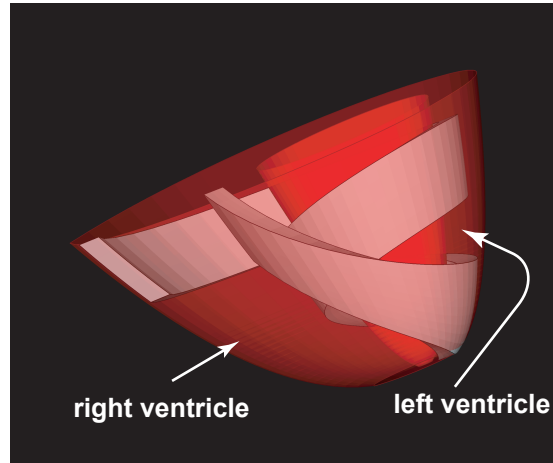


Figure 5.3: The band (grey) inside the heart shell (transparent red) with the left and right ventricles indicated.

5.2 Methods

5.2.1 Geometries of the bands

In order to determine the relative importance of different types of damages in dilated cardiomyopathy we chose a model that approximates the myocardium as a double helical band. Such view of the arrangement of cardiac muscle fibers is supported by both histological and DTMRI data [24]. In this approximation the muscle band starts from the pulmonary aorta, hugs the right ventricle, winds down to the apex, as the descending segment, and then spirals up to the aortic valve as the ascending segment. The exact path of the band in space is dictated by the fiber angle and the shape of the chambers bounded by the band (i.e., the right and left ventricle). The double helical band inside the shell of the myocardium can be found in figure 5.3.

A healthy heart has an elongated shape, that looks like an American football. As a result, the heart is often times modeled as an elongated half-ellipsoid. However, since in this chapter we focus on the function of the left ventricle, we found it more convenient to approximate the shape with a paraboloid. In case of dilated cardiomyopathy the heart is expanded to the point where it looks more spherical than ellipsoidal (i.e., more like a soccer ball than a football). The other change attributed to dilated cardiomyopathy is the change in fiber angle. To test the hypothesis that the change in fiber orientation is the primary factor responsible for the specific characteristics of dilated cardiomyopathy we examine four separate types of models: A model for a healthy heart; models with varying reduction in fiber angle in the region of the apex; models with a dilated left ventricular chamber; a model with other damage introduced to the band.

The normal shape of the left ventricle can be approximated with a paraboloid, with a long axis of 7 cm and the basal radius of 3.5 cm. The normal fiber orientation was taken from histological

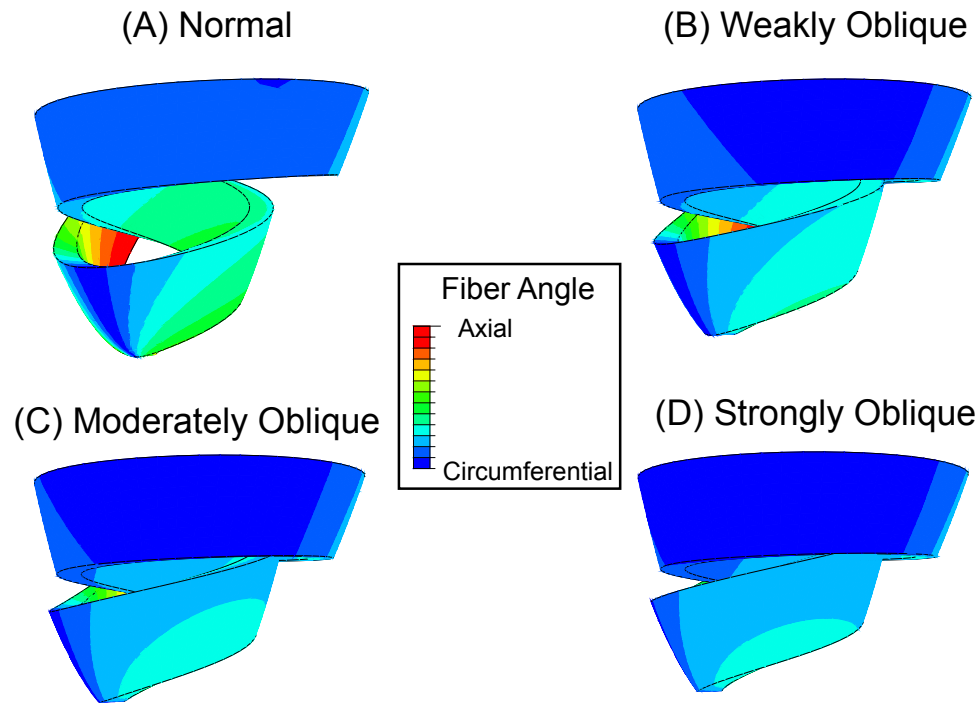


Figure 5.4: The model double helical band is color coded for the fiber angle – blue and red representing circumferential and axial fibers, respectively. The fiber angle was calculated in the same way as in paper by Helm et.al. [23]. (A) “Normal” model with fiber orientation corresponding to physiological. (B) “Weakly Oblique” model showing the fibers close to the apex to be a little more oblique than in the “Normal” case. (C) “Moderately Oblique” model with fibers considerably more oblique in the apical region than would be normal. (D) “Strongly Oblique” model showing the fibers close to the apex region to be almost circumferential. (A different view of these can be found in figure D.3)

data [21]. For ease of comparison we calculated and plotted (figure 5.4) the fiber angle the same way it is calculated from MRI data [23]. The following lists the different models that we describe in this chapter, along with the shorthand names that will be used to refer to these models in the rest of the chapter.

Normal: A case with the normal elongated shape and normally oriented fibers. The band color coded for the fiber angle can be found in Figure 5.4A. The fitted left ventricular volume can be seen in Figure 5.5A. The ratio of the long axis to the basal radius is taken to be around $7cm/3.5cm = 2$.

Weakly Oblique: A case with the normal elongated shape of the left ventricle, but with fibers in the region of the apex made slightly more obliquely oriented than normal. Figure 5.4B shows this band color coded for the fiber angle, and the region closer to the apex has fewer green tones than in the normal case meaning that the fibers here are more oblique than in the normal fiber orientation.

Moderately Oblique: A case with the normal elongated shape of the left ventricle, but with fibers in the region of the apex made more obliquely oriented than normal. Figure 5.4C shows this band color coded for the fiber angle, and the region closer to the apex has more blue coloring than in the “Weakly Oblique” case meaning that the fibers here are even more oblique.

Strongly Oblique: A case with the normal elongated shape of the left ventricle, but with fibers in the region of the apex made very much more obliquely oriented than normal. Figure 5.4D shows this band color coded for the fiber angle, and the region closer to the apex is mainly blue meaning that the fibers here are even more oblique than in the “Moderately Oblique” case.

Moderately Dilated: A case with the heart slightly dilated – meaning that ratio between the long axis and the basal radius was made to be ≈ 1.2 , but we still approximate the volume as a paraboloid as shown in figure 5.5B. The fibers in this model are oriented normally.

Strongly Dilated: A case with the heart very dilated – the geometry of the left ventricular chamber was approximated with a section of a sphere as shown in figure Figure 5.5C, as a result the ratio of long axis to the basal radius is ≈ 1 . The fibers in this model are oriented normally.

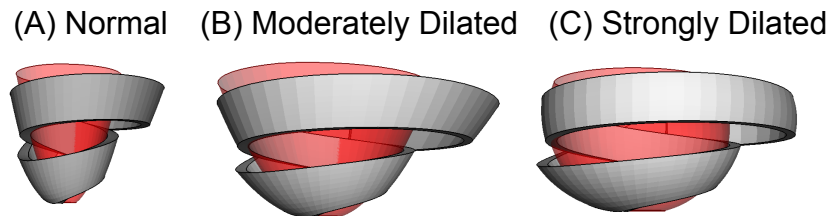


Figure 5.5: The model double helical band (grey) with the fitted left ventricular (LV) volume (red). The long axis dimension in each case is 7 cm. (A) “Normal” model, the LV is approximated with a paraboloid, with the basal radius of ≈ 3.5 cm; (B) “Moderately Dilated” model, the LV is approximated with a paraboloid, with the basal radius of ≈ 6 cm; (C) “Strongly Dilated” model, the LV is approximated with a section of a sphere, with the basal radius of ≈ 7 cm. See different view in figure D.4

Other Damage: A case with normal fiber orientation and a normal shape of the left ventricle, but an outer layer of the band in the region of the apex is made inactive to stimulate other damage that might occur in case of infarction, where part of the myocardium is dead. Figure 5.6 shows the materials used in the “Normal” model and in this model, with the dead material color coded in grey. An additional figure D.6 can be found in the appendix D.

The detailed description of the equations for these bands, along with geometrical constants used in this chapter can be found in appendix C.1.

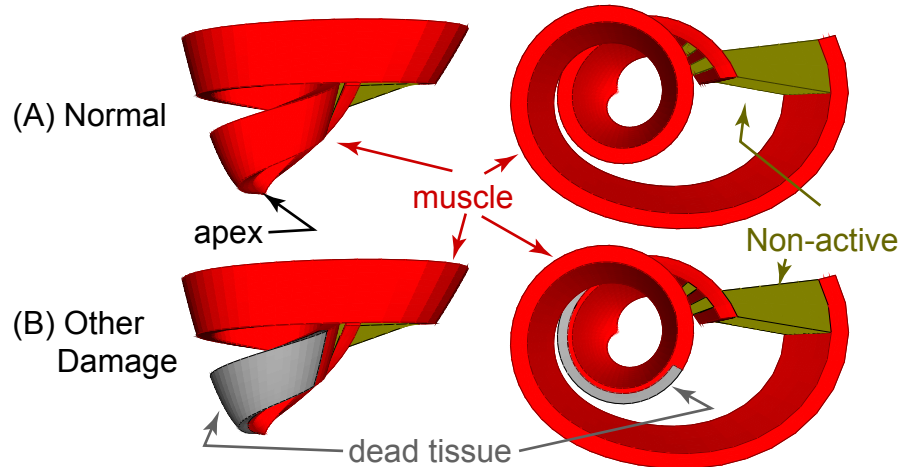


Figure 5.6: The double helical band model color coded for different types of materials used in these simulations: red - muscle, active material; green - non-active, softer, collagen type material; grey - dead tissue with a non-active stiffer material. (A) “Normal” model with no dead tissue from the side view (left) and top view (right). The left panel also shows the location of the apex used to hold the band in the vertical direction. In the horizontal plane the band is constrained by the non-active material. (B) “Other Damage” model showing the dead region near the apex.

5.2.2 Material Properties

The muscle band, which consists of a group of parallel muscle fibers contracts along the direction of the fibers, as each muscle fibers can only contract longitudinally. The fibers cannot contract much over 15% [16], therefore we impose a condition that the band will not exceed this maximum shortening ratio at any point along its length. While it is shortening in the fiber direction the band expands in the other two directions to conserve volume of the material. The whole band can shorten simultaneously, or parts of it can contract independently of each other. That means the muscle cells in different regions of the band can act separately. For simplicity, we assume a linear elastic response as long as the material is not excited. This approximation is appropriate for these simulations because we are not modeling the blood, and therefore we are not considering the pressure forces on the material. The material is incompressible, which ideally would mean that it has the Poisson ratio of $\nu = 0.5$, so we choose the maximal computationally possible Poisson ratio of $\nu = 0.48$. As we do not consider pressure inside the left ventricle, we choose to normalize modulus of each type of material used in these models by the Young’s modulus of the muscle.

The double helical band is held together with a non-active material shown in figure 5.6A. The non-active material was chosen to be four times softer then the active material, i.e., the Young’s modulus of the non-active material is one fourth of the Young’s modulus of the active material.

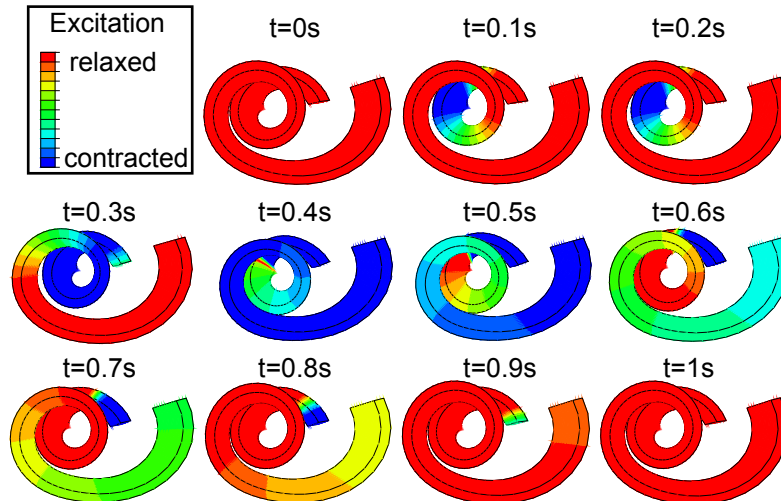


Figure 5.7: Top view of the double helical band model color coded for excitation: red and blue correspond to relaxed and excited, respectively. The material is fully contracted (up to 15% shortening) when it is fully excited (blue). The excitation wave starts at the apex and propagates outward. The band is completely contracted (end-systole) at $t = 0.38s$. During diastole the relaxation wave front also starts from the apex and travels outward. (See different view in figure D.5.)

5.2.3 Boundary Conditions and Excitation

In order to easily compare the twist in our model to the heart's twist, we wanted to fix the band in space in the same manner as the heart. In the body, the heart's apex does not move up or down, while the base of the heart does not rotate. The band structure is fixed in the horizontal plane by the non-active material, in the same manner as the heart is constrained by the vessels. The lowest point of the double helix is assumed to be the apex, and is constrained in the vertical direction (figure 5.6A).

The excitation scheme was chosen to mimic the Purkinje network that has the excitation start close to the apex and progress outward [15, 56]. Figure 5.7 shows snapshots of the model band at different times during the heartbeat color coded for excitation. For all the different types of contractions the maximal amplitude of enforced stress was adjusted such that at the given Young's modulus of the active material, the resulting strain does not exceed physiological constraints discussed in section 5.2.2.

5.2.4 Computational Methods

To enable spatio-temporal excitation, it is necessary to allow different sections of the bands to contract independently. This creates a complex coupling between local small deformations and huge global shape responses, making it a challenging, but also promising, modeling problem. Another difficulty is that we are considering three dimensional geometries. To combat these problems, we

utilize the idea of finite elements. It is possible, with small quadrilateral elements to build very complicated shapes. The finite element method also breaks down a complex problem of the dynamics of a large system in response to deformation into a set of manageable equations. Since this set is very large, it behooves us to use the computing power available to solve it. We therefore, model these bands using a finite element package, ABAQUS, designed to handle such problems [74]. In the finite element code we use ABAQUS built-in tools to independently “excite” each node, and when the nodes of an element are “excited,” the element contracts in the direction of the longitudinal fiber direction.

To model the complicated geometry along with this spatial wave activation we assume elastic equilibrium and utilize the final element package ABAQUS Standard 6.5. We use non-linear analysis with orthotropic elastic material properties.

5.2.5 Data Analysis

The results of the simulations are visualized and analyzed using both ABAQUS CAE 6.5 visualization software, and a code of Fortran and MatLab. The functionality of the left ventricle was judged by calculating the left ventricular volume as a function of time, maximal ejection fraction, torsion (or twist) as a function of time, and the peak rate of filling.

5.2.5.1 Volume and Ejection fraction

The volume of the left ventricle was approximated as the sum of slices of paraboloid for all cases except for “Strongly Dilated,” where it was approximated with spherical slices. The ventricle chamber was cut into slices by vertical planes (constant θ) containing the long axis between θ and $\theta + \Delta\theta$, where $\Delta\theta \approx 7.2^\circ$. The calculated volume was normalized over the end diastolic volume (EDV).

The pumping efficiency of the band is measured by calculating the ejection fraction:

$$EF(t) = \frac{V_{end\ diastole} - V(t)}{V_{end\ diastole}}, \quad (5.1)$$

$$EF_{max} = \frac{V_{end\ diastole} - V_{end\ systole}}{V_{end\ diastole}}, \quad (5.2)$$

where, $V(t)$, $V_{end\ diastole}$ and $V_{end\ systole}$ are the volume at time t , end diastolic volume and end systolic volume of the chamber, respectively.

5.2.5.2 Rate of Filling

The peak rate of filling was estimated as the highest slope during early diastole. The period of early diastole was determined to start at the time of the minimum volume (end-systole). Early diastole ends at the start of the diastasis period, where the speed of filling falls sharply.

5.2.5.3 Twist and Torsion

Often times the words twist and torsion are used interchangeably, which makes sense since they measure the same effect. Twist is normally defined as the slope of the linear approximation of the relationship between the angular rotation of the markers and their long axial position [27–29]. Torsion is defined as the average angular rotation of the markers placed at different points along the long axis [73]. However, in some cases the later definition is named twist [72]. While the two values (slope and average) are easily related, one cannot be calculated from the other without additional measurements that are not normally provided in these papers. To be consistent for this chapter we define twist as the slope and torsion as the average of the rotation at different long axis positions. The detailed description of the method used to calculate these quantities can be found in appendix C.2. For this chapter all of the results shown will be of torsion.

5.3 Results

5.3.1 Ejection fraction

For each of the models tested here (Normal, Oblique Fibers, and Dilated Shapes), we calculated the volume of the left ventricle as a function of time. Figure 5.8 shows the change of volume, as percentage of end-diastolic volume, with time for each of the models. The normal case, shown in green, has a physiological response – with a systolic contraction leading to a large stroke volume, i.e., small end-systolic volume, followed by rapid filling, and then a slower filling of the left ventricle. In the cases where the myocardium band is malformed in any way the stroke volume is reduced. The plots show that the more severe the damage introduced into the model the greater the impact on the end-systolic volume. To quantify this we calculated the maximal ejection fraction for each case, the results of the calculations can be found in Table 5.1. The normal model shows a physiological maximal ejection fraction of over 55%. Any kind of introduced damage, be it a change in geometrical shape, a change in fiber angle, or a simulated infarction, reduces maximal ejection fraction. In the cases of progressively more oblique fibers the ejection fraction drops from 46% to 37% as the fiber

Model Type	Maximum EF	Maximal Torsion	Peak Rate of Filling
Normal	58%	8.4°	1.32 (EDV/sec)
Weakly Oblique	46%	7.1°	1.14 (EDV/sec)
Moderately Oblique	40%	6.5°	0.98 (EDV/sec)
Strongly Oblique	37%	5.7°	0.77 (EDV/sec)
Moderately Dilated	46%	4.5°	1.26 (EDV/sec)
Strongly Dilated	33%	2.5°	1.31 (EDV/sec)
Other Damage	52%	4.9°	0.97 (EDV/sec)

Table 5.1: Results for different model types

angle in the apical region is decreased (brown, red, and yellow in the plots of figure 5.8). In the case of a changed overall geometry of the chamber the ejection fraction also decreases from 46% for “Moderately Dilated” shape to 33% in the “Strongly Dilated” model (blue and light blue in the plots of figure 5.8). The “Other Damage” model has the ejection fraction of 52% (grey in the plot of figure 5.8).

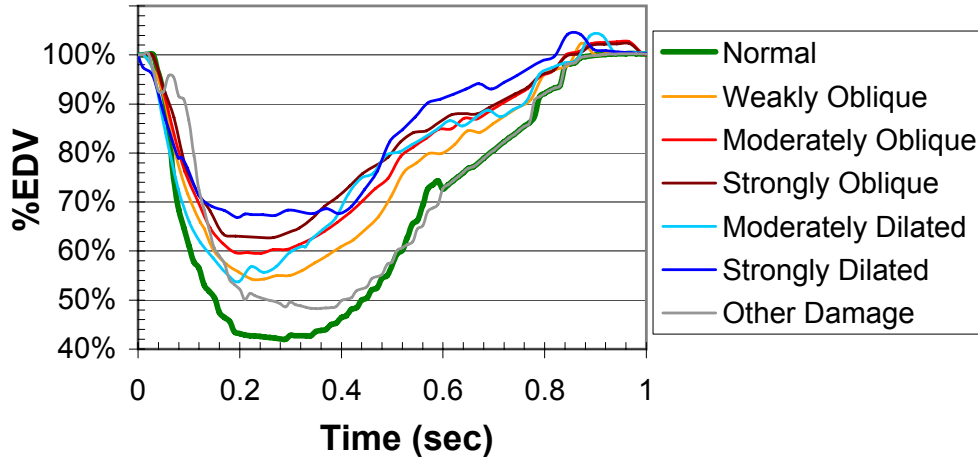


Figure 5.8: Volume of the left ventricle vs. time for each model. The volume is given as a percentage of the initial left ventricular volume, or in other words it is normalized by the end-diastolic volume (EDV). The peak filling rate is calculated from the highest slope during early diastole. Green curve: “Normal” model showing a physiological response with a maximal ejection fraction close to 60% and a rapid early diastolic filling rate. Peak filling rate between $0.4s - 0.55s$. Yellow curve: “Weakly Oblique” model showing a reduced maximum ejection fraction with end-systole at about $t = 0.3s$. Peak filling rate between $0.4s - 0.55s$. Red curve: “Moderately Oblique” model showing a reduced maximal ejection fraction. Peak filling rate is between $0.39s - 0.57s$. Brown curve: “Strongly Oblique” model showing an ejection fraction $< 40\%$. Peak filling rate is between $0.39s - 0.57s$. Blue curve: “Moderately Dilated” model showing a reduced ejection fraction with end-systole volume at $t = 0.2s$. The peak filling rate is between $0.34s - 0.44s$. Dark Blue curve: “Strongly Dilated” model showing the smallest maximal ejection fraction of $\approx 30\%$. Peak filling rate is between $0.4s - 0.55s$. Grey curve: “Other Damage” model showing a change in systolic behavior, but a return to normal during diastole. The peak filling rate is between $0.4s - 0.55s$.

5.3.2 Rate of Filling in the initial diastole period

Figure 5.8 also shows how the rate of filling during the initial diastolic period is affected by damage. In the “Normal” case the change of volume in early diastole is very sharp, which is in agreement with physiological observations. While in some of damaged models it appears to be less than in the normal case, it is hard to judge since the end-systolic volume, and the time at which it is reached, is different for each case. To quantify the observation of the speed of filling we calculated the filling rate. The normal peak filling rate ranges between $1.0 - 3.4$ EDV/sec (where EDV is the end diastolic volume) [75]. Table 5.1 shows the rate of filling for each of the models which was estimated from

early diastole period. The filling rate decreases with the decrease of fiber angle in the apical region, but does not have such a characteristic with the change of shape of the left ventricle. Indeed, in all models except for “Moderately Oblique” fibers and “Strongly Oblique” fibers the rate of filling remains in the normal range.

5.3.3 Torsion of the left ventricle

The torsion was calculated for each of the model cases. Physiologically the maximal torsion in normal cases has been reported between $6^\circ - 9^\circ$ [72, 73]. Table 5.1 shows the maximal torsion for each of the different models. The maximal torsion is within normal range for all the cases, except for the “Moderately Dilated” and “Strongly Dilated” models. Figure 5.9 shows the relationship between the torsion and ejection fraction for each model case. The “Normal,” “Moderately Dilated” and “Strongly Dilated” cases show a double looped response while the “Moderately Oblique,” and “Strongly Oblique” models present only one counterclockwise loop. In the “Weakly Oblique” model the second loop is partially collapsed. Indeed, the greater the change in fiber angle, the more impact can be seen in the shape of the torsion and ejection fraction relationship. The case of “Other Damage” shows neither a characteristic one loop response nor a normal double loop response (figure 5.9G). The same results calculated as twist can be found in figure D.7.

5.4 Discussion and Conclusion

5.4.1 The importance of the normal double looped response

To gain insight into the meaning of our data let us first consider qualitatively why the relationship between twist and ejection fraction might be indicative of heart damage. If the geometry of the heart is normal in both global geometry and in fiber orientation, the relationship between twist (or torsion) and the normalized ejection fraction has the form of a double looped curve (Figure 5.1A). It is possible to understand in a very robust way that this double loop feature is a signature of efficient pumping.

During the systolic period the heart twists as the muscle is contracted (figure 5.1A(i)). This twist is large enough that it is possible to see with the naked eye in open heart surgeries as well as MRI studies. The material of the heart is elastic, so as soon as the muscle fibers are released from contraction, all of the tissue springs back toward the relaxed state (figure 5.1A(ii)). This produces a very rapid untwisting during the onset of diastole, which lowers the pressure inside the ventricle. In turn, this creates a greater pressure difference between the left ventricle and the atrium allowing for faster initial filling. Once the A-V valve opens the untwisting and refilling of the ventricle (decrease in ejection fraction) happen simultaneously (figure 5.1A(iii)). And lastly, at end diastole the filling

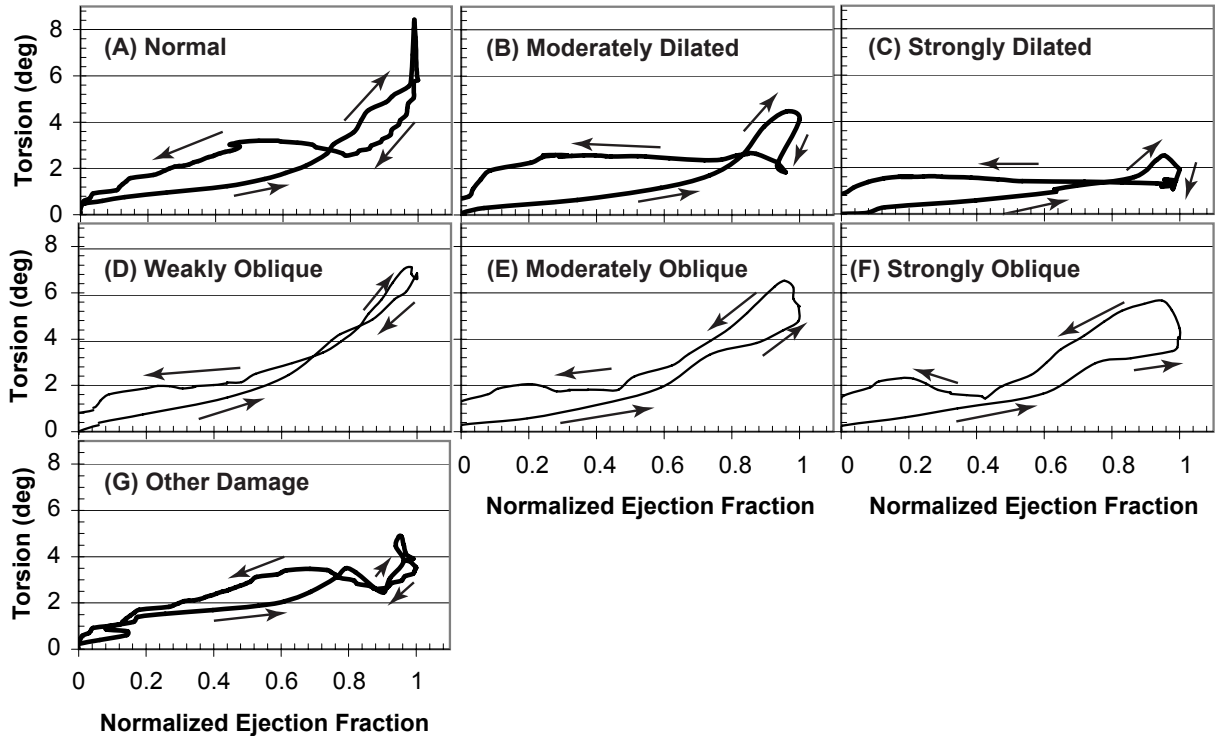


Figure 5.9: Plots of torsion vs. normalized ejection fraction. The arrows indicate the progression through the loops with time. (A) “Normal” model showing a physiological double looped relationship, with a proper maximal value of torsion. (B) “Moderately Dilated” model showing a reduction in maximal value of torsion, but a double loop relationship. (C) “Strongly Dilated” model still has the double looped curve, but a greatly reduced maximal value of torsion. (D) “Weakly Oblique” model showing a collapsed top loop, but no reduction in the maximal value of torsion. (E) “Moderately Oblique” model showing the characteristic to dilated cardiomyopathy (DCM) counterclockwise loop, without a large reduction in maximal value of torsion. (F) “Strongly Oblique” model also showing the characteristic counterclockwise loop with a larger loop than in (E). (G) “Other Damage” model showing randomness in torsion progression close to end-systole.

is much slower, while the untwisting continues (figure 5.1A(iv)).

These characteristics can be used to estimate the slopes of the lines, in a plot of torsion vs. ejection fraction: The slope of the line during early diastole is greater than during systole. During the middle of diastole the slope decreases sharply, and during end diastole it is again greater than that of systole. Figure 5.10 shows a cartoon of the normal torsion and ejection fraction relationship in green. This response, in most cases, is in the form of a double loop. The size of the loops depends on the patient’s age and whether or not other damage is present. But what would it mean if only one loop existed?

If the single loop was clockwise, no impact on the rate of filling would be observed, as the initial diastolic untwisting would still be faster than the systolic twisting (dashed green in figure 5.10). However, a counterclockwise loop would imply that the initial untwisting is not rapid enough to effectively assist with filling (in red figure 5.10), indeed the increase in volume would be hindered by

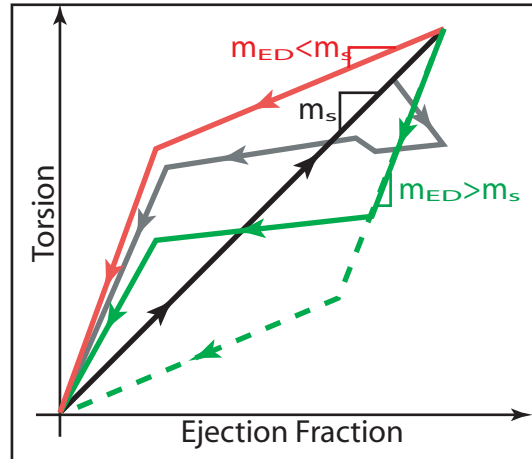


Figure 5.10: Rough schematic drawing of different torsion ejection fraction relationships. The arrows indicate the progression with time. Black line: Systole - with ejection fraction and twisting happening simultaneously. With the slope of the line being m_s . Solid Green lines: Normal classical diastolic progression with early diastolic slope $m_{ED} > m_s$, meaning a fast untwisting. Dashed Green lines: A different possibility for diastole with a rapid early untwist, showing how the bottom loop can take on different sizes or (in this case) disappear all together. Red lines: A diastole progression characteristic of dilated cardiomyopathy with the initial untwisting slower than systolic twist, i.e., the slope of the line $m_{ED} < m_s$. The result is a single counterclockwise loop. Grey lines: Diastolic progression of a case with dead tissue – creating a random response close to end-systole.

the residual twist. As a result the untwisting mechanism is not used effectively to assist refilling. An intermediate case would have the systolic twisting and diastolic untwisting happening at the same rate – which would mean the twist mechanism is not aiding the filling process, but it is also not hindering it.

If the part of the myocardium would become stiffer (as often happens after an infarction due to scarring) the untwisting motion would be unsymmetrical and will depend on the location of the damage. Indeed, the softer tissue would compensate for the stiff portion during the initial contraction, but as the whole structure twists at a maximum the stiffness would impact the dynamics. This would likely affect the relationship between torsion and ejection fraction during maximal twist, disorganizing it. As a result we expect the top loop to lose its symmetry and shape (grey in figure 5.10).

From studies performed on patients it is known that the single counterclockwise loop response, a sketch of which is shown in figure 5.1B, is characteristic of dilated cardiomyopathy [73]. A different type of response occurs for other types of damages [27–29].

5.4.2 Comparing different model results

The double looped response can be reproduced by the “Normal” model that also matches physiological maximal ejection fraction, filling rate, and maximal twist. In this model the myocardium is

defined by a bundle of fibers in the shape of a double helix. The overall shape of the left ventricle is that of an elongated paraboloid, and the fiber orientation in the double helix is consistent with physiological observations. The excitation pattern mimics that of the heart, with the contraction starting near the apex and propagating outwards. The detailed discussion of this model will be published elsewhere. Here, it is important to note that in this model the relationship between torsion (twist) and ejection fraction has the characteristic double looped response (Figure 5.9A). This shows that our model, however simplified, is capable of reproducing the physiological double-looped relationship between torsion and ejection fraction. So does the changes in geometry and fiber orientation affect the response?

As the fiber orientation is changed to be more and more oblique, the rate of filling decreases and the relationship between twist and torsion takes on the form of a counterclockwise single loop and the maximal ejection fraction is reduced. In the case of “Weakly Oblique” model the top loop is collapsed (figure 5.9D), and as the fiber angle is decreased for models “Moderately Oblique” and “Strongly Oblique” there is only one counterclockwise loop present (figures 5.9E and 5.9F). For these models with a change in fiber angle, the maximum torsion is decreased but it is still greater than what is observed in DCM cases (less than 4°).

For the model cases of normal fiber orientation and dilated left ventricle shape the ejection fraction is also decreased. Indeed, our results show that the greater the dilation of the left ventricle the smaller the maximum ejection fraction. However, the rapid filling rate remains within physiological limits and is unrelated to the degree of dilation. Therefore it is not unexpected that the relationship between torsion and ejection fraction remains in the form of the double loop for both the “Moderately Dilated” and “Strongly Dilated” models (figures 5.9B and 5.9C). However, the torsion response is not completely normal, as the maximal torsion is greatly reduced, and is below 4° .

We also took a look at other damage to ensure that the one looped response is characteristic of the change in fiber orientation and not other direct changes to the band. A simulation of a case where a layer of the myocardium is dead (non-active) resulted in greatly reduced maximal ejection fraction and peak filling rate. However, the relationship between torsion and ejection fraction does not take on the form of a single counterclockwise loop (figure 5.9G). Instead, the twisting and untwisting become irregular near maximal values.

5.4.3 Conclusion

The series of models were created to test whether the change of fiber angle or the change of left ventricular shape is the dominant factor in creating the characteristic failing response of dilated cardiomyopathy. In a heart with dilated cardiomyopathy both of these factors are present, but it is important to understand which of them has to be the primary target during the reconstruction surgeries.

We show that only the change in fiber angle produces the characteristic counterclockwise single loop relationship between torsion and ejection fraction. Neither simply dilating the shape of the ventricle nor introducing other damage has such an effect. As we have discussed in section 5.4.1 this relationship can be used to judge the efficiency of the ventricle pumping. Indeed, our results show that unless the fiber angle is fixed the peak rate of filling will remain low, which is detrimental to a patient's exercise capacity [76].

It would be erroneous to assume that fixing the fiber angles alone is sufficient to completely restore the pumping efficiency. Indeed, we show that by dilating the shape of the left ventricle we greatly reduce the maximal ejection fraction as well as the maximal twist. However, our results presented in this chapter demonstrate that the fiber angle is the single predominant determinant of the reduced functionality of the heart, and, therefore, it should be the primary target of surgical procedures directed at ventricle restoration in patients with dilated cardiomyopathy.

Chapter 6

The filled-out heart model: pressure in the left ventricle

6.1 Introduction

In the previous chapters we have shown how the double helical band can be used to simulate the volume changes and the twisting of the left ventricle. This simplified model can be a valuable tool in discerning different underlying geometrical factors behind pumping efficiency and twisting motion of the healthy heart as well as some pathological defects. However, in constructing a model that operates in a vacuum we were unable to simulate the force that is applied to the blood to pump it out; by the same token, we were unable to simulate the force which acts on the muscle band and which has to be overcome by the muscle band in order to perform its motion. In other words, the pressure in the left ventricle cannot be simulated without taking into account the interaction of heart tissue with blood, which, in turn, requires that we explicitly take into account, at least in some form, the collagen matrix and other tissue in the heart. In general, it is a very ambitious and at present still rather remote goal. However, to place the double helical band model on the solid foundation it is important to show that this model, at least in principle, is capable of generating the correct physiological forces when acting inside a collagen network.

The pressure in the aorta is about 14kPa (105mmHg), which means that the aortic valve will not open until the pressure in the left ventricle reaches above 14kPa. In order to fully generate the pressure and volume of the left ventricle it would be necessary to create a high fidelity model of the different materials inside the heart. This would include separate material models for the endocardium, epicardium, and myocardium. Each of these tissues has a different task during the cardiac cycle. The endocardium and epicardium are made from a membrane that is very resistant to expansion, but as with any membrane it will easily bend under contraction. The myocardium on the other hand, is a combination of muscle fibers, which are the active elements, and a collagen network, which has a high bulk modulus, but shears very easily. Considering that in combination

these materials provide a non-linear material response, we are again faced with a problem of an overabundance of parameters. To get around this problem we will first look at the pressure generated by the left ventricle, without considering the ejection fraction.

6.2 Methods

6.2.1 Geometries of the chambers

The ventricle walls need to completely enclose the double helical band of muscles. As described in detail in chapter 2 the equations for the double helical band are written by first specifying the z -coordinate of the centerline of the band in terms of the polar coordinate θ :

$$z_{cent} = C_1 - C_2 \frac{\theta^{A_1}}{A_2} \exp\left[-\frac{\theta}{B_2}\right] \quad (6.1)$$

where C_1 , C_2 , A_1 , A_2 , B_2 are constants. The polar coordinate θ varies $\theta_{max} \geq \theta \geq 0$. Based on this the three-dimensional parametric equations for the band are:

$$\begin{aligned} z_{band} &= z_{cent} + \xi, & r_{band} &= \sqrt{z + C_3} [\text{Factor 1}] [\text{Factor 2}] + \zeta, \\ x &= r \cos \theta, & y &= r \sin \theta, \\ \text{Factor 1} &= 1 + C_4 \cos\left(\frac{\theta - \theta_{crossing}}{2}\right), \\ \text{Factor 2} &= 1 + C_5 \exp\left(-(\theta - \theta_{right})^2\right), \end{aligned} \quad (6.2)$$

where C_3 , C_4 and C_5 are constants. The parameters $-w/2 \leq \xi \leq w/2$ and $0 \leq \zeta \leq t$ control the position in the width and thickness directions respectively, where w and t are the width and thickness of the band. The Factor 1 is introduced to avoid self-overlap of the band at $\theta_{crossing} = \pi\left(-1 + \cot \frac{\pi}{A_1 B_2}\right)$ and $\theta_{crossing} + 2\pi$. The factor bends the centerline away from self-crossing. We also introduce Factor 2, which is only significant in the region of anterior surface and describes the fact that this surface bends significantly outward from the septum. We choose the middle of anterior surface to correspond to $\theta_{right} = 3.8\pi$. The position of the apex of the left ventricular chamber is taken to be at $z = C_3$.

To describe the surface of the heart we assume that at each cross-section by a r - z plane containing the long axis of the left ventricle (z -axis), the wall has the form of a parabola. The parabolic constant, A , of the projected parabola is calculated as $A_{band}(\theta, \xi, \zeta) = (z_{band} - z_{apex})(\theta, \xi, \zeta)/r_{band}^2(\theta, \xi, \zeta)$, where the position at the apex varies depending on the layer between $C_3 \leq z_{apex} \leq C_3 - t$, from the inside layer to the outside layer. To easily define the envelopes for the outside of the heart and the inside of each ventricle we define the parabolic constant for a surface that would sweep the outside

of the band and the inside of the band:

$$A_{out,band}(\theta) = \min_{\xi} (A_{band}(\theta, \xi, t)), \quad (6.3)$$

$$A_{in,band}(\theta) = \max_{\xi} (A_{band}(\theta, \xi, 0)). \quad (6.4)$$

To define the outside wall of the heart for a closed surface with $0 < \theta \leq 2\pi$ the parabolic constant is then calculated as three separate segments: The segment that defines the outside of the right heart based on the section of the band that belongs to the right heart; the segment that defines the left ventricle is based on the outer portion of the left ventricle band; the segment that defines the rest of the right heart is based on the linear interpolation between the end of the band and a symmetrical position of the left ventricle.

$$A_{out}(\theta) = \begin{cases} A_{out,band}(\theta_{max}) - \frac{A_{out,band}(\theta_{max}) - A_{out,band}(\theta_{max} - \theta_{RH})}{\theta_{RH}} \theta, & : 0 < \theta < \theta_{RH} \\ \min(A_{out,band}(\theta), A_{out,band}(\theta + 2\pi)) & : \theta_{RH} \leq \theta \leq 2\pi - \theta_{RH} \\ A_{out,band}(\theta + 2\pi) & : 2\pi - \theta_{RH} < \theta \leq 2\pi \end{cases} \quad (6.5)$$

$$A_{in}(\theta) = \begin{cases} A_{in,band}(\theta_{max}) - \frac{A_{in,band}(\theta_{max}) - A_{in,band}(\theta_{max} - \theta_{RH})}{\theta_{RH}} \theta, & : 0 < \theta < \theta_{RH} \\ \max(A_{in,band}(\theta), A_{in,band}(\theta + 2\pi)) & : \theta_{RH} \leq \theta \leq 2\pi - \theta_{RH} \\ A_{in,band}(\theta + 2\pi) & : 2\pi - \theta_{RH} < \theta \leq 2\pi \end{cases} \quad (6.6)$$

In these equations $\theta_{RH} \approx 0.7\pi$ defines the size of the right heart. We define the septum wall to be between $2\pi + \theta_{RH} < \theta < 2\pi - \theta_{RH}$. The parabolic constant for the septum wall is then defined as:

$$A_{out}(\theta) = \begin{cases} \min(A_{out,band}(\theta), A_{out,band}(\theta - 2\pi)) & : 2\pi + \theta_{RH} \leq \theta \leq 2\pi \\ A_{out,band}(\theta) & : 2\pi < \theta \leq 2\pi - \theta_{RH} \end{cases} \quad (6.7)$$

$$A_{in}(\theta) = \begin{cases} \max(A_{out,band}(\theta), A_{out,band}(\theta - 2\pi)) & : 2\pi + \theta_{RH} \leq \theta \leq 2\pi \\ A_{out,band}(\theta) & : 2\pi < \theta \leq 2\pi - \theta_{RH} \end{cases} \quad (6.8)$$

The resulting two chamber shell can be seen in figure 6.1. In order to simulate pressure we enclose the left ventricular chamber with a cap in the form of a disk. In order to calculate the coordinates of each node on the shell we vary $z_{apex} \leq z \leq \max z_{band}$.

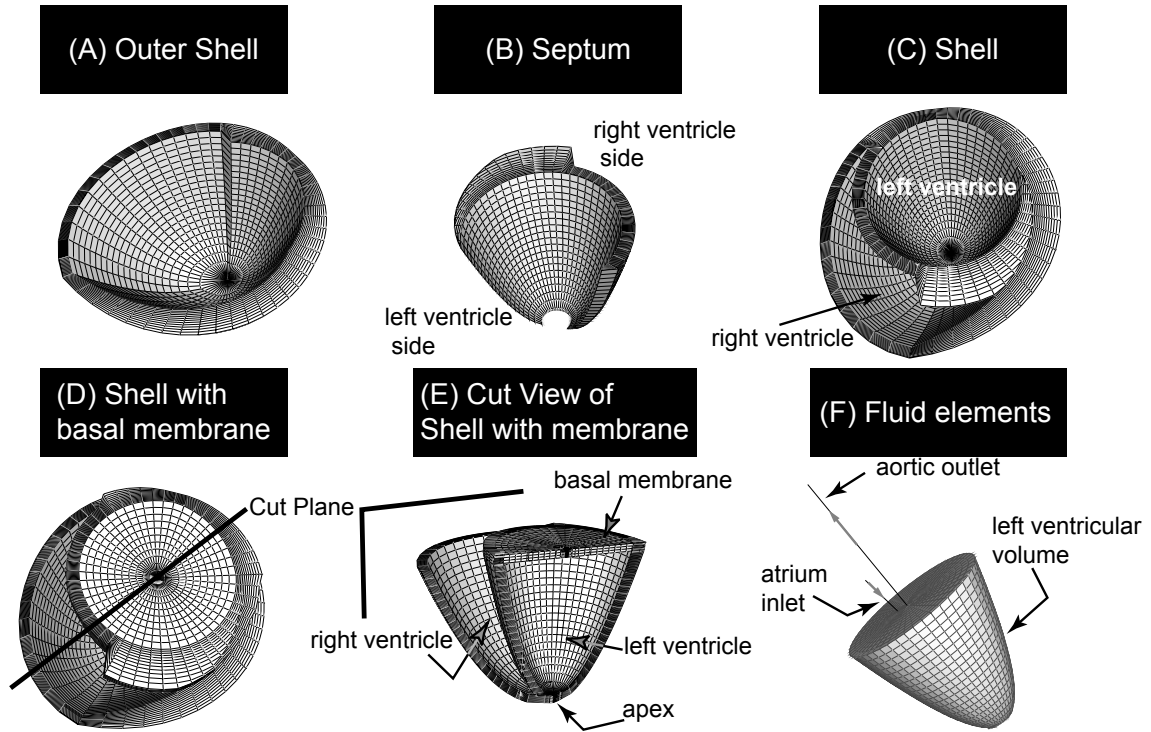


Figure 6.1: Images of the elements of the filled out model. (A) The outside shell of the heart. (B) The septum wall, with the left ventricle at the concave side and the right ventricle at the convex side. (C) The walls of the two chambers, with the left and right ventricular chambers labeled. (D) The shell of the heart with the basal membrane wall capping the left ventricular cavity. The thick black line indicates the cut plane seen in the next picture. (E) The cross-sectional view of the complete shell. The left and right ventricular chambers are indicated. The basal membrane closes of the left ventricle. The apex is the lowest point of the left ventricle. (F) The fluid elements of the model include the left ventricular volume (“Hydrostatic Fluid” element), and the two “Fluid Link” elements: the atrium inlet through which blood enters the ventricle and the aortic outlet through which blood leaves the ventricle.

6.2.2 Active Material Properties

The strain (ε) caused by the excitation is given by:

$$\begin{bmatrix} \varepsilon_{11} \\ \varepsilon_{22} \\ \varepsilon_{33} \\ \varepsilon_{12} \\ \varepsilon_{13} \\ \varepsilon_{23} \end{bmatrix} = \begin{bmatrix} \alpha_{11} \\ \alpha_{22} \\ \alpha_{33} \\ \alpha_{12} \\ \alpha_{13} \\ \alpha_{23} \end{bmatrix} \text{Ex}, \quad (6.9)$$

where Ex is the excitation parameter, and α_{ij} is the excitation expansion factor in the ij direction. For convenience we choose for $0 \leq \text{Ex} \leq -1$, where 0 is fully relaxed and -1 is fully contracted. The

active material properties depend on the direction of the fibers. As a result, the strain in response to excitation in the active material is given by $\varepsilon_{fiber}^{Ex} = 0.15Ex$ in the fiber direction and in both perpendicular directions as $\varepsilon_{perpend}^{Ex} = -0.085Ex$. However, because the original material is oriented in the cylindrical coordinates, i.e., directions (1, 2, 3) correspond to (r, θ, z) , and not the natural fiber coordinates, we need to rotate the excitation matrix such that the contraction direction corresponds to the fiber direction. To do so we calculate the tangent ($\hat{\mathbf{t}}$), normal ($\hat{\mathbf{n}}$) and binormal ($\hat{\mathbf{b}}$) of the fiber direction in terms of cylindrical coordinates. The rotation matrix (\mathbf{R}) is then given by:

$$\mathbf{R} = \begin{bmatrix} t_r & n_r & b_r \\ t_\theta & n_\theta & b_\theta \\ t_z & n_z & b_z \end{bmatrix}. \quad (6.10)$$

The excitation expansion factors are then calculated:

$$\begin{bmatrix} \alpha_{11} & \alpha_{12} & \alpha_{13} \\ \alpha_{12} & \alpha_{22} & \alpha_{23} \\ \alpha_{13} & \alpha_{23} & \alpha_{33} \end{bmatrix} = \mathbf{R} \begin{bmatrix} 0.15 & 0 & 0 \\ 0 & -0.085 & 0 \\ 0 & 0 & -0.085 \end{bmatrix} \mathbf{R}^T. \quad (6.11)$$

The choice of Young's modulus is challenging because the material of the myocardium is very complex. We know that the bulk modulus the tissue can be as high as $1.72 \times 10^9 \text{Pa}$ [16]. The Young's modulus of the material is taken to be at the following values $E_Y = 1 \times 10^9 \text{Pa}, 1 \times 10^6 \text{Pa}$. The Poisson's ratio is taken to be $\nu = 0.48$; in principle, the active material in the heart is nearly incompressible, which would correspond to $\nu = 0.5$, but absolute incompressibility is neither realistic nor computationally simple, so we choose the value closest to 0.5 and still simple to implement computationally, which is $\nu = 0.48$.

6.2.3 Non-active material properties

The collagen matrix that surround the muscle fibers is very easy to shear. Indeed the shear modulus is several orders of magnitude smaller than the modulus of the muscle. For this experiment, for simplicity, we assume an isotropic behavior for the non-active material. Therefore, the shear modulus (G) would be given by $G = E_Y / [2(1 + \nu)]$. As a result, we estimate the Young's modulus of the material to be $E_Y \approx 0.25 \times 10^6 \text{Pa}$. The Poisson's ratio is taken to be $\nu = 0.48$, for the same reason as the active material.

6.2.4 Excitation

For the purpose of specifying the excitation we assume that the band inside the shell is a real physical entity. The excitation is then specified as a function of the spatial coordinate along the band (s) and time (t).

Purkinje wave excitation: The spatial wave modeled after the Purkinje nerve network in the heart dictates the excitation according to the following formula:

$$\text{Ex}(s, t) = \begin{cases} 0 & : t < t_1 \\ \frac{-(t-t_1)}{t_2-t_1} & : t_1 \leq t < t_2 \\ -1 & : t_2 \leq t < t_3 \\ \frac{-(t_4-t)}{t_4-t_3} & : t_3 \leq t < t_4 \\ 0 & : t \geq t_4 \end{cases} \quad (6.12)$$

where t_1, t_2, t_3, t_4 are given by:

$$\begin{bmatrix} t_1 \\ t_2 \\ t_3 \\ t_4 \end{bmatrix} = \begin{cases} 0 \leq s < AI & : \begin{bmatrix} \frac{0.55s_{max}}{AI}(AI - s) \\ \frac{0.55s_{max}}{AI}(AI - s) + 0.075 \\ t_3 = \frac{0.45s_{max}}{AI}(AI - s) + 0.25 \\ \frac{s_{max}}{AI}(AI - s) + 0.475 \end{bmatrix} \\ AI \leq s < s_{max} & : \begin{bmatrix} \frac{0.30s_{max}}{s_{max}-AI}(s - AI) \\ \frac{0.30s_{max}}{s_{max}-AI}(s - AI) + 0.075 \\ \frac{1.1s_{max}}{s_{max}-AI}(s - AI) + 0.325 \\ \frac{1.25s_{max}}{s_{max}-AI}(s - AI) + 0.375 \end{bmatrix} \end{cases} \quad (6.13)$$

where $AI = 0.85s_{max}$ is the position of the apex, and s_{max} is the length of the band.

Temporal excitation: For the temporal wave, there was no dependence on the spatial coordinate, and the activation was described by a table with linear approximations between values.

Time (sec)	Excitation
0	0
0.055	-0.25
0.09	-0.50
0.13	-0.75
0.225	-0.938
0.375	-1
0.415	-0.75
0.47	-0.50
0.545	-0.375
0.66	-0.25
0.83	-0.125
1	0

6.2.5 Computational Methods

In order to model this three-dimensional geometry with the complex material properties we utilize the commercial finite element software ABAQUS Standard 6.51 [74]. The shell of the the ventricles is broken into three-dimensional brick elements (8 node elements). These are connected at the apex and at the borders between the septum and outside wall with wedge elements (6 node elements). The elements are shown in figure 6.1 panels A-E.

6.2.6 Modeling the Blood

The blood filling the left ventricle is modeled such that we assume that the pressure inside the ventricle is constant. As a result, the fluid can have a different volume or pressure, but there are no other degrees of freedom. The density of the fluid is taken to be 1 g/mL. In ABAQUS, the fluid is modeled as a “Hydrostatic Fluid” element (figure 6.1F). Physically, this approximation is justified because all motions in the heart are slow compared at the speed of sound in the blood, which means pressure in the blood inside the ventricle adjusts adiabatically to the motions of the heart. Consequently, we model the inflow and outflow as a bulk mass transfer not as a fluid dynamics problem.

6.2.7 Valves

The mitral and aortic valve are included in the model. The valves are constructed by creating “Fluid Link” elements (figure 6.1F). We specify the properties of this element such that the mitral valve “Fluid Link” element can have flow going into the ventricle only, while the aortic valve “Fluid Link”

element can only have flow going out of the ventricle. The property of a “Fluid Link” element is specified as a relationship between the difference in pressures (ΔP) and the mass flow rate (q). The relationships are specified as follows:

$$q_{aortic} = \begin{cases} 0 & : \Delta P_{aortic} \leq 0 \\ C_v \Delta P_{aortic} & : \Delta P_{aortic} > 0 \end{cases} \quad (6.14)$$

$$q_{mitral} = \begin{cases} -C_v \Delta P_{mitral} & : \Delta P_{mitral} < 0 \\ 0 & : \Delta P_{mitral} \geq 0 \end{cases} \quad (6.15)$$

where $\Delta P_{aortic} = P_{LV} - P_{aorta}$ and $\Delta P_{mitral} = P_{LV} - P_{atrium}$. For this study we arbitrarily picked the rate of flow constant to be $C_v = 10$. This value only controls how fast the fluid is transferred from or to the left ventricular chamber, and at this stage its biggest impact is on the convergence of the model. The boundary condition on the aorta are specified such that the pressure is constant at $P_{aorta} = 14\text{kPa}$, while the pressure in the left atrium is kept at $P_{atrium} = 0\text{Pa}$.

6.2.8 Data Analysis

The results of simulations done in ABAQUS Standard were analyzed with the visualization software ABAQUS CAE 6.51. The pressure and volume of the hydrostatic fluid inside the left ventricle chamber were specified as direct output.

6.3 Results

In this chapter we are investigating the ability of the model which has the double helical band as an internal “engine” to give rise to physiologically high pressures. Focusing on the left ventricle we can think of the chamber as a bag of fluid. If the walls of the bag are made from patches of different materials, when the pressure in the bag is increased, the bag bulges out in the place of the soft material. This is precisely what we observe in the simulations – the ventricle bulges out through the space in between the band material, where only the softer collagen material is present (figure 6.2). As a result we can conclude that the maximal pressure possible in the left ventricle will be governed by the softest material present.

As a first experiment we run the case with no separate endocardium material. This means that the softest material has the Young’s modulus of 0.25MPa . Figure 6.3A shows the pressure in the left ventricle as a function of time. The pressure curve is piece-wise linear, because the pressure in the fluid faithfully follows the degree of excitation in the active material. The pressure in the left ventricle, at its maximal value, reaches the aortic pressure of 14kPa , which is enough to open the aortic valve. At that point the pressure stays constant until the contraction of the muscle is released.

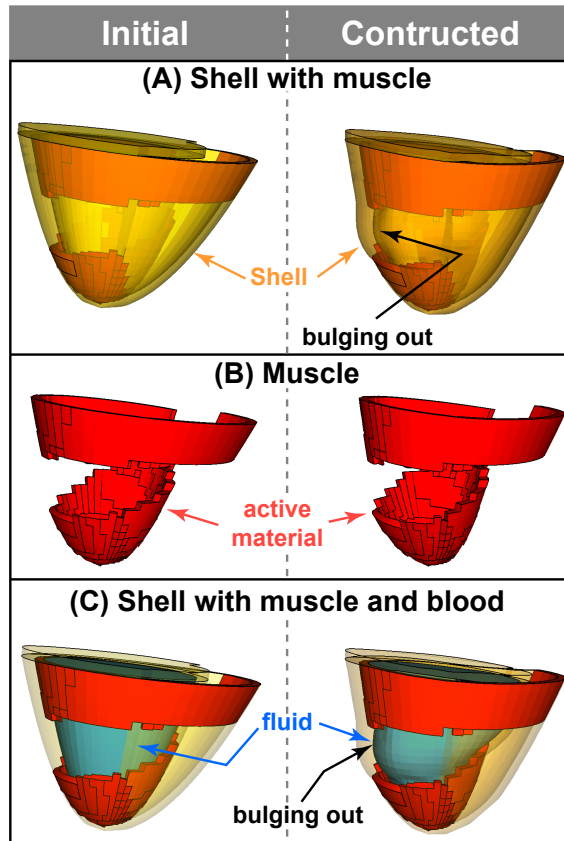


Figure 6.2: The effect of bulging out through the soft material. The chamber walls are shown in transparent yellow, the active material (muscle) is shown in red, and the fluid is shown in blue. The left panels show the initial shapes, while the right panels show the model at maximum excitation. (A) The chamber walls with the active material inside. During contraction the bulging out of walls is plainly visible. (B) The active material is isolated. Here it is easy to see that the walls constrain the possible deformation. (C) The walls with the active material and the fluid shown inside. Here it is clearly visible how the fluid pushes out in between the active material sections.

For a Purkinje type spatial wave the pressure in the left ventricle as a function of time is plotted in figure 6.3B. This curve is much smoother, but the maximal pressure still reaches the physiological aortic pressure at 14kPa.

When the inner layer of the left ventricular chamber is forced to be stiffer than the rest of the soft tissue, it becomes the softest material exposed to the fluid. The results can be seen in figures 6.3C for the spatial wave. As can be seen from the plots the aortic pressure of 14kPa is reached much faster and as a consequence the ejection period is longer. Additionally, the pressure continues to increase because in this case the flow rate out of the ventricle is not fast enough to accommodate the rapid increase in pressure. This shows that we can reliably exert the necessary pressures, even though the heart tissue is a combination of different types of materials.

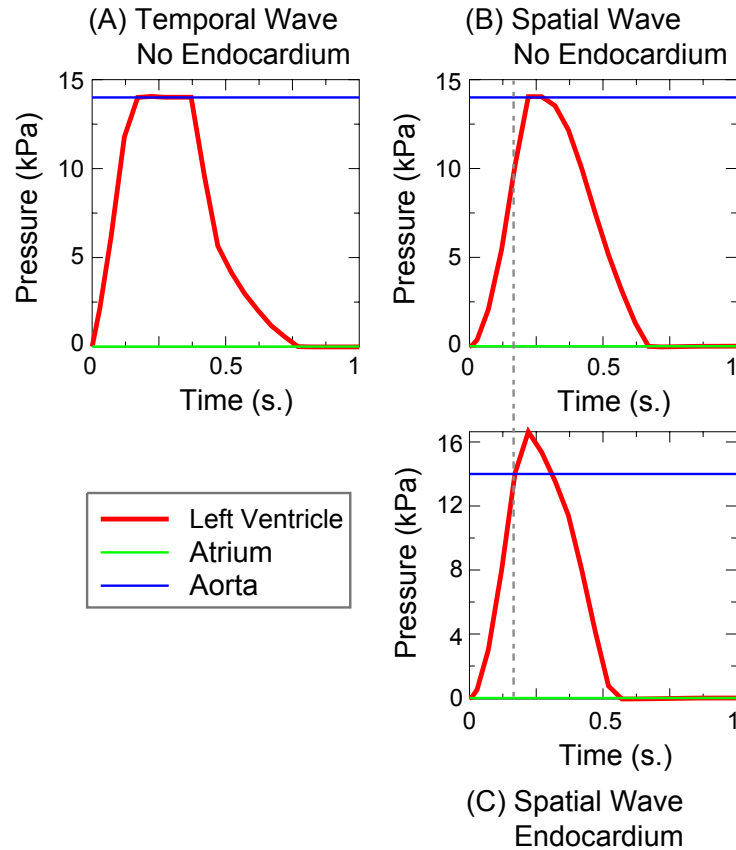


Figure 6.3: Plots of pressure vs. time. The left ventricle pressure is indicated in red, the aorta pressure is in blue, and the atrium pressure is in green. (A) Temporal wave contraction, no endocardium tissue – the aortic pressure is reached and there is a period of ejection. (B) Spatial wave, no endocardium tissue. Here the period of ejection is slightly shorter than in (A) because the temporal wave excitation scheme holds the band at maximal contraction for longer. (C) Spatial wave, with the endocardium made stiffer than the rest of the soft tissue. As indicated by the dashed grey line the left ventricular pressure reaches the aortic pressure much faster than in case (B), and therefore the period of ejection is longer.

6.4 Conclusion

In this chapter we tested whether the double helical muscle band is capable of producing physiologically high left ventricular pressures. We showed that the maximal pressure is limited by the modulus of the softest material exposed to the blood. It is known, from experimental tests on heart tissue, that the modulus of the tissue ranges over several orders of magnitude. For example the bulk modulus of collagen is 1.72GPa (see textbook by Humphrey page 677 [16]). By contrast, from experimental tests done on the endocardium the modulus ranges from 1kPa to 10kPa with strain ranging from 0.03 to 0.06 (see textbook by Humphrey page 657 [16]). From these experiments we see that not only does the modulus vary greatly, but the constitutive relation is nonlinear. Our results, therefore, are estimates of the possible pressures that can be produced in the ventricle. However,

because collagen is prevalent throughout the myocardium, the fact that we produce physiologically high pressures with materials of Young's modulus smaller than the modulus of the collagen by several degrees of magnitude shows that the double helix is capable of causing sufficient force to support ejection.

Chapter 7

Outlook and possible future directions

Since time immemorial, mathematicians and artists alike fancied helices and spirals. Prominent in ancient ornaments, spiral shape most famously showed up in Watson and Crick's double helical model of DNA. Helical shapes of fibers, bands, and bundles is generally one of the Nature's greatest schemes for self-assembly, growth, and structural integrity presented in: aromatics [77] (see also News and Views on this subject in [78]), tendrils of plants [79], proteins, DNA [80], the heart, etc. How these helical structures self-assemble is often a mystery: sometimes, like in proteins, it is possible to show that the transformation is entropically driven [81], but oftentimes it is not known how these helices form [82]. As Martin Kemp famously observed in his elegant treatise on "spirals of life," the helical living designs are generally well known for their static features, rather than their active function [63]. Of course, airplane propeller or bacterium flagella represent rotating spiral designs, but in both cases the spiral itself is still passive.

That is why we were much excited to learn that while all the fibers in the myocardium were helically organized for structural integrity, the active muscle fibers in the heart appear to have a sort of double helical organization as well, as it was recently observed by the modern sophisticated imaging technique – version of MRI called DTMRI [23]. The apparently dominant helical organization of fibers in the heart raises a more serious question: Is it possible that spiral organization of the active myofibrils may also shed light on the complex dynamics of the heart?

We started thinking that these spiral structures might hold the key to understand the wonderfully efficient function of the heart. Indeed, the muscle band consists of a group of parallel muscle fibers, each of which cannot contract much over 15%, yet the volume exchange ratios, ejection fractions, in the ventricles can exceed 60%. Is it possible to gain an insight into these paradox by invoking the spiral geometry of the muscle band?

H.T. Crane once wrote on the general problems of biological growth. He pointed out, that while the process in the whole can be too complex for us to produce an equation describing it, we can

understand it if we know “the principles involved and something of the order of their importance” [62]. In studying the development of the heart I followed this road-map.

The most efficient way to approach these problem is by using computational modeling.

We constructed an efficient computational model in chapter 2 by assuming that the myofibrils are arranged in the heart muscle is a single band that starts from the pulmonary aorta, hugs the right ventricle, winds down to the apex, as the descending segment, and then spirals up to the aortic valve as the ascending segment. We assumed that this band reacts to the local strain created by excitation of the muscle cells as an elastic body, while the rest of the myocardium is a passive material that does not create any strain and just bounds the volume. This allowed us to resort to very advanced computational techniques used in other well developed engineering fields, and even use a commercially available finite element package – ABAQUS [74]. Simplistically, this program solves elastic equilibrium equations for each small cuboid, and then puts together the evolution of the whole structure by continuity.

The advantage of computational modeling is that once the computational model is set up it allows for easy testing of a wide variety of conditions. We can vary the fiber angles, width, thickness, and ventricle dimensions. The band can shorten as a whole, or parts of it can contract independently of each other. This allows us to create complicated contraction schemes inside the band.

The simplest dynamic scheme is to excite all the nodes at the same time and have the elements contracting in sync, making a uniform contraction. More interestingly, we are able to mimic the action of the Purkinje network by considering an excitation/relaxation wave traveling along our band starting at the apex.

The first success of our model is its ability to effortlessly resolve the above mentioned paradox and to reproduce the large ejection fraction, despite the small muscle strain. It came as a pleasant surprise that our model easily matches not only the physiological maximum ejection fraction, but also the left ventricular volume evolution with time as was shown in chapter 2.

In chapter 3 we use this approach of focusing on dominant structures in the heart to investigate the causes of the forces that play an integral role in the self-assembly of the adult four chamber heart from the embryonic tube heart. We showed that the helical form of the fibers surrounding the heart tube in combination with a spatial excitation wave is able to produce the twisting forces necessary for the initiation of self-assembly.

We then turned, in chapter 4, to a much more sensitive property of the heart, namely the timing relationship between twist and ejection fraction, which is considered a potentially powerful diagnostic tool of ventricular health. While comparing the model results to actual physiological data, we were gratified to find that we can match the double looped response observed in nature, and that this is possible only with an excitation that approximated the physiological scheme.

In chapter 5 we used our model to consider pathological behaviors of the heart. Indeed, because

of the relatively simple nature of the double helical model we are able to test different types of damage separately, and to discern the causes of pathological behavior. As we have shown, for dilated cardiomyopathy the change in fiber angle is much more critical than the change in gross geometry of the left ventricular chamber. Additionally, we were able to match experimental results for the relationship between twist and ejection fraction seen in cases of dilated cardiomyopathy, giving more credence to the computational model.

Finally, in chapter 6 we demonstrated that the double helical muscle band used as an engine inside a collagen shell can produce physiologically high pressures. This filled-out model will be the springboard into further research. Indeed, to model both the pressure generation and volume ejection of the ventricles we need to match the highly nonlinear behavior of the heart tissue. It will be necessary to model the endocardium membrane that is very resistant to stretching, as well as the ability of the collagen matrix to shear with the movement of the muscle fibers, while increasing the width of the walls.

What have we learned from this model? In general the greatest benefits of modeling is to gain insight into the dominant structures and processes. In our case, the model was initially proposed by Torrent-Guasp and supported by modern imaging techniques, such as DTMRI, but is still not uniformly accepted by researchers in the field. Our modeling results indicate that helical arrangement of the muscle in the heart does provide a natural and simple explanation of heart pumping. This insight predicts that the heart cells grown around a scaffold in recent breakthrough research by a Minnesota group will need an additional input to provide them with proper organization, in order to transform their wonderfully achieved beating into efficient pumping. We hope our results will be valuable in this endeavor.

The imagination of great artist allowed M.C. Escher to portray the human face as an elegantly bent paper stripe (Rind 1955). When we look at the image we unmistakably see the human head and face, and even quite expressive face. Is this model physiologically correct, does it involve all the physiologically relevant details? No, it does not. But it does capture something important – in fact, something most essential for the artist. We hope that, similarly, our model, however simplified, does capture something most essential. Definitely, it can serve as a starting point for further research, as it helps asking useful questions to be addressed by MRI and other studies.

Appendix A

Additional Analytical Calculations

A.1 Inherent limit on pumping efficiency of structures with non-helical fibers

Let us first consider a tubular and a parabolic pumping chamber with non-helical fibers. We impose the same boundary and material conditions as were described in section 2.2. We expect the biggest ejection fraction to be produced by the biggest possible fiber contraction of 15%.

A tube volume is given by $V = \pi r^2 L$, where r is the radius and L is length. For a parabolic chamber the volume is given by $V = (1/2)\pi r_{max}^2 L$, where L is the height of the parabola, and r_{max} is the radius at height L . For both of these, if the fibers are arranged circumferentially the circumference, and thus the radius will decrease by 15%, i.e., $r = 0.85r_0$.

Using equation 2.8 the ejection fraction would be about 28%. However, in the tube model the ejection fraction would actually be lower, because the two ends of the tube are fixed, so that the fibers close to the ends cannot contract and will simply exhibit stress in response to excitation. This is also the case for the basal region of the parabolic chamber.

If the fibers are arranged longitudinally then the in the tube model there will be no pumping at all because the length is restricted from shortening by the boundary conditions. For the parabolic chamber the length will be reduced by 15%, and thus the ejection fraction would also be 15%.

Appendix B

Analytical estimate of energy efficiency of twist vs. contraction pumps

B.1 Introduction

There is heuristic evidence that twisting action is very important in pumping mechanisms [64]. Here we present a range of analytical models called on to illustrate one of the reasons behind nature's propensity of taking advantage of the effect of twisting.

B.2 Pumping from a Cylindrical shell

We create analytical models for tube-pumping mechanisms. Such pumps are used extensively, for example inside the body to increase the flow through the vasculature. We will use the notion of the ejection fraction to evaluate the output of our simple pumps. The ejection fraction, EF , is given by the change of volume normalized by the initial volume:

$$EF = \frac{V_0 - V}{V_0} = 1 - \frac{V}{V_0}. \quad (\text{B.1})$$

Let us considering two different systems, one that has the tube contracting radially while the other is twisted.

B.2.1 Radial shortening of the tube

Let us first consider squeezing the tube radially, as seen in figure B.1. In this case we have circular wires, with radius r_{wire} arranged around a cylinder of constant length $L = L_0$, and initial radius of

r_0 , and the initial fiber length of $D_0 = 2\pi r_0$. The volume of the cylinder is simply given by:

$$V = L \cdot \pi r^2. \quad (\text{B.2})$$

In this model the wires will shorten around the tube by a factor of ε , meaning that the fiber length is $D = (1 - \varepsilon)D_0 = 2(1 - \varepsilon)\pi r_0 = 2\pi r$. And thus $r = (1 - \varepsilon)r_0$. Since the length of the cylinder is constant we use equation B.1 and get the ejection fraction to be:

$$EF = 1 - \frac{r^2}{r_0^2} = 1 - \frac{(1 - \varepsilon)^2 r_0^2}{r_0^2} = 2\varepsilon - \varepsilon^2. \quad (\text{B.3})$$

The difficulty with such a pump is that a device which uses shortening of wires to pump would be energetically very expensive, which is easy to prove to oneself by simply bending a wire and then trying to shorten it – it takes a great deal more effort to shorten something than it does to bend it. However, there are at least two simple ways to create radial shortening in the tube while bending the wires. In the first case, the wire slides into a spiral form, as seen in figure B.2(a). In this case the model would become invalid once the radius of the tube becomes comparable to the radius of the wire. A second simple device is akin to a snake eating its own tail, where we create a slit in one half of the wire that the second half can slide into (figure B.2(b)). In this case the minimum circumference can be only half of the wire length, $\varepsilon_{max} = 0.5$, but that would mean an ejection fraction of $EF = 75\%$, which is sufficient for most applications. Thus both of these models are considered.

The work used to achieve the volume change for both of these models is the bending energy of the wires. Assuming that the fibers are initially stress free, and that linear elasticity applies, the

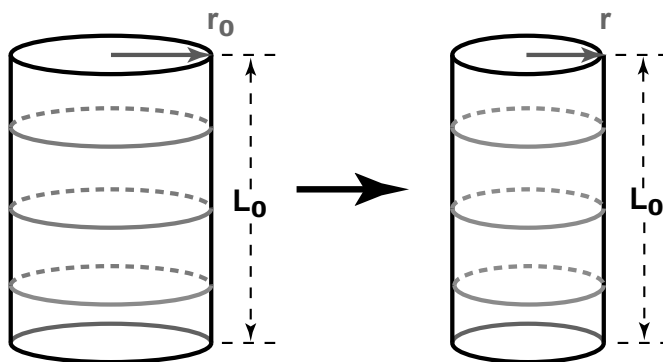


Figure B.1: A schematic of radially squeezed tube, with a few wires drawn.

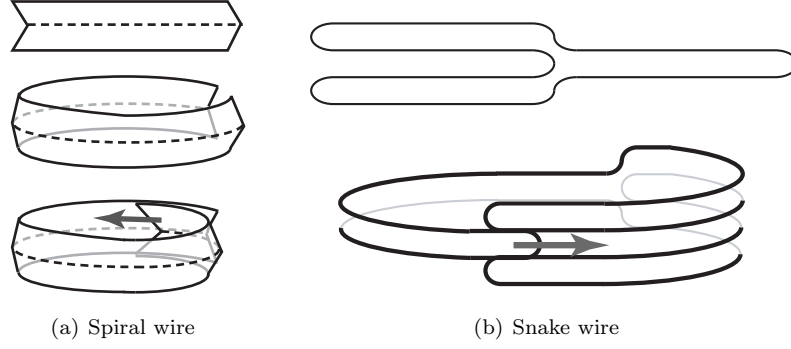


Figure B.2: Two different ways to create radial shortening through bending of the wires.

energy to reduce the radius of the tube can be calculated by:

$$E = \frac{1}{2}kD \left(\frac{1}{R} - \frac{1}{R_0} \right)^2, \quad (\text{B.4})$$

$$k = \frac{1}{4}E_Y \pi r_{wire}^4, \quad (\text{B.5})$$

where E_Y is the Young's modulus of elasticity for the wires, R and R_0 are the current and initial radii of curvature, respectively. For radial wires the radius of curvature is simply the current radius of the tube. For the purpose of these calculations we will assume that the average wire radius is the same in both of the cases that we proposed above, which means that both cases require the same amount of work to shorten the circumference of the tube.

$$E = \frac{1}{2}kD_0 \left(\frac{1}{r} - \frac{1}{r_0} \right)^2 = \frac{kD_0}{2r_0^2} \left(\frac{r_0}{r} - 1 \right)^2. \quad (\text{B.6})$$

As mentioned before, in these calculations we assume that $r \gg r_{wire}$ and we will assume so for all of these analytical models. Another scaling assumption that we need to make is that the distance between fibers is much greater than the diameter of the fibers. For now let us assume that there are n wires. By manipulating equation B.3, we can find that:

$$\frac{r_0}{r} = \frac{1}{\sqrt{1 - EF}} \Rightarrow \quad (\text{B.7})$$

$$\Rightarrow \left[\frac{r_0}{r} - 1 \right]^2 = \left[\frac{1 - \sqrt{1 - EF}}{\sqrt{1 - EF}} \right]^2 = \frac{(1 - \sqrt{1 - EF})^2}{1 - EF}. \quad (\text{B.8})$$

Applying this to equation B.6 we can find the total work performed as a function of the ejection

fraction achieved:

$$E = \frac{nkD_0}{2r_0^2} \frac{(1 - \sqrt{1 - EF})^2}{1 - EF}. \quad (\text{B.9})$$

We can write this work in a dimensionless form:

$$\tilde{E} = \frac{E}{E_Y \pi r_{wire}^2 r_0} = \frac{nr_{wire}^2 D_0}{8r_0^3} \frac{(1 - \sqrt{1 - EF})^2}{1 - EF}. \quad (\text{B.10})$$

A plot of the work required for the pumping as a function of the ejection fraction is shown in figure B.3. Note that the plot does not extend beyond ninety percent ejection fraction, because the radius of the tube becomes comparable to the radius of the wires at that point and the model breaks down, and thus the work approaches infinity for an ejection fraction of one.

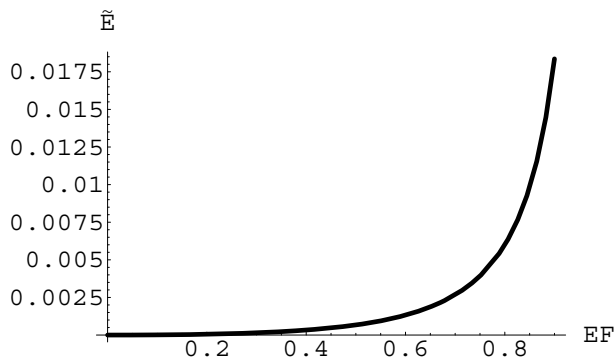


Figure B.3: The plot of work required vs. the ejection fraction achieved for radial contraction in a tube, $n=5$.

B.2.2 Twisting of the tube

Now Let us consider a cylinder made up of non-extendable longitudinal or helical wires. Again the wire radius is r_{wire} and its constant length is $D = D_0$. The cylinder has a constant radius of $r = r_0$ and an initial length of L_0 . For this model the top edge of the cylinder is held, while the bottom is rotated by an angle α (figure B.4). In this case the assumption that the distance between the fibers is much larger than the diameter of the fibers is very important. If this assumption is valid, the work put into this transformation, is the bending energy. However, if this assumption is not true and the fibers are close enough to interact with one another during the transformation the bending energy will no longer be a dominating factor. For this analytical problem we will also assume that there will be no buckling.

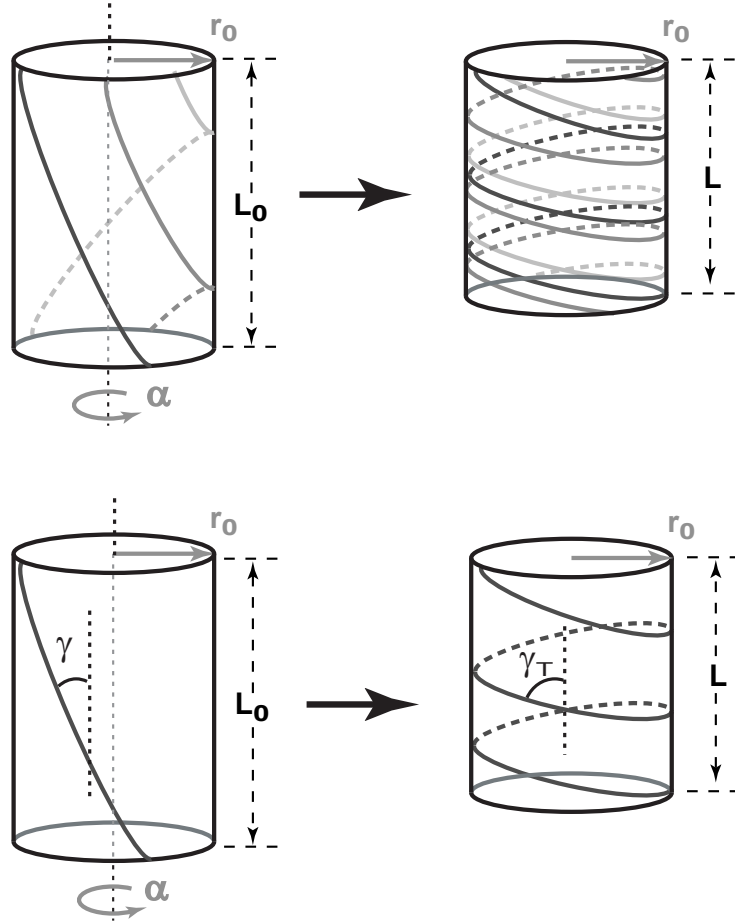


Figure B.4: Twisting of helically arranged fibers. The top series shows the tube with several wires. The bottom shows only one wire, and labels the relevant twist angles.

The length of the tube can be written in terms of the turn angle:

$$L = \sqrt{D^2 - \alpha^2 r^2}. \quad (\text{B.11})$$

Let us assume that initially the fibers are at an angle γ to the vertical (figure B.4). If this angle is $\gamma = 0$ then the length of the tube is the same as the fiber length, $L_0 = D$. Substituting these into the equation B.2 and B.1 we have:

$$EF = 1 - \frac{L}{L_0} = 1 - \frac{\sqrt{D^2 - \alpha^2 r^2}}{D} = 1 - \sqrt{1 - \left(\frac{\alpha r}{D}\right)^2}. \quad (\text{B.12})$$

However, if initially the unstressed fibers are helical and $\gamma \neq 0$, the starting twist needs to be taken into account. It is important to note that $0 \leq \gamma \leq \pi/2$. For volume calculations this can be interpreted as though we first rotated the bottom edge by an angle β , which is given by the known

twist angle, γ :

$$\beta = \frac{D \sin \gamma}{r}. \quad (\text{B.13})$$

Now we can use equations B.11, B.2 and B.1 to write the ejection fraction as a function of both the initial turn angle and the additional turn angle:

$$EF = 1 - \frac{L}{L_0} = 1 - \sqrt{\frac{D^2 - (\alpha + \beta)^2 r^2}{D^2 - \beta^2 r^2}} = 1 - \sqrt{\frac{D^2 - (\alpha r + D \sin \gamma)^2}{D^2 (1 - \sin^2 \gamma)}}. \quad (\text{B.14})$$

After the transformation the total angle that the fiber makes to the vertical is going to be:

$$\sin \gamma_t = \frac{r(\alpha + \beta)}{D} = \frac{\alpha r}{D} + \sin \gamma. \quad (\text{B.15})$$

The total γ_t also has to be between zero and $\pi/2$, which puts a constraints on α .

$$-\frac{D(\sin \gamma)}{r} \leq \alpha \leq \frac{D(1 - \sin \gamma)}{r}. \quad (\text{B.16})$$

However, if $\alpha < 0$, there would be no pumping. The upper limit on α would actually be constrained by the radius of the wire. Indeed the distance between the wires has to be greater than the diameter of the wire (figure B.5). This constrains the total twist angle to:

$$x > 2r_{wire} \Rightarrow \cos^2 \gamma_t > \frac{nr_{wire}}{\pi r} \Rightarrow \sin \gamma_t < \sqrt{1 - \left(\frac{nr_{wire}}{\pi r}\right)^2} \quad (\text{B.17})$$

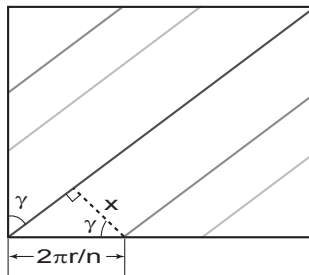


Figure B.5: The cylinder laid out flat, showing the twist angle and the distance between the wires.

That means that the limit on maximal turn angle that we can induce is:

$$\alpha < \frac{D}{r} \left[\sqrt{1 - \left(\frac{nr_{wire}}{\pi r}\right)^2} - \sin \gamma \right], \quad (\text{B.18})$$

which puts a constraint on the ejection fraction that can be reached with this device:

$$EF < 1 - \frac{1}{\cos \gamma} \left(\frac{nr_{wire}}{\pi r} \right). \quad (\text{B.19})$$

Figure B.6 shows the relationship between the initial twist angle, γ , and the maximum ejection fraction that can be achieved.

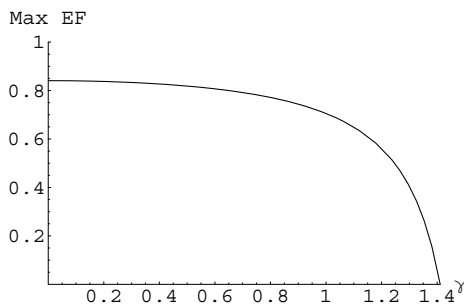


Figure B.6: The maximum ejection fraction possible with the twist method as a function of γ . Constants: $n = 5, D = 2\pi r, r_{wire} = 0.1r$.

To calculate the work used to make these transformations we can calculate the energy of bending (formula B.4) for one wire undergoing this twisting. Substituting the relationship of equation B.13 into equation C.17 from the appendix C.3 we have the expression for the radii of curvature in terms of the turn angles:

$$R_0 = \frac{D^2}{\beta^2 r} = \frac{r}{\sin^2 \gamma}, \quad R = \frac{D^2}{(\alpha + \beta)^2 r} = \frac{D^2}{\left(\alpha + \frac{D \sin \gamma}{r}\right)^2 r}. \quad (\text{B.20})$$

Plugging these into equation B.4, for one wire the work to bend it will be:

$$E = \frac{k_2}{2} \frac{r^2}{D^3} \alpha^2 (\alpha + 2\beta)^2 = \frac{k_2}{2} \frac{r^2}{D^3} \alpha^2 \left(\alpha + 2 \frac{D \sin \gamma}{r} \right)^2. \quad (\text{B.21})$$

This can be used to write the relationship between work and ejection fraction. Assuming we have n wires the work will be:

$$E = \frac{k_2 n}{2} \frac{D}{r^2} \left[1 - \left(\frac{\beta r}{D} \right)^2 \right]^2 [2EF - EF^2]^2 = \quad (\text{B.22})$$

$$= \frac{k_2 n}{2} \frac{D}{r^2} \cos^4 \gamma [2EF - EF^2]^2. \quad (\text{B.23})$$

If we write it in the same dimensionless form as for the previous case we have:

$$\tilde{E} = \frac{E}{E_Y \pi r_{wire}^2 r_0} = \frac{nD_0}{8r_0} \left(\frac{r_{wire}}{r} \right)^2 \left[1 - \left(\frac{\beta r}{D} \right)^2 \right]^2 [2EF - EF^2]^2 = \quad (\text{B.24})$$

$$= \tilde{E} = \frac{nD_0}{8r_0} \left(\frac{r_{wire}}{r} \right)^2 \cos^4 \gamma [2EF - EF^2]^2. \quad (\text{B.25})$$

It is important to note that unlike the radial shortening case the initial length of the wire is independent of the initial radius of the tube for the twisting model. If the length of the fiber is the same as the initial circumference of the cylinder, then the ejection fraction and work for the twist case can be written as:

$$EF = 1 - \frac{\sqrt{1 - \left(\frac{\alpha}{2\pi} + \sin \gamma \right)^2}}{\cos \gamma} \quad (\text{B.26})$$

$$\tilde{E} = \frac{n\pi}{4} \left(\frac{r_{wire}}{r} \right)^2 \cos^4 \gamma [2EF - EF^2]^2. \quad (\text{B.27})$$

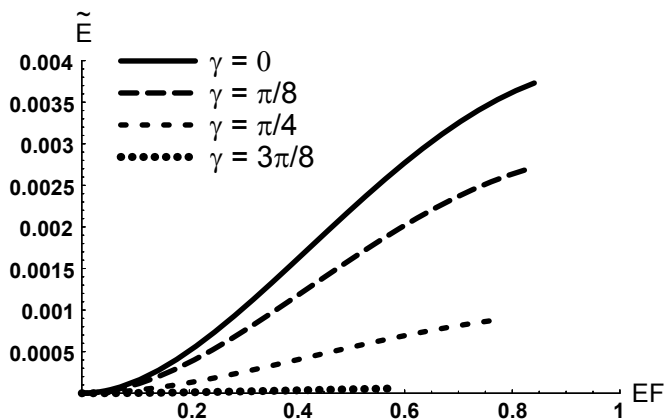


Figure B.7: The plot of work required vs. the ejection fraction achieved for twisting of the bottom of the tube. There are multiple curves for several initial twist angles, γ values, $n = 5, D = 2\pi r, r_{wire} = 0.1r$

This dimensionless work is plotted for several values of the initial twist angle in figure B.7, with the same values for the constants as in the case of the radial shortening. Each curve stops at the maximum ejection fraction that can be achieved with the starting twist angle. Note that the most efficient way to get a specific ejection fraction is to pick the maximum initial angle at which it is possible to get that ejection fraction. Indeed if we assume that the most efficient path to each specific ejection fraction is taken we can rewrite the work relationship as:

$$\tilde{E} = \frac{nD_0}{8r_0} \left(\frac{r_{wire}}{r} \right)^2 \left(\frac{nr_{wire}}{\pi r} \right)^4 \frac{[2EF_{max} - EF_{max}^2]^2}{(1 - EF_{max})^4}. \quad (\text{B.28})$$

Note that $r_{wire}/r_0 \ll 1$, so even if the length of the wire is increased this device will remain more efficient than the one that has radial shortening.

B.2.3 Pumping against inner pressure

Working with linear elasticity it is relatively easy to consider the work required to overcome the pressure inside the tube. Indeed for a tube that has inner pressure, P_{in} , and the pressure outside is P_{out} , we can use the volume calculations for both models to show:

$$\begin{aligned} E_{pressure} &= (P_{out} - P_{in})\Delta V = (P_{out} - P_{in})(V - V_0) = \\ &= (P_{out} - P_{in})V_0 \frac{V - V_0}{V_0} = -EF(P_{out} - P_{in})V_0 \end{aligned} \quad (\text{B.29})$$

This energy is not dependent on the way we achieve the ejection fraction, and will be the same for all the devices considered here, and can be added to the work calculated in the previous sections.

B.2.4 Comparing the two different methods of pumping

To see how the different methods of pumping compare we plot the dimensionless energies on the same plot, cutting the ejection fraction at 75%, since higher ejection fractions are not of interest here (figure B.8). At first glance it seems that for some ejection fractions the radial contraction device is more efficient than the twisting device. However, if for each ejection fraction the γ is chosen such that the work is most efficient to reach that ejection fraction, the results clearly show that the twisting is a better choice (figure B.9). Another way to look at it is to show the work required for the two different models when the maximal desired ejection fraction is known. Such a plot for three different ejection fractions is shown in figure B.10.

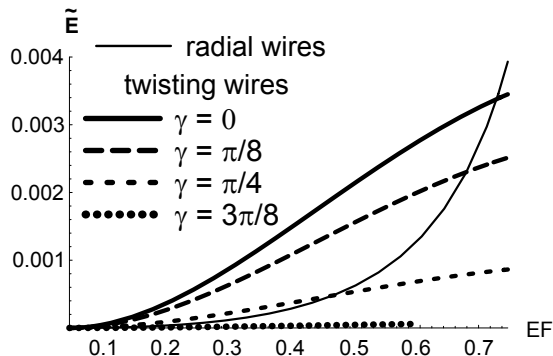


Figure B.8: The plot of work required vs. the ejection fraction achieved for both the twisting of the bottom of the tube and radial shortening of wires. There are multiple curves for several initial twist angles, γ values. All the constants are the same for both cases: $n = 5, D = 2\pi r, r_{wire} = 0.1r$.

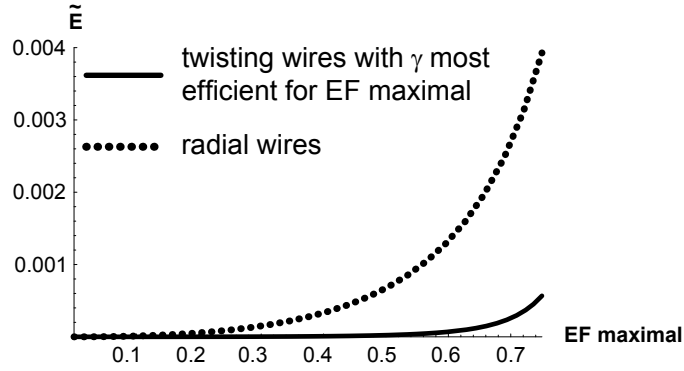


Figure B.9: The plot of work required vs. the maximal ejection fraction achieved for both the radial shortening of wires and the most efficient twisting of the bottom of the tube. All the constants are the same for both cases: $n = 5, D = 2\pi r, r_{wire} = 0.1r$.

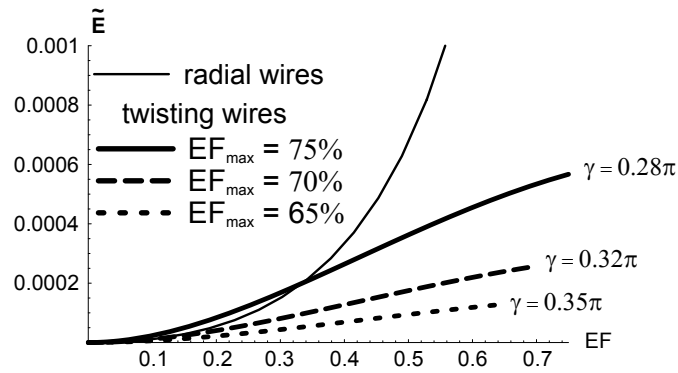


Figure B.10: The plot of work required vs. the ejection fraction achieved for both the twisting of the bottom of the tube and radial shortening of wires. There are multiple curves for several different maximal ejection fractions. All the constants are the same for both cases: $n = 5, D = 2\pi r, r_{wire} = 0.1r$.

B.3 Pumping from a half ellipsoid shell

Now let us consider pumping from a half ellipsoid shell. A biological example of such a pump would be the four chamber heart. We could potentially use the same method we did when describing the cylindrical pumps. This would not be very hard for radially contracting wires, but for helical wires it would require some very complicated mathematical expressions to describe the helix and calculate the radius of curvature in ellipsoid coordinates. Additionally, if later at some point we wanted to change the geometry of our chamber we would have to perform all the calculations again from scratch. So instead we will formulate an approximation method that will work quite well for a range of geometries.

Let us approximate the ellipsoid shell by a series of cylinders with each having a height dz . Each cylinder will have a radius of $r(z)$, which will determine the shape of our chamber. For example the

elliptical shell we will consider here will have

$$r = C \sinh \xi \sin \theta, \quad (\text{B.30})$$

$$z = C \cosh \xi \cos \theta, \quad (\text{B.31})$$

where C and ξ are constants, and θ is the parametric variable for a heart model varying $\frac{3\pi}{10} \leq \theta \leq \pi$.

We will now set up a formulation for calculating the ejection fraction of our convex shell pump. The volume of the shell will be the sum of the volumes of the cylinders that it is made up of. For the approximation to be accurate let us assume that $dz \rightarrow 0$, then instead of a sum we can write the volume in integral form. The initial volume would be given by:

$$V_0 = \pi \int_{z_0}^{z_{max}} [r(z)]^2 dz \quad (\text{B.32})$$

where z_0 and z_{max} are the initial and final height of the shell, respectively. How the volume changes will depend on how each cylinder in the stack will deform.

B.3.1 Radial Contraction in a Shell

If we have radial wires about an axisymmetric shell of shape $r(z)$ each contracting the same way as described in section B.2.1. Thus the radius changes $r_f(z) = (1 - \varepsilon)r(z)$ (note that $r(z)$ here is the initial radius). Then the volume is given by:

$$V = \pi \int_{z_0}^{z_{max}} [r_f(z)]^2 dz = \pi(1 - \varepsilon)^2 \int_{z_0}^{z_{max}} [r(z)]^2 dz = (1 - \varepsilon)^2 V_0, \quad (\text{B.33})$$

which means that the ejection fraction is the same as in equation B.3.

$$EF = 1 - (1 - \varepsilon)^2 = 2\varepsilon - \varepsilon^2. \quad (\text{B.34})$$

The energy for each wire is given by:

$$E_{one} = \frac{kD_0(z)}{2r(z)^2} \left(\frac{r(z)}{r_f(z)} - 1 \right)^2 = \frac{k\pi}{r(z)} \left(\frac{\varepsilon}{1 - \varepsilon} \right)^2. \quad (\text{B.35})$$

Thus for multiple wires the energy would become:

$$E = k\pi \left(\frac{\varepsilon}{1 - \varepsilon} \right)^2 \sum_{i=1}^n \frac{1}{r(z_i)}, \quad (\text{B.36})$$

where, i is the number of the wire. Since there is no single initial radius we will normalize this differently from the tube case:

$$\tilde{E} = \frac{E}{E_Y \pi r_{wire}^3} = \frac{r_{wire} \pi}{4} \left(\frac{\varepsilon}{1 - \varepsilon} \right)^2 \sum_{i=1}^n \frac{1}{r(z_i)}. \quad (\text{B.37})$$

B.3.2 Twisting of a Shell

When each disk is twisted it will respond in the same way as the cylinder described in section B.2.2. That means that we assume that the radius does not change while the height becomes dz' . The new height will be given by:

$$dz' = \frac{L}{L_0} dz. \quad (\text{B.38})$$

And the new volume will become:

$$V = \pi \int_{z_0}^{z_{max}} [r(z)]^2 \left(\frac{dz'}{dz} \right) dz = \pi \int_{z_0}^{z_{max}} [r(z)]^2 \left(\frac{L}{L_0} \right) dz. \quad (\text{B.39})$$

The ratio of the initial and final length can be taken from section B.2.2. The energy can be calculated in the same way, since we know that the total work that needs to be done is the sum of the work used to turn each disk we will have dE rewritten from equation B.4:

$$dE = \frac{k_2}{2} [r(z)]^2 \left(\frac{d\alpha}{dD} \right)^2 \left[\frac{d\alpha}{dD} + 2 \frac{\sin \gamma}{r(z)} \right]^2 dD. \quad (\text{B.40})$$

However, now we need to determine the boundary conditions on each of the disks so that we can apply the equations we derived for the cylinder. We specify that the bottom of the shell is rotated by α , while the top is held immobile. This means that a disk somewhere in the middle will have one rotation at the top and a bigger rotation on the bottom. However, from a solid mechanics point of view if we are rotating the whole disk as a whole, it will not experience any deformations. This means that the only rotation that will impact the shape of the disk is the difference in the rotation of the top and bottom. To use our previous formulas we can look at each disk relative to its top (now immobile) with the bottom rotating by $d\alpha$. There are multiple ways to specify $d\alpha$ as a function of z , that we will describe a little later. The other quantity that is different for each disk is the length of the wire in each disk. Obviously, this will depend on the initial fiber angle, but it will also be a function of the shape of the shell under study:

$$dD = \frac{dz}{\cos \gamma}, \quad (\text{B.41})$$

where dD is the length of fiber at each disk, as previously γ and dz is the initial fiber angle and the height of each disk, respectively. For this study we will specify that γ will not depend on z .

This means that if we are considering an ellipsoid shell, the angle γ is the angle that is made by the projection of the tangent to the fiber on the $z - \theta$ plane and the z vector. Notice, that for each disk both $d\alpha$ and dD will be small quantities, thus we will rearrange the equations for the ratio of the lengths to combine these:

$$\frac{L}{L_0} = \frac{1}{\cos \gamma} \sqrt{1 - \left[\left(\frac{d\alpha}{dD} \right) r(z) + \sin \gamma \right]^2}. \quad (\text{B.42})$$

And the total energy can be written as:

$$E = \frac{k_2}{2 \cos \gamma} \int_{z_0}^{z_{max}} \left(\frac{d\alpha}{dD} \right)^2 \left[\frac{d\alpha}{dD} r(z) + 2 \sin \gamma \right]^2 dz. \quad (\text{B.43})$$

Now let us consider the different possibilities for specifying $d\alpha$ on the disks.

The simplest rule would be to enforce that the rotations varies linearly with z , i.e., $d\alpha = \frac{\alpha}{L_0} dz$. This has the benefit of being simple, with the ‘‘small’’ ratio becoming:

$$\frac{d\alpha}{dD} = \frac{\alpha \cos \gamma}{L_0}. \quad (\text{B.44})$$

And the length ratio becomes:

$$\frac{L}{L_0} = \frac{1}{\cos \gamma} \sqrt{1 - \left[\left(\frac{\alpha \cos \gamma}{L_0} \right) r(z) + \sin \gamma \right]^2}. \quad (\text{B.45})$$

Substituting this into equation B.39 to find the final volume of the shell we have:

$$V = \pi \int_{z_0}^{z_{max}} \frac{[r(z)]^2}{\cos \gamma} \sqrt{1 - \left[\left(\frac{\alpha \cos \gamma}{L_0} \right) r(z) + \sin \gamma \right]^2} dz. \quad (\text{B.46})$$

The ejection fraction is simply given by equation B.1. The energy can be calculated to be:

$$E = \frac{k_2 \cos \gamma}{2} \left(\frac{\alpha}{L_0} \right)^2 \int_{z_0}^{z_{max}} \left[\frac{\alpha \cos \gamma}{L_0} r(z) + 2 \sin \gamma \right]^2 dz. \quad (\text{B.47})$$

We need to normalize this expression differently from what was done in the cylinder case since the radius varies with z . This will not matter since we will only be comparing the energies of the shell being twisted and radially contracted. So we will have:

$$\tilde{E} = \frac{E}{E_Y \pi r_{wire}^3} = \frac{r_{wire} \cos \gamma}{8} \left(\frac{\alpha}{L_0} \right)^2 \int_{z_0}^{z_{max}} \left[\frac{\alpha \cos \gamma}{L_0} r(z) + 2 \sin \gamma \right]^2 dz. \quad (\text{B.48})$$

While considerably more complicated these expressions have the same nature as in the case of a cylinder and predictably the same result.

B.4 Conclusion

The simple analytical problems presented here showcase of the importance of twist in pumping devices. These are of course grossly simplified, ignoring effects like buckling. However the results help us develop an instinctive understanding of the importance of twisting in biological pumps.

Appendix C

Additional Methods

C.1 Geometrical parameters in formulating the Double helical heart: healthy and diseased

In this model we assume that the double helical band to approximate the myocardium fiber architecture. While detailed description of how these equations are formulated will be published elsewhere, we give a brief overview here. As a first step we describe the changing orientation of the fibers by specifying the long-axis coordinate, z_{cent} , as a function of polar coordinate θ for the centerline of the band:

$$z_{cent} = C_1 - C_2 \frac{\theta^{A_1}}{A_2} \exp\left[-\frac{\theta}{B_2}\right] \quad (\text{C.1})$$

where C_1, C_2, A_1, A_2, B_2 are constants. The polar coordinate θ varies $\theta_{max} \geq \theta \geq 0$, where θ_{max} corresponds to the start of the band at the pulmonary aorta, and $\theta = 0$ corresponds to the end of the ascending segment.

The r -coordinate of the centerline should now be constructed in such a way that the centerline correctly skirts the ventricular chamber surfaces. So for a parabolic chamber the centerline r_{cent} :

$$\begin{aligned} r_{cent} &= \sqrt{\frac{1}{A_3} z_{cent} + ZA * C_3 [\text{Factor 1}] [\text{Factor 2}]}, \\ \text{Factor 1} &= 1 + C_4 \cos\left(\frac{\theta - \theta_{crossing}}{2}\right), \\ \text{Factor 2} &= 1 + C_5 \exp\left(-(\theta - \theta_{right})^2\right), \end{aligned} \quad (\text{C.2})$$

where, A_3, ZA, C_3, C_4 and C_5 are constants. We introduce Factor 1 to avoid self-overlap of the band at $\theta_{crossing} = \pi \left(-1 + \cot \frac{\pi}{A_1 B_2}\right)$ and $\theta_{crossing} + 2\pi$. The factor bends the centerline away from self-crossing. We also introduce Factor 2, which is only significant in the region of anterior surface and describes the fact that this surface bends significantly outwards from the septum. We choose the middle of anterior surface to correspond to $\theta_{right} = 3.8\pi$. The position of the apex of

the left ventricular chamber is taken to be at $z = C_3$. The constants of equations C.1 and C.2 are not independent when related to the geometry of the heart, for example a combined change in A_1 and ZA controls the fiber orientation in the region of the apex. The shape of the chamber can be controlled by changes in the constant A_3 . The centerline can also be written in a similar way for a spherical chamber:

$$r_{cent} = \sqrt{\frac{1}{A_3} z_{cent} + ZA * C_3 \text{ [Factor 1] [Factor 2]}} \quad (\text{C.3})$$

where R_0 characterizes the spherical shape of the ventricle, while all the other constants are the same as for equation C.2.

To make the mathematical description of the 3D shape of the band simpler, we approximate the direction of the width to be along the z -axis. The parameterized three dimensional structure is then described in cartesian coordinate, (x, y, z) , by:

$$\begin{aligned} z &= z_{cent} + \xi & r &= r_{cent}(z) + \zeta \\ x &= r \cos \theta & y &= r \sin \theta \end{aligned} \quad (\text{C.4})$$

where $-w/2 < \xi < w/2$ and $0 < \zeta < t$, with w and t are the width and the thickness of the band, respectively.

The parameters that remain constant for all models have values of $C_1 = 4.9$, $C_2 = 7$, $A_2 = 0.5$, $C_3 = -0.77$, $C_4 = 1/6$ and $C_5 = 1$. The following is the list of the models used in this paper and the parameter values for each one (unless otherwise specified equation C.2 was used):

Normal: $A_1 = 1.3, ZA = 1.1, A_3 = 1$.

Weakly Oblique: $A_1 = 1.1, ZA = 1.4, A_3 = 1$.

Moderately Oblique: $A_1 = 1.0, ZA = 1.6, A_3 = 1$.

Strongly Oblique: $A_1 = 0.9, ZA = 1.7, A_3 = 1$.

Moderately Dilated: $A_1 = 1.3, ZA = 1.1, A_3 = 1/4$.

Strongly Dilated: In this case equation (C.3) was used with $A_1 = 1.3, ZA = 1.1, A_3 = 1, R_0 = 3.8$.

Other Damage: $A_1 = 1.3, ZA = 1.1, A_3 = 1$.

C.2 Calculating Twist of the Left ventricle

In order to measure twist we attach a strip of soft material to the left ventricle. This strip of material (twist indicator) is made of a material that is two orders of magnitude softer than the non-active

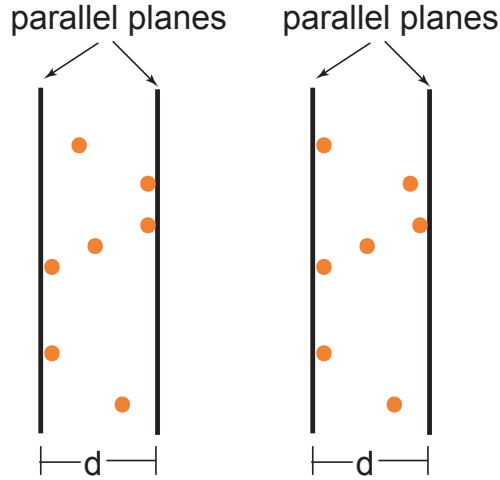


Figure C.1: A sketch of the two dimensional projection of the “sandwich” with markers. Left: a case with two markers on each plane. Right: a case with three markers on one plane and only one marker on the other plane.

material (i.e., the Young’s modulus of the twist indicator material is one hundredth of the Young’s modulus of the non-active material). As a result the twist indicator does not influence the movement of the band. In its initial configuration the strip is on a vertical plane containing the long axis of the left ventricle and at $\theta = 2.96\pi$. During the deformation of the band the strip can deform in plane or out of the plane. When the long axis of the left ventricle shortens during contraction the indicator strip deforms in plane. In the shortening of the long-axis the top and bottom portions of the left ventricle band come closer together, and to accommodate this deformation the strip buckles outward. However, unless the top and bottom portions of the band rotate with respect to each other, the buckling will occur in the same vertical plane. Conversely, in twisting of the left ventricle the bottom and top portions of the band move with respect to each other in the horizontal plane. As a result the strip deforms out-of-plane. The greater the twist of the left ventricle, the greater the out-of-plane deformation. To measure the out-of-plane deformation we keep track of the position of the nodes on the strip indicator. The way we calculate the out-of-plane distance is akin to the least squares method in 3D, we imagine two parallel planes sandwiching these nodes and minimize the distance between the planes. Because the two planes are always parallel (i.e., the normals are the same) there are two possible arrangements: In the first configuration, one plane is defined by a triplet of points, while the other is defined by a single point and the the normal of the first plane. In the second possible configuration, each plane contains a pair of points (figure C.1). Once the minimum distance, the minimal sandwich thickness, is calculated we can translate that measure directly into twist or torsion. Twist of the left ventricle is normally defined as the slope of the fit line to the relationship between the rotational angle of a marker and its long-axial position. Torsion

of the left ventricle is defined as the average of the rotations of markers placed at different positions of the long-axis. We could use the nodes of the twist indicator as markers and calculate the rotation of each one and then average to calculate torsion or twist, but this would only introduce unnecessary errors. Instead, we directly relate the out-of-plane deformation of the twist indicator to the values of twist and torsion. Assuming that the twist changes linearly with the z -coordinate of the long axis, with no twist at the basal plane and maximal twist at the apex, the maximum out-of-plane movement will be at $\frac{1}{3}$ LA from the apex in the case of a parabolic and $(1 - 1/\sqrt{2})R_0$ in the case of a spherical chamber, where LA and R_0 is the long axis and the sphere radius, respectively. As a result twist is calculated from out-of-plane deformation (d) of the twist indicator:

$$\text{twist}_{\text{parabolic}} = -\frac{3\sqrt{3}}{2} \frac{d}{(\text{LA})(r_{\text{base}})}, \quad (\text{C.5})$$

$$\text{twist}_{\text{sphere}} = -\frac{2d}{R_0^2}, \quad (\text{C.6})$$

where, LA and r_{base} are the long axis length and radius at the base (top), respectively. Once twist is known torsion can be calculated from the relationship between twist and torsion torsion = $(LA)\text{twist}/2$:

$$\text{torsion}_{\text{parabolic}} = \frac{3\sqrt{3}}{4} \frac{d}{r_{\text{base}}}, \quad (\text{C.7})$$

$$\text{torsion}_{\text{sphere}} = \frac{d}{R_0}. \quad (\text{C.8})$$

C.3 Calculating radius of curvature

Let $\vec{r}(s)$ be the parametric equation for the curve of interest, where s is the natural parameter. The tangent is given by:

$$\hat{t}(s) = \dot{\vec{r}}(s). \quad (\text{C.9})$$

We know that the relationship between the tangent and the normal can be expressed as:

$$\dot{\hat{t}}(s) = \varkappa \cdot \hat{n}(s), \quad (\text{C.10})$$

where \varkappa is the curvature. The radius of curvature is then given by

$$R = \frac{1}{\varkappa} = \frac{1}{\|\dot{\hat{t}}(s)\|}. \quad (\text{C.11})$$

C.4 Radius of Curvature for a helix about a cylinder

For a helix about a cylinder of radius r where the curve makes γ angle with the vertical, z -coordinate.

The parametric equation in terms of natural parameter s is:

$$z = s \cdot \cos \gamma, \quad \theta = \frac{s}{r} \sin \gamma, \quad (\text{C.12})$$

$$\vec{r}(s) = [x, y, z] = \left[r \cos \left(\frac{s}{r} \sin \gamma \right), r \sin \left(\frac{s}{r} \sin \gamma \right), s \cdot \cos \gamma \right]. \quad (\text{C.13})$$

The tangent is then given by:

$$\hat{t}(s) = \left[-\sin \gamma \sin \left(\frac{s}{r} \sin \gamma \right), \sin \gamma \cos \left(\frac{s}{r} \sin \gamma \right), \cos \gamma \right]. \quad (\text{C.14})$$

The derivative of the tangent is:

$$\dot{\hat{t}}(s) = \left[-\frac{1}{r} \sin^2 \gamma \cos \left(\frac{s}{r} \sin \gamma \right), -\frac{1}{r} \sin^2 \gamma \sin \left(\frac{s}{r} \sin \gamma \right), 0 \right]. \quad (\text{C.15})$$

The curvature is then:

$$\kappa = \left\| \dot{\hat{t}}(s) \right\| = \frac{\sin^2 \gamma}{r}. \quad (\text{C.16})$$

The radius of curvature is then:

$$R = \frac{r}{\sin^2 \gamma}. \quad (\text{C.17})$$

Appendix D

Extra Figures

D.1 Additional figures for chapter 2

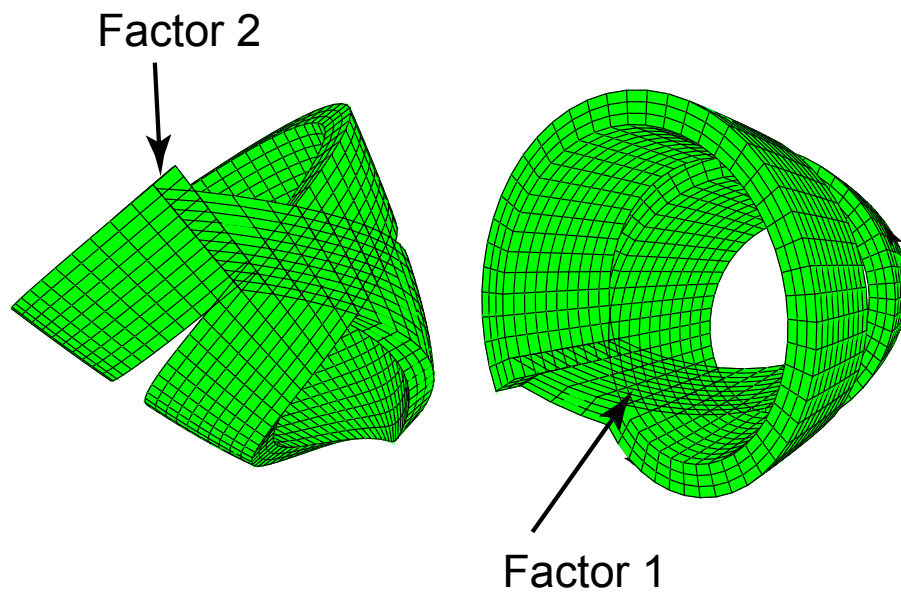


Figure D.1: The form of the band before Factor 1 and Factor 2 were included into equation 2.5. On the left the point at which Factor 2 pulls the band out is indicated. On the right the cross over point which Factor 1 separates is indicated.

D.2 Additional figures for chapter 4

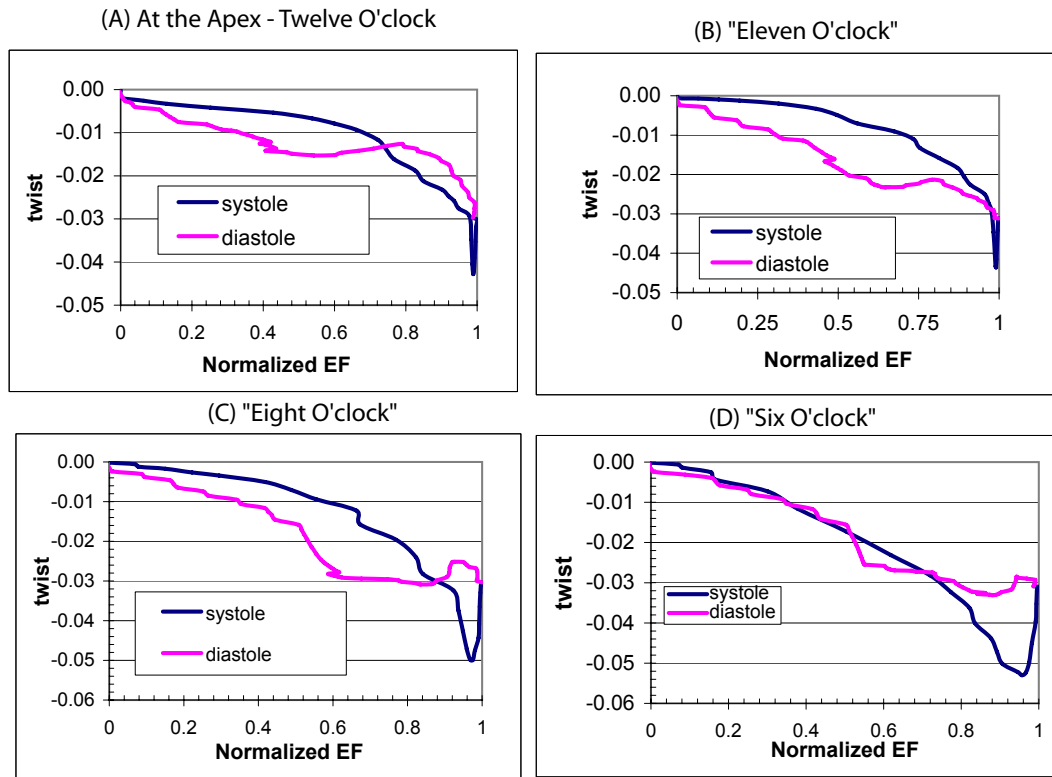


Figure D.2: Twist vs. normalized ejection fraction for spatial waves with varying origin of excitation. (A) The “Purkinje” type wave used through out this dissertation; (B) the wave origin is shifted slightly into the septum; (C) the wave origin is shifted toward the right heart; (D) the wave origin is shifted further towards the right heart. It is interesting to not that the loops seem to collapse forecasting that when the wave originates at the right heart the directions of contractions are reversed.

D.3 Alternate figures for chapter 5

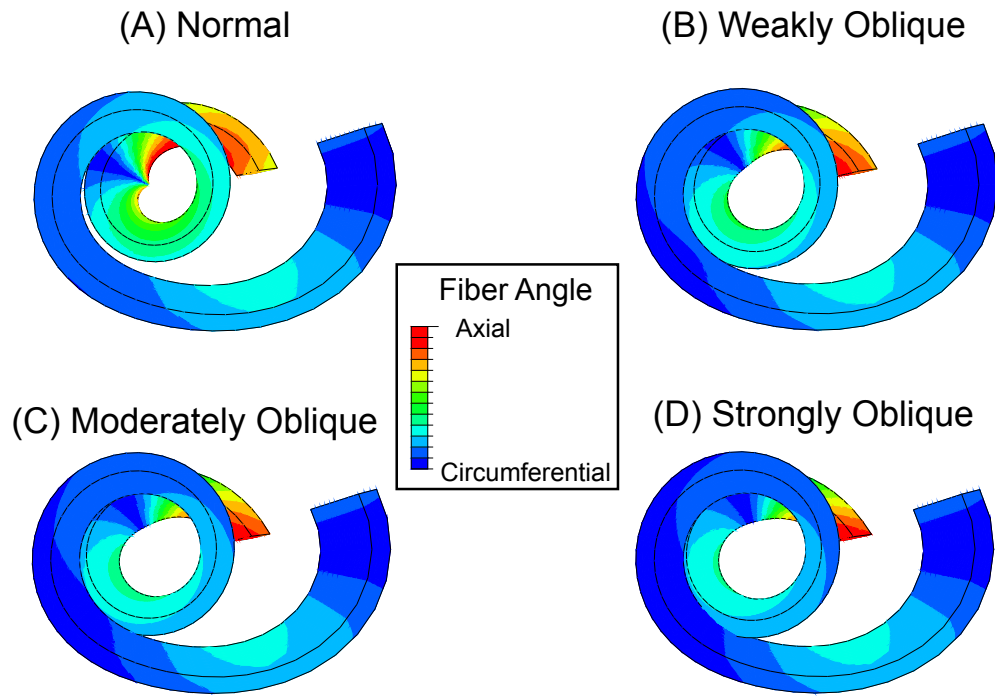


Figure D.3: Top view: The model double helical band is color coded for the fiber angle - blue and red representing circumferential and axial fibers, respectively. The fiber angle was calculated in the same way as in paper by Helm et.al. [23]. (A) "Normal" model with fiber orientation corresponding to physiological. (B) "Weakly Oblique" model showing the fibers close to the apex to be a little more oblique than in the "Normal" case. (C) "Moderately Oblique" model with fibers considerably more oblique in the apical region than would be normal. (D) "Strongly Oblique" model showing the fibers close to the apex region to be almost circumferential.

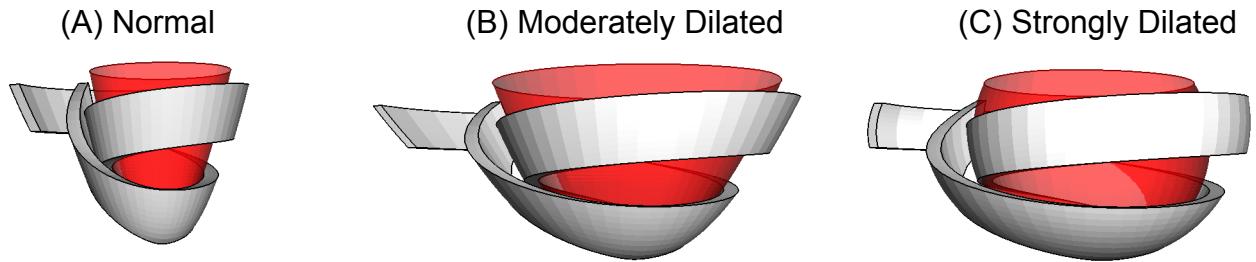


Figure D.4: Different view: The model double helical band (grey) with the fitted left ventricular (LV) volume (red). The long axis dimension in each case is 7 cm. (A) “Normal” model, the LV is approximated with a paraboloid, with the basal radius of ≈ 3.5 cm; (B) “Moderately Dilated” model, the LV is approximated with a paraboloid, with the basal radius of ≈ 6 cm; (C) “Strongly Dilated” model, the LV is approximated with a section of a sphere, with the basal radius of ≈ 7 cm.

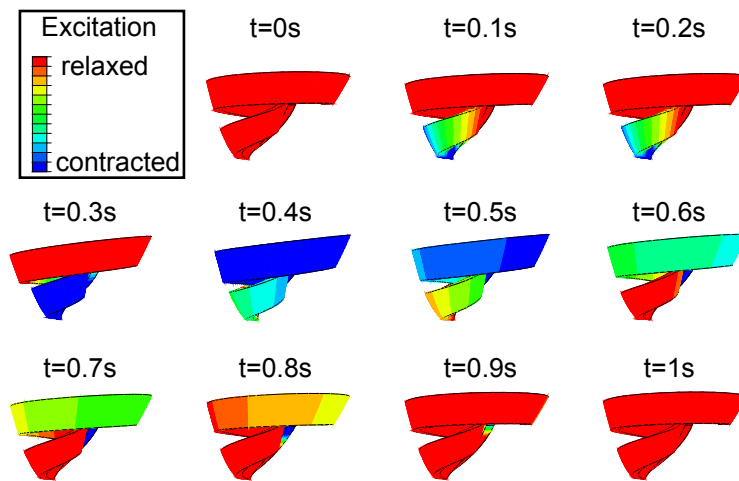


Figure D.5: Side view of the double helical band model color coded for excitation: red and blue correspond to relaxed and excited, respectively. The material is fully contracted (up to 15% shortening) when it is fully excited (blue). The excitation wave starts at the apex and propagates outward. The band is completely contracted (end-systole) at $t = 0.38$ s. During diastole the relaxation wave front also starts from the apex and travels outward.

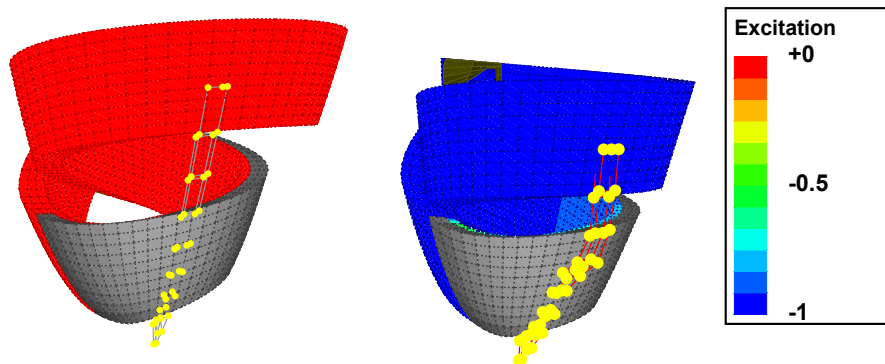


Figure D.6: The double helical band after “infarction” with the twist markers. The band is color coded for excitation: relaxed and fully contracted in red and blue, respectively. The markers are yellow circles connected with grey lines. Grey indicates the dead muscle. The left panel shows the fully relaxed band, with all the markers in plane. The right panel shows the fully contracted band, with the markers out of plane. It is also easy to visually see the volume reduction.

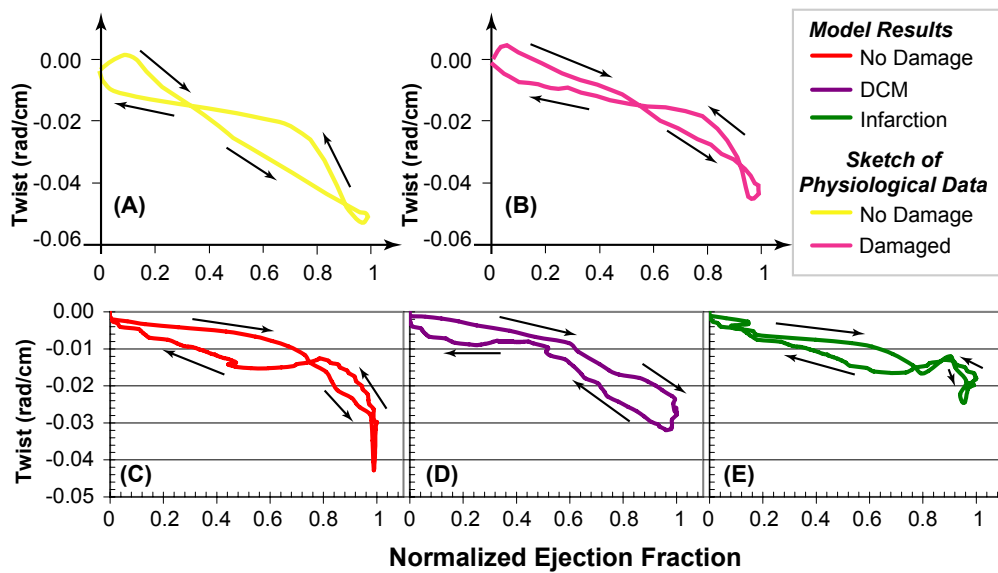


Figure D.7: Twist vs. normalized ejection fraction for: (A) A schematic showing the physiological twist for a normal heart [27]; (B) a compiled schematic for a damaged heart [27, 28]; (C) the undamaged model; (D) model of a heart with DCM; (E) Model of the heart after an infarction.

Bibliography

- [1] Wayne Rosamond, Katherine Flegal, Gary Friday, Karen Furie, Alan Go, Kurt Greenlund, Nancy Haase, Michael Ho, Virginia Howard, Bret Kissela, Steven Kittner, Donald Lloyd-Jones, Mary McDermott, James Meigs, Claudia Moy, Graham Nichol, Christopher J. O'Donnell, Veronique Roger, John Rumsfeld, Paul Sorlie, Julia Steinberger, Thomas Thom, Sylvia Wasserthiel-Smoller, Yuling Hong, for the American Heart Association Statistics Committee, and Subcommittee Stroke Statistics. Heart disease and stroke statistics—2007 update: A report from the american heart association statistics committee and stroke statistics subcommittee. *Circulation*, 115(5):e69–171, 2007.
- [2] Sharon Ann Hunt, William T. Abraham, Marshall H. Chin, Arthur M. Feldman, Gary S. Francis, Theodore G. Ganiats, Mariell Jessup, Marvin A. Konstam, Donna M. Mancini, Keith Michl, John A. Oates, Peter S. Rahko, Marc A. Silver, Lynne Warner Stevenson, Clyde W. Yancy, Elliott M. Antman, Sidney C. Jr. Smith, Cynthia D. Adams, Jeffrey L. Anderson, David P. Faxon, Valentin Fuster, Jonathan L. Halperin, Loren F. Hiratzka, Sharon Ann Hunt, Alice K. Jacobs, Rick Nishimura, Joseph P. Ornato, Richard L. Page, and Barbara Riegel. Acc/aha 2005 guideline update for the diagnosis and management of chronic heart failure in the adult—summary article: A report of the american college of cardiology/american heart association task force on practice guidelines (writing committee to update the 2001 guidelines for the evaluation and management of heart failure): Developed in collaboration with the american college of chest physicians and the international society for heart and lung transplantation: Endorsed by the heart rhythm society. *Circulation*, 112(12):1825–1852, 2005.
- [3] Khawaja Afzal Ammar, Steven J. Jacobsen, Douglas W. Mahoney, Jan A. Kors, Margaret M. Redfield, John C. Jr. Burnett, and Richard J. Rodeheffer. Prevalence and prognostic significance of heart failure stages: Application of the american college of cardiology/american heart association heart failure staging criteria in the community. *Circulation*, 115(12):1563–1570, 2007.
- [4] William J. Larsen. Development of the heart. In *Human Embryology*, pages 131–155. W. B. Saunders Company, 2nd edition, 1997.

- [5] Arian S. Forouhar, Michael Liebling, Anna Hickerson, Abbas Nasiraei-Moghaddam, Huai-Jen Tsai, Jay R. Hove, Scott E. Fraser, Mary E. Dickinson, and Morteza Gharib. The embryonic vertebrate heart tube is a dynamic suction pump. *Science*, 312(5774):751–753, 2006.
- [6] Michael Liebling, Arian S. Forouhar, Ralf Wolleschensky, Bernhard Zimmermann, Richard Ankerhold, Scott E. Fraser, Morteza Gharib, and Mary E. Dickinson. Rapid three-dimensional imaging and analysis of the beating embryonic heart reveals functional changes during development. *Developmental Dynamics*, 235(11):2940–2948, 2006. 10.1002/dvdy.20926.
- [7] A. N. Moghaddam. *Measurement and Analysis of Structure and Function of Myocardium in Embryonic and Adult Heart*. PhD thesis, California Institute of Technology, 2006.
- [8] Abbas Nasiraei-Moghaddam, Michael Liebling, Arian S. Forouhar, Huai-Jen Tsai, Scott E. Fraser, and Morteza Gharib. A lagrangian approach reveals the active and passive regions in the embryonic zebrafish heart. *Annals of Biomedical Engineering*, submitted 2007.
- [9] J. B. Cowey. The structure and function of basement membrane muscle system in amphiporus lactifloreus (nemertea). *Quarterly Journal of Microscopical Science*, 93(1):1–15, 1952.
- [10] R. B. Clark and J. B. Cowey. Factors controlling the change of shape of certain nemertean and turbellarian worms. *Journal of Experimental Biology*, 35:731–748, 1958.
- [11] Thomas Bartman and Jay Hove. Mechanics and function in heart morphogenesis. *Developmental Dynamics*, 233:373–381, 2005.
- [12] Jorg Manner. On rotation, torsion, lateralization, and handedness of the embryonic heart loop: New insights from a simulation model for the heart loop of chick embryos. *The Anatomical Record Part A: Discoveries in Molecular, Cellular, and Evolutionary Biology*, 278A(1):481–492, 2004.
- [13] D. H. Van Campen, J. M. Huyghe, P. H. M. Bovendeerd, and T. Arts. Biomechanics of the heart muscle. *European Journal of Mechanics, A/Solid*, 13(4-suppl.):19–41, 1994.
- [14] Keith L. Moore and Arthur F. Dalley. *Clinically Oriented Anatomy*. Lippincott Williams and Wilkins, New York, 5th edition, 2006.
- [15] Arthur C. Guyton and John E. Hall. *Textbook of Medical Physiology*. W.B. Saunders company, New Yourk, 10th edition, 2000.
- [16] Jay D. Humphrey. *Cardiovascular Solid Mechanics*. Springer, New York, 2002.
- [17] Gerald D. Buckberg. Basic science review: The helix and the heart. *The Journal of Thoracic and Cardiovascular Surgery*, 124(5):863–883, 2002.

- [18] L. Krehl. Beitrage zur kenntnis der fullung und entleerung des herzens. *Abh Math-Phys Kl Saechs Akad Wiss*, 17:341–362, 1891.
- [19] P.S. Jouk, Yves Usson, Gabrielle Michalowicz, and Laurence Grossi. Three-dimensional cartography of the pattern of the myofibres in the second trimester fetal human heart. *Anatomy and Embryology*, 202(2):103–118, 2000.
- [20] Daniel D. Streeter Jr., Henry M. Spotnitz, Dali P. Patel, John Ross, and Edmund H. Sonnenblick. Fiber orientation in the canine left ventricle during diastole and systole. *Circulation Research*, 24:339–347, 1969.
- [21] F. Torrent-Guasp, M. J. Kocica, A. F. Corno, M. Komeda, F. Carreras-Costa, A. Flotats, J. Cosin-Aguillar, and H. Wen. Towards new understanding of the heart structure and function. *European Journal of Cardio-Thoracic Surgery*, 27(2):191–201, 2005.
- [22] Leonid Zhukov and Alan H. Barr. Heart-muscle fiber reconstruction from diffusion tensor MRI, 2003.
- [23] Patrick Helm, Mirza Faisal Beg, Michael I. Miller, and Raimond L. Winslow. Measuring and mapping cardiac fiber and laminar architecture using diffusion tensor MR imaging. *Ann NY Acad Sci*, 1047(1):296–307, 2005.
- [24] Francesc Carreras, Manel Ballester, Sandra Pujadas, Ruben Leta, and Guillem Pons-Llado. Morphological and functional evidences of the helical heart from non-invasive cardiac imaging. *Eur J Cardiothorac Surg*, 29(Suppl1):S50–55, 2006.
- [25] Joseph C. Walker, Julius M. Guccione, Yi Jiang, Peng Zhang, Arthur W. Wallace, Edward W. Hsu, and Mark B. Ratcliffe. Helical myofiber orientation after myocardial infarction and left ventricular surgical restoration in sheep. *J Thorac Cardiovasc Surg*, 129(2):382–390, 2005.
- [26] Neil B. Ingels Jr. Myocardial fiber architecture and left ventricular function. *Technology and Health Care*, 5:45–52, 1997.
- [27] Marc R. Moon, Neil B. Ingels Jr., George T. Daughters II, Edward B. Stinson, David E. Hanses, and D. Craig Miller. Alterations in left ventricular twist mechanics with inotropic stimulation and volume loading in human subjects. *Circulation*, 89(1):142–150, 1994.
- [28] Kwok L. Yun, Marek A. Niczyporuk, George T. Daughters II, Neil B. Ingels Jr., Edward B. Stinson, Edwin L. Alderman, David E. Hanses, and D. Craig Miller. Alterations in left ventricular diastolic twist mechanics during acute human cardiac allograft rejection. *Circulation*, 83(3):962–973, 1991.

- [29] R. Beyar, F. C. P. Yin, M. Hausknecht, M. L. Weisfeldt, and D. A. Kass. Dependence of left-ventricular twist-radial shortening relations on cardiac cycle phase. *American Journal of Physiology*, 257(4):H1119–H1126, 1989. Part 2.
- [30] M. Takeuchi, T. Nishikage, H. Nakai, M. Kokumai, S. Otani, and R. M. Lang. The assessment of left ventricular twist in anterior wall myocardial infarction using two-dimensional speckle tracking imaging. *Journal of the American Society of Echocardiography*, 20(1):36–44, 2007.
- [31] M. Stuber, M. B. Scheidegger, S. E. Fischer, E. Nagel, F. Steinemann, O. M. Hess, and P. Boesiger. Alterations in the local myocardial motion pattern in patients suffering from pressure overload due to aortic stenosis. *Circulation*, 100(4):361–368, 1999.
- [32] E. Nagel, M. Stuber, B. Burkhard, S. E. Fischer, M. B. Scheidegger, P. Boesiger, and O. M. Hess. Cardiac rotation and relaxation in patients with aortic valve stenosis. *Eur Heart J*, 21(7):582–589, 2000.
- [33] M. Takeuchi, H. Nakai, M. Kokumai, T. Nishikage, S. Otani, and R. M. Lang. Age-related changes in left ventricular twist assessed by two-dimensional speckle-tracking imaging. *Journal of the American Society of Echocardiography*, 19(9):1077–1084, 2006.
- [34] F. E. Rademakers, M. B. Buchalter, W. J. Rogers, E. A. Zerhouni, M. L. Weisfeldt, J. L. Weiss, and E. P. Shapiro. Dissociation between left ventricular untwisting and filling. accentuation by catecholamines. *Circulation*, 85(4):1572–1581, 1992.
- [35] Larry A. Taber, Ming Yang, and W. William Podszus. Mechanics of ventricular torsion. *Journal of Biomechanics*, 29(6):742–752, 1996.
- [36] D. P. Zipes, P. Libby, R. O. Bonow, and E. Braunwald. *Braunwald’s Heart Disease: A Textbook of Cardiovascular Medicine*. W. B. Saunders, St. Louis, MO, 7th edition, 2005.
- [37] Constantine L. Athanasuleas, Alfred W. H. Stanley, Gerald D. Buckberg, Vincent Dor, Marissa DiDonato, and Eugene H. Blackstone. Surgical anterior ventricular endocardial restoration (saver) in the dilated remodeled ventricle after anterior myocardial infarction. *Journal of the American College of Cardiology*, 37(5):1199–1209, 2001.
- [38] A. P. Furnary, F. M. Jessup, and L. P. Moreira. Multicenter trial of dynamic cardiomyoplasty for chronic heart failure. (the american cardiomyoplasty group.). *J Am Coll Cardiol*, 28(5):1175–1180, 1996.
- [39] M. A. Pfeffer and E. Braunwald. Ventricular remodeling after myocardial infarction. experimental observations and clinical implications. *Circulation*, 81(4):1161–1172, 1990.

- [40] H. M. Hurlburt, G. P. Aurigemma, J. C. Hill, A. Narayanan, W. H. Gaasch, C. S. Vinch, T. E. Meyer, and D. A. Tighe. Direct ultrasound measurement of longitudinal, circumferential, and radial strain using 2-dimensional strain imaging in normal adults. *Echocardiography – a Journal of Cardiovascular Ultrasound and Allied Techniques*, 24(7):723–731, 2007.
- [41] Edward A. Sallin. Fiber orientation and ejection fraction in the human left ventricle. *Biophysics Journal*, 9(7):954–64, 1969.
- [42] Charles S. Peskin and David M. McQueen. A general method for the computer simulation of biological systems interacting with fluids. *Sym Soc Exp Biol.*, 49:265–76, 1995.
- [43] Sandor J. Kovacs, David M. McQueen, and Charles S. Peskin. Modelling cardiac fluid dynamics and diastolic function. *Philosophical Transactions of the Royal Society A: Mathematical, Physical and Engineering Sciences*, 359(1783):1299 – 1314, 2001.
- [44] Peter J. Hunter, Andrew J. Pullan, and Bruce H. Smaill. Modeling total heart function. *Annu Rev Biomed Eng*, 5:147–77, 2003.
- [45] Marko Vendelin, Peter Bovendeerd, Juri Engelbrecht, and Theo Arts. Optimizing ventricular fibers: Uniform strain or stress, but not atp consumption, leads to high efficiency. *American Journal of Physiology*, 283:1072–1081, 2002.
- [46] Hiroshi Watanabe, Toshiaki Hisada, Seiryu Sugiura, Jun-ichi Okada, and Hiroshi Fukunari. Computer simulation of blood flow, left ventricular wall motion and their interrelationship by fluid-structure interaction finite element method. *JSME International Journal Series C Mechanical Systems, Machine Elements and Manufacturing*, 45(4):1003–1012, 2002.
- [47] A.D. McCulloch and R. Mazhari. Regional myocardial mechanics: Integrative computational models of flow-function relations. *J Nucl Cardiol.*, 8(4):506–19, 2001.
- [48] A. D. McCulloch. Functionally and structurally integrated computational modeling of ventricular physiology. *Japanese Journal of Physiology*, 54(6):531–539, 2004.
- [49] Kevin D. Costa, Yasuo Takayama, Andrew D. McCulloch, and James W. Covell. Lamina fiber architecture and three-dimensional systolic mechanics in canine ventricular myocardium. *Am J Physiol Heart Circ Physiol*, 276(2):H595–607, 1999.
- [50] John C. Criscione, Andrew D. McCulloch, and William C. Hunter. Constitutive framework optimized for myocardium and other high-strain, lamina materials with one fiber family. *Journal of the Mechanics and Physics of Solids*, 50:1681–1702, 2002.

- [51] K.d. Costa, P. J. Hunter, J.M. Rogers, Julius M. Guccione, L.K. Waldman, and Andrew D. McCulloch. A three-dimensional finite element method for large ventricular myocardium. *Transactions of the ASME*, 118:452–72, 1996.
- [52] Roy C. P. Kerckhoffs, Maxwell L. Neal, Quan Gu, James B. Bassingthwaite, Jeff H. Omens, and Andrew D. McCulloch. Coupling of a 3d finite element model of cardiac ventricular mechanics to lumped systems models of the systemic and pulmonic circulation. *Annals of Biomedical Engineering*, 35(1):1–18, 2007.
- [53] T. P. Usyk and A. D. McCulloch. Electromechanical model of cardiac resynchronization in the dilated failing heart with left bundle branch block. *Journal of Electrocardiology*, 36:57–61, 2003.
- [54] T. P. Usyk, I. J. LeGrice, and A. D. McCulloch. Computational model of three-dimensional cardiac electromechanics. *Computing and Visualization in Science*, 4(4):249–257, 2002.
- [55] Partho P. Sengupta, Josef Korinek, Marek Belohlavek, Jagat Narula, Mani A. Vannan, Arshad Jahangir, and Bijoy K. Khandheria. Left ventricular structure and function, basic science for cardiac imaging. *Journal of the American College of Cardiology*, 48(10):1988–2001, 2006.
- [56] Partho P. Sengupta, Vijay K. Krishnamoorthy, Josef Korinek, Jagat Narula, Mani A. Vannan, Steven J. Lester, Jamil A. Tajik, James B. Seward, Bijoy K. Khandheria, and Marek Belohlavek. Left ventricular form and function revisited: Applied translational science to cardiovascular ultrasound imaging. *Journal of the American Society of Echocardiography: Official publication of the American Society of Echocardiography*, 20(5):539–551, 2007.
- [57] James C. O’Reilly, Dale A. Ritter, and David R. Carrier. Hydrostatic locomotion in a limbless tetrapod. *Nature*, 386(6622):269–272, 1997.
- [58] B. A. Dubrovin, A. T Fomenko, and S. P. Novikov. *Modern Geometry—Methods and Applications*. Springer series in Soviet mathematics, Graduate texts in mathematics. Springer-Verlag, New York, 2nd edition, 1992.
- [59] Gerald D. Buckberg, Myron L. Weisfeldt, Manel Ballester, Raphael Beyar, Daniel Burkhoff, H. Cecil Coghlan, Mark Doyle, Neal D. Epstein, Morteza Gharib, Ray E. Ideker, Neil B. Ingels, Martin M. LeWinter, Andrew D. McCulloch, Gerald M. Pohost, Leslie J. Reinlib, David J. Sahn, George Sopko, Francis G. Spinale, Henry M. Spotnitz, Francisco Torrent-Guasp, and Edward P. Shapiro. Left ventricular form and function: Scientific priorities and strategic planning for development of new views of disease. *Circulation*, 110(14):e333–336, 2004.
- [60] Richard P. Harvey and Nadia Rosenthal. *Heart Development*. Academic Press, San Diego, CA, 1999.

- [61] Claus Mattheck. *Design in Nature: Learning from Trees*. Springer, New York, 1998.
- [62] H.R. Crane. Principles and problems of biological growth. *The Scientific Monthly*, 70(6): 376–389, 1950.
- [63] Martin Kemp. Spirals of life: D’arcy thompson and theodore cook, with leonardo and durer in retrospect. *Physis; rivista internazionale di storia della scienza*, 32(1):37–54, 1995.
- [64] D. E. Hansen, G. T. d Daughters, E. L. Alderman, N. B. Ingels, E. B. Stinson, and D. C. Miller. Effect of volume loading, pressure loading, and inotropic stimulation on left ventricular torsion in humans. *Circulation*, 83(4):1315–1326, 1991.
- [65] A. Needleman, S. A. Rabinowitz, D. K. Bogen, and T. A. McMahon. A finite-element model of the infarcted left-ventricle. *Journal of Biomechanics*, 16(1):45–58, 1983.
- [66] K. Sunagawa and K. Sagawa. Models of ventricular contraction based on time-varying elastance. *Crc Critical Reviews in Biomedical Engineering*, 7(3):193–228, 1982.
- [67] P. H. M. Bovendeerd, T. Arts, T. Delhaas, J. M. Huyghe, D. H. Vancampen, and R. S. Reneman. Regional wall mechanics in the ischemic left ventricle: Numerical modeling and dog experiments. *American Journal of Physiology-Heart and Circulatory Physiology*, 39(1):H398–H410, 1996.
- [68] T. Arts, P. Bovendeerd, T. Delhaas, and F. Prinzen. Modeling the relation between cardiac pump function and myofiber mechanics. *Journal of Biomechanics*, 36(5):731–736, 2003.
- [69] T. Arts, T. Delhaas, P. Bovendeerd, X. Verbeek, and F. W. Prinzen. Adaptation to mechanical load determines shape and properties of heart and circulation: the circadapt model. *American Journal of Physiology-Heart and Circulatory Physiology*, 288(4):H1943–H1954, 2005.
- [70] Vincent Dor, Marisa Di Donato, Michel Sabatier, Francoise Montiglio, Filippo Civaia, and RESTORE Group. Left ventricular reconstruction by endoventricular circular patch plasty repair: A 17-year experience. *Seminars in Thoracic and Cardiovascular Surgery*, 13(4):435–447, 2001.
- [71] Peng Zhang, Julius M. Guccione, Susan I. Nicholas, Joseph C. Walker, Philip C. Crawford, Amin Shamal, David A. Saloner, Arthur W. Wallace, and Mark B. Ratcliffe. Left ventricular volume and function after endoventricular patch plasty for dyskinetic anteroapical left ventricular aneurysm in sheep. *Journal of Thoracic and Cardiovascular Surgery*, 130(4):1032–1038, 2005.
- [72] Hiromi Nakai, Masaaki Takeuchi, Tomoko Nishikage, Michiko Kokumai, Shinichiro Otani, and Roberto M. Lang. Effect of aging on twist-displacement loop by 2-dimensional speckle tracking imaging. *Journal of the American Society of Echocardiography*, 19(7):880–885, 2006.

- [73] Frederick A. Tibayan, David T. M. Lai, Tomasz A. Timek, Paul Dagum, David Liang, George T. Daughters, Neil B. Ingels, and D. Craig Miller. Alterations in left ventricular torsion in tachycardia-induced dilated cardiomyopathy. *J Thorac Cardiovasc Surg*, 124(1):43–49, 2002.
- [74] Inc ABAQUS. *ABAQUS Version 6.5 commercial computer software documentation*. Hibbitt, Karlsson and Sorensen Inc., Plymouth, MI USA, 2004.
- [75] Harm J. Muntinga, Frederik van den Berg, Hans R. Knol, Menco G. Niemeyer, Paul K. Blanksma, Henk Louwes, and Ernst E. van der Wall. Normal values and reproducibility of left ventricular filling parameters by radionuclide angiography. *The International Journal of Cardiac Imaging*, 13(2):165–171, 1997.
- [76] Fumio Yuasa, Tsutomu Sumimoto, Toshihiko Hattori, Toshimitsu Jikuhara, Makoto Hikosaka, Tetsuro Sugiura, and Toshiji Iwasaka. Effects of left ventricular peak filling rate on exercise capacity 3 to 6 weeks after acute myocardial infarction. *Chest*, 111(3):590–594, 1997.
- [77] D. Ajami, O. Oeckler, A. Simon, and R. Herges. Synthesis of a mobius aromatic hydrocarbon. *Nature*, 426(6968):819–821, 2003.
- [78] David M. Lemal. Aromatics do the twist. *Nature*, 426:776–77, 2003.
- [79] Piotr Pieranski, Justyna Baranska, and Arne Skjeltorp. Tendril perversion—a physical implication of the topological conservation law. *European Journal of Physics*, 25:613–21, 2004.
- [80] Jeremy M. Berg, John L. Tymoczko, and Lubert Stryer. *Biochemistry*. W. H. Freeman and Company, New York, 5th edition, 2002.
- [81] Yehuda Snir and Randall D. Kamien. Entropically driven helix formation. *Science*, 307:1067, 2005.
- [82] T.A. Cook. *The Curves of Life*. Dover, 1979.